

Surveys of Clumps, Cores, and Condensations in Cygnus X:
I. a New Catalog of ~ 0.1 pc Massive Dense Cores

YUE CAO (曹越)^{1,2} KEPING QIU,^{1,2} QIZHOU ZHANG,³ YUWEI WANG,^{1,2} BO HU,^{1,2} AND JUNHAO LIU^{1,2}

¹*School of Astronomy and Space Science, Nanjing University, 163 Xianlin Avenue, Nanjing 210023, P.R.China*

²*Key Laboratory of Modern Astronomy and Astrophysics (Nanjing University), Ministry of Education, Nanjing 210023, P.R.China*

³*Harvard-Smithsonian Center for Astrophysics, 60 Garden St., MS 42, Cambridge, MA 02138 USA*

(Received - -, -; Revised - -, -; Accepted - -, -)

Submitted to ApJS

ABSTRACT

Using infrared to (sub)millimeter data from *Spitzer*, *Herschel*, the James Clerk Maxwell Telescope, and the IRAM 30-m telescope, we conducted an unbiased survey of the massive dense cores (MDCs) in the Cygnus X molecular cloud complex, aimed at characterizing the physical conditions of high-mass star formation (HMSF) at ~ 0.1 pc scales. We created $5^\circ \times 6^\circ$ images of the 70–1200 μm dust continuum, gas column density, and dust temperature of Cygnus X. A spatial relation between the dense regions ($A_v \geq 15$) and the developed H II regions was found, indicating the impact of the latter on the global structures of Cygnus X. With a $35-M_\odot$ mass threshold implied by HMSF signposts, we identified 151 MDCs with sizes of ~ 0.1 pc, masses of 35–1762 M_\odot , and temperatures of 8–35 K. Our MDC sample is statistically complete in Cygnus X and is three times larger than that in Motte et al. (2007). The MDCs were classified into IR-bright/IR-quiet ones based on their mid-infrared fluxes and a large “IR-quiet” proportion (90%) was found in our sample. Two possible scenarios were proposed to interpret this: accelerated HMSF and the incapability of HMSF of the IR-quiet MDCs. We also found 26 starless MDCs by their lack of compact emissions at 21–70 μm wavelengths, of which the most massive ones are probably the best candidates of initial HMSF sites in Cygnus X.

Keywords: ISM: clouds — ISM: individual objects (Cygnus X) — ISM: structure — stars: formation — stars: massive

1. INTRODUCTION

High-mass stars ($M_* > 8 M_\odot$) play an important role in physical and chemical evolution of interstellar medium and energy budget of galaxies. Studies on their formation have made significant progress over the past decades (see Tan, & McKee 2002; Hoare et al. 2007; Zinnecker, & Yorke 2007; Tan et al. 2014; Motte et al. 2017; Schilke 2017; Tan 2018). Observational studies have confirmed that high-mass stars form in massive dense cores (MDCs), which are ~ 0.1 pc dense entities in molecular clouds with masses of tens to hundreds of solar masses (e.g., Motte et al. 2007; Beuther et al. 2010; Csengeri et al. 2011; Hennemann et al. 2014; Tigé et al. 2017; Ching et al. 2018). The physical conditions of high-

mass star formation (HMSF) are closely related to the formation and dynamical evolution of MDCs.

One of the key arguments in HMSF is whether high-mass stars form as a scaled-up version of the classic low-mass star formation paradigm (Shu et al. 1987). Two theoretical models have been developed in this context: the core accretion model (McKee & Tan 2002; Krumholz et al. 2007) and the competitive accretion model (Bonnell et al. 2001; Bonnell & Bate 2006). In the core accretion scenario, high-mass stars form through the monolithic collapse of high-mass analogs of low-mass prestellar cores (McKee & Tan 2002; Krumholz et al. 2007). While in the competitive accretion scenario, “seeds” of high-mass stars accrete and grow competitively in massive cores or clumps (Bonnell et al. 2001; Bonnell & Bate 2006; Zhang et al. 2009; Hartmann et al. 2012). Whether high-mass prestellar cores exist, is then an essential observable distinction of the two models. So far there have been quite a number of millimeter/submillimeter

surveys and case studies targeting massive clumps and cores (Motte et al. 2007; Bontemps et al. 2010; Wang et al. 2012; Duarte-Cabral et al. 2013; Cyganowski et al. 2014; Zhang et al. 2015; Tigé et al. 2017; Cheng et al. 2018), and infrared-dark clouds (IRDCs) (Rathborne et al. 2006; Butler & Tan 2012; Tan et al. 2013; Peretto et al. 2014; Wang et al. 2014; Lu et al. 2015; Ohashi et al. 2016; Kong et al. 2017), yet no bona fide high-mass prestellar cores have been identified.

In this paper we focus on Cygnus X, one of the most massive and active high-mass star-forming regions in our Galaxy. Lying at a distance of 1.4 kpc (Rygl et al. 2012), it harbors numerous H II regions (Wendker et al. 1991), OB associations (Uyaniker et al. 2001), and high-mass star-forming sites, including W75N, DR21, DR21(OH), and S106 (Schneider et al. 2002; Shepherd et al. 2004). Motte et al. (2007) (hereafter M07) carried out a dust continuum survey covering a 3-square-degree area in Cygnus X, and detected a total of 129 dense cores, of which 42 cores are considered as probable precursors of high-mass stars (i.e., MDCs). Here we take the advantage of a newly available large data set from *Spitzer*, *Herschel*, and the James Clerk Maxwell Telescope (JCMT), and perform a detailed multi-wavelength survey of the MDCs in Cygnus X with a spatial coverage one order of magnitude larger than that of M07.

The distance of Cygnus X has been debated over decades. Due to its location on the tangent point of the Galaxy rotation, Cygnus X has been once considered as a superposition of various objects (e.g., Dickel et al. 1969; Pipenbrink & Wendker 1988; Uyaniker et al. 2001). However, recent CO surveys toward Cygnus X suggested that it is more likely to be located at a coherent distance (e.g., Schneider et al. 2006; Gottschalk et al. 2012); Rygl et al. (2012) measured the parallaxes of five maser sites in Cygnus X and concluded that Cygnus X North is a physically connected region at ~ 1.4 kpc; Xu et al. (2013) provided a comprehensive result of parallax measurement of the Local Arm, of which eight out of nine maser sites in Cygnus X have distances within 1.3–1.6 kpc, except AFGL 2591 (3.3 kpc). We therefore will assume that most of the objects in Cygnus X share a coherent distance of 1.4 kpc, except a few regions, e.g., AFGL 2591 (see Sect. 3.2.1). It should be noticed that M07 adopted a distance value of 1.7 kpc in their analysis, which was derived by the ^{13}CO study of Schneider et al. (2006). Since this value has been updated to 1.4 kpc, we will modify their results to match the new distance before any comparisons are made, and the corrected results will hereafter be referred to as “M07” unless otherwise specified.

As the first paper of our project, Surveys of Clumps, CorEs, and CoNdenSations in CygnUS-X (CENSUS¹), we

describe our data used in Sect. 2. In Sect. 3 we discuss our data processing, including generating large maps of Cygnus X, MDC sample selection, SED fitting, classification of MDCs, and analysis on HMSF signposts. We discuss these main results in Sect. 4, including the formation and HMSF potential of large-scale cloud structures, review of the MDC sample and comparison with M07, infrared properties of the MDCs and the interpretations of HMSF, and the starless MDCs in Cygnus X. Our conclusions are summarized in Sect. 5.

2. DATA

2.1. Ground-based Observations

The published 1.2 mm continuum images from the MAMBO and MAMBO-2 cameras of the 30-m telescope of Institut de Radioastronomie Millimétrique (IRAM) in M07 were used for our analysis. The 3 deg² spatial coverage of these images are shown in Figure 1. The beam size is 11'' and the mean 1σ rms level is 12.9 mJy \cdot beam⁻¹ (see Table 1). Detailed observational parameters and data processing can be found in M07.

The JCMT SCUBA-2 continuum data at 450 μm and 850 μm toward Cygnus X were obtained from the Canadian Astronomy Data Centre², which have not been published before. The observations were made in scan mode during 2011–2015 and the average integration time of each map is ~ 0.5 h. The FWHM beam sizes are 7.9'' and 13'' and the 1σ rms levels are 340 mJy beam⁻¹ and 34 mJy beam⁻¹ for 450 μm and 850 μm , respectively. See Figure 1 for the coverage of the images. The related program IDs are M11BEC30, M12BU30, M13AD03, M13AU03, M13BU29, M15AI133, and M15AI144.

2.2. Space Telescope Observations

Continuum images in the wavelengths of *Herschel* PACS (70 and 160 μm) and SPIRE (250, 350, and 500 μm) were obtained from the *Herschel* Science Archive³. These data are from the HOBYS⁴ project (Motte et al. 2010), the Hi-GAL⁵ project (Molinari et al. 2010), and open-time observations toward Cygnus X by Hora (2011). See the corresponding references for their observational configurations and data processing. The beam sizes are 5.2'', 12'', 17.6'', 23.9'', and 35.2'',

in the Cygnus X complex. The project consists of several parallel surveys involving the SMA, JVLA, JCMT, Tianma 65m radio telescope (Shanghai 65 m Radio Telescope), as well as case studies with ALMA, NOEMA, and CARMA.

² <http://www.cadc-ccda.hia-ihp.nrc-cnrc.gc.ca/en/>

³ <http://archives.esac.esa.int/hsa/whsa/>

⁴ *Herschel* imaging survey of OB Young Stellar objects, <http://www.herschel.fr/cea/hobys/en/index.php>

⁵ The *Herschel* Infrared Galactic Plane Survey, <https://hi-gal.ifs-roma.inaf.it/higal/>

¹ CENSUS project (PI: Keping Qiu) is dedicated to a systematic study of the 0.01–10 pc hierarchical cloud structures and high-mass star formation

and the 1σ rms levels are $4.0 \text{ mJy} \cdot (3.2'' \text{ pixel})^{-1}$, $2.9 \text{ mJy} \cdot (3.2'' \text{ pixel})^{-1}$, $41 \text{ mJy} \cdot \text{beam}_{250\mu\text{m}}^{-1}$, $50 \text{ mJy} \cdot \text{beam}_{350\mu\text{m}}^{-1}$, and $30 \text{ mJy} \cdot \text{beam}_{500\mu\text{m}}^{-1}$, respectively in the order of increasing wavelengths (Table 1).

The *Spitzer* IRAC 8- μm and MIPS 24- μm maps from the *Spitzer* Legacy Survey of the Cygnus X Complex⁶ (Kraemer et al. 2010) were obtained from the NASA/IPAC Infrared Science Archive⁷. Both maps cover the entire Cygnus X region (see Figure F1 and F2). The resolutions are $2''$ and $6''$, and the 1σ rms noise levels are 47.9 and $5.2 \text{ MJy} \cdot \text{sr}^{-1}$ respectively for $8 \mu\text{m}$ and $24 \mu\text{m}$.

Table 1. Main Parameters of the Data Used

Telescopes	Instruments	Bands (μm)	<i>FWHM</i> ($''$)	1σ rms ($\text{MJy} \cdot \text{sr}^{-1}$)
<i>Spitzer</i>	IRAC	8	1.98	47.9
	MIPS	24	6	5.2
<i>Herschel</i>	PACS	70	9.2	16.5
		160	12.6	12.0
	SPIRE	250	18.4	4.97
		350	25.2	3.29
		500	36.7	0.91
JCMT	SCUBA-2	450	7.9	204
		850	13	7.6
IRAM	MAMBO/MAMBO-2	1200	11	4.0

3. ANALYSIS

3.1. Mosaic Maps of Cygnus X

We generated mosaic images of the whole Cygnus X region in the bands of *Herschel* (70, 160, 250, 350, and 500 μm), JCMT (450 and 850 μm), and the IRAM 30 m telescope (1.2 mm) using the *Montage* package⁸ (Jacob et al. 2010) (see Figures F3 to F10). The procedures include re-projection, re-gridding, and merging of the original data in each band. For the *Herschel* data, the zero-level offset correction was conducted with the Planck (217, 353, 545, and 857 GHz) and IRAS (100 μm) data following the procedure of Bernard et al. (2010). All the mosaic maps are $5^\circ \times 6^\circ$ in size with resolutions presented in Table 1. An RGB color image made out of three *Herschel* mosaics was also created (see Figure F14).

⁶ <https://www.cfa.harvard.edu/cygnusX/>

⁷ IRSA is chartered to curate the science products of NASA’s infrared and submillimeter missions, providing access to more than 20 billion astronomical measurements, including all-sky coverage in 24 bands. <http://irsa.ipac.caltech.edu/frontpage/>

⁸ <http://montage.ipac.caltech.edu/>

High-resolution column density map (Figure 1) and temperature map (Figure F12) of Cygnus X were generated from the 160, 250, 350, and 500 μm mosaic images using the *hirescoldens* command in the *getsources*⁹ (v2.180813) procedure (Men’shchikov et al. 2012). This command decomposed the continuum images into single-spatial-scale components and pixel-by-pixel fitted the SEDs at each scale using a modified blackbody model fully described in Sect. 3.2.2. The column density map was then constructed by combining the column density “components” at each scale, and its final resolution was set by that of the second shortest wavelength ($18.4''@250 \mu\text{m}$). The temperature map is nevertheless not addable and was generated using the same SED fitting routine with the images convolved to the lowest resolution ($36.7''@500 \mu\text{m}$). The 70 μm data were not used since the emission traces warm dust and a single-temperature model is no longer applicable (see Motte et al. 2010). For parameter settings, we used a dust-opacity spectral index $\beta = 2$ and a gas-to-dust ratio of 100. We conservatively estimated the relative flux uncertainties in each band as 0.2. The uncertainty maps of column density and temperature (Figure F11 and F13) were generated by *hirescoldens*, which considered both the flux uncertainties and the fitting errors.

3.2. Complete Sample of Massive Dense Cores

In principle, our target sample should contain all the MDCs in Cygnus X which are massive enough to be able to form high-mass stars. We will describe the procedure for generating our MDC sample in this subsection.

3.2.1. Selection of High-column-density Fields

High-mass stars form preferentially in high-column-density regions, both proposed by theoretical works (Krumholz & McKee 2008) and verified by observations (e.g., Motte et al. 2007; Kauffmann & Pillai 2010). To find regions in Cygnus X with potential of HMSF, i.e., regions where MDCs reside, we selected 40 rectangular fields on the column density map that cover regions where $N_{\text{H}_2} \geq 3.5 \times 10^{22} \text{cm}^{-2}$ (see Figure 1 and E1). Informations of the fields are listed in Table A. The column density threshold ($3.5 \times 10^{22} \text{cm}^{-2}$, corresponding to $A_v \gtrsim 15$, Güver & Özel 2009) guarantees that all the cores with masses above certain value can be selected in our sample. Specifically, assuming that cores have 2D Gaussian profiles in the column density map with FWHM sizes d_{FWHM} and peak column densities $N_{\text{H}_2, \text{p}}$, their masses can be estimated as:

$$M = \frac{\pi}{4 \ln 2} \mu_{\text{H}_2} m_{\text{H}} N_{\text{H}_2, \text{p}} D^2 d_{\text{FWHM}}^2, \quad (1)$$

where $\mu_{\text{H}_2} = 2.8$ is the mean molecular weight per hydrogen molecule, m_{H} is the mass of hydrogen atom, and D is the

⁹ <http://www.herschel.fr/cea/gouldbelt/en/getsources/>

source distance. Cores with $N_{\text{H}_2, \text{p}} \geq 3.5 \times 10^{22} \text{ cm}^{-2}$ and typical sizes of 0.1 pc, or 0.15 pc convolved with the $18''$ beam, will have masses above $23.3 M_{\odot}$. In other words, our core sample to be extracted in the selected fields will be *statistically complete for the cores with $M \geq 23.3 M_{\odot}$* .

To rule out the regions of which the distances are not coherent with 1.4 kpc, we used the JVLA K-band observation of ammonia inversion lines toward the fields in Cygnus X (proposal ID: VLA/17A-107, PI: Keping Qiu, Zhang et al. in prep.) and found that the systematic velocities of the field C01 and part of the field C08 are -41 and $-65 \text{ km} \cdot \text{s}^{-1}$, respectively, which correspond to BeSSeL¹⁰ kinematic distances of 6.1 and 9.1 kpc, respectively. We excluded *the whole C01 field and part of the C08 field*, as well as *AFGL 2591 in field S29* from the regions for core extraction. See Figure 1 and the corresponding sub-figures in Figure E1 for the excluded regions.

To select MDCs in Cygnus X, Motte et al. (2007) used a criterion of $A_V \geq 15$ mag and selected $\sim 3 \text{ deg}^2$ high-extinction regions (see the white dashed polygons in Figure 1). Compared with their coverage, our new fields have a total area of 2.2 deg^2 but are focused on denser regions. In addition, 14 out of 39 fields are newly added compared with M07. These fields have peak column densities comparable to those of the regions in M07 but were not covered in their IRAM observations. This indicates that our sample of MDCs represents great improvements on statistical completeness.

3.2.2. Core Extraction and SED Fitting

Table 2. Percentages of the Cores

Band	Flux ^a	SED fitting ^b
<i>Herschel</i> 70 μm	54.1%	0.0%
<i>Herschel</i> 160 μm	68.3%	66.7%
<i>Herschel</i> 250 μm	64.3%	61.6%
<i>Herschel</i> 350 μm	62.2%	57.1%
JCMT 450 μm	22.8%	12.2%
<i>Herschel</i> 500 μm	56.0%	49.4%
JCMT 850 μm	47.9%	46.7%
IRAM 1.2 mm	21.8%	21.5%

^a Percentages of cores that *getsources* successfully extracted their fluxes in this band.

^b Percentages of cores of which the fluxes in this band were used for SED fitting. The *Herschel* 70 μm fluxes were not used intentionally (see Sect. 3.2.2).

Cores in each field are extracted using *getsources* (Men’shchikov et al. 2012; Men’shchikov 2017), which is a multi-scale, multi-wavelength source extraction algorithm. In spirit, it consists of two main procedures: detection and measurement. Detection of compact sources is based on the detection images in each band, which are generated by decomposed, cleaned and background-removed single-scale images. The measurement procedure then measures the properties of sources (sizes, positions, and fluxes in each band). We used the 70–1200 μm continuum images of the fields as inputs of *getsources* and a *deconvolved* maximum core size of $35''$ (0.23 pc) for background removal (the actual scale for background removal in each band is this deconvolved size convolved with the corresponding beam). Data in 70 μm were not used to constrain source positions since their emission peaks can deviate significantly from density peaks. After running through the 39 fields, 963 cores were identified by *getsources*. Table 2 lists the percentages of cores that *getsources* have successfully measured their fluxes in each band. As can be seen, at least nearly half of the cores do not have well-defined fluxes in each band, indicating that this core catalog needs re-selection in order to truly reflect the ~ 0.1 pc entities in Cygnus X.

To create such a “robust” core catalog, we used the following four criteria: (1) having fluxes in at least three bands; (2) having SEDs that can be fitted to obtain masses and temperatures (see below); (3) relative mass error in SED fitting $\Delta M/M < 0.8$; (4) relative temperature error in SED fitting $\Delta T/T < 0.5$. The SED fitting procedure are described as follows.

We used the *curve_fit* function in the Python package *scipy*¹¹ to fit the SEDs of cores with the modified blackbody model

$$F_{\nu} = \frac{\kappa_{\nu} B_{\nu}(T) M}{D^2}, \quad (2)$$

where $B_{\nu}(T)$ is the Planck function and κ_{ν} is the dust mass opacity, which is evaluated following the HOBYS consortium: $\kappa_{\nu} = \kappa_0 (\nu/\nu_0)^{\beta}$, where $\kappa_0 = 0.1 \text{ cm}^2 \text{ g}^{-1}$, $\nu_0 = 1 \text{ THz}$, and $\beta = 2$. We used the fluxes at $\lambda \geq 160 \mu\text{m}$ for the fitting and the data points. During the fitting, we found that some fluxes significantly deviated from the model (see Figure C). These fluxes were poorly extracted by *getsources* due to the low resolutions or poor data qualities in some bands (e.g., *Herschel* 500 μm and JCMT 450 μm). We removed them from our SED fitting by eye-inspection and the fractions of the cores of which the fluxes were used in SED fitting are listed in Table 2.

With the criteria mentioned above, we selected a total of 496 “robust” cores, which we considered to reliably reflect

¹⁰ Bar and Spiral Structure Legacy survey, <https://www3.mpifr-bonn.mpg.de/staff/abrunthaler/BeSSeL/index.shtml>

¹¹ <http://www.scipy.org/>

the ~ 0.1 pc entities in Cygnus X. Furthermore, 205 out of the *robust* cores have $M \geq 23.3 M_{\odot}$ and are thus statistically complete (*complete* cores, see Sect. 3.2.1). See Figure 2 for an illustration of the relative relations of these core sets.

Once the masses and temperatures of cores were determined, physical parameters such as integrated far-IR luminosity, column density, and volume density can also be obtained as

$$L_{\text{FIR}} = 4\pi D^2 \int_0^{+\infty} F_{\nu} d\nu, \quad (3)$$

$$N_{\text{H}_2} = \frac{4}{\pi} \frac{M}{\mu_{\text{H}_2} m_{\text{H}} FWHM_{\text{dec}}^2}, \quad (4)$$

$$n_{\text{H}_2} = \frac{6}{\pi} \frac{M}{\mu_{\text{H}_2} m_{\text{H}} FWHM_{\text{dec}}^3}, \quad (5)$$

where $FWHM_{\text{dec}}$ is the deconvolved FWHM size at $160 \mu\text{m}$, since $160 \mu\text{m}$ is the highest-resolution band that can reflect optically thin dust emissions.

3.2.3. Signposts of High-mass Star Formation and Sample of MDCs

Table 3. Physical Properties of the MDCs in Cygnus X

Samples		$FWHM$ size (pc)	T (K)	M (M_{\odot})	N_{H_2} (10^{22}cm^{-2})	n_{H_2} (10^5cm^{-3})	L_{FIR} (L_{\odot})
All	min	0.09	8.4	35	2.5	0.4	2
	max	0.31	34.7	1762	1263.3	1715.0	2.04×10^4
	mean	0.14	15.2	131	83.7	58.8	631
IR-bright	mean	0.15	22.9	398	147.6	67.1	4.47×10^3
IR-quiet but not starless	mean	0.14	15.0	109	82.1	63.6	252
Starless	mean	0.13	11.8	71	22.2	9.6	22

In our definition, MDCs are cores that are sufficiently massive to have the potential of HMSF. To find them in our *complete* core sample, we took the simple idea that MDCs should have masses exceeding some lower limit, if a constant core-to-star efficiency is assumed (Alves et al. 2007). To set such limit, we used two observational signposts of HMSF: class II methanol masers and ultra-compact H II (UCH II) regions.

Discovered by Menten (1991), class II methanol masers were found to be exclusively associated with high-mass star forming regions (Minier et al. 2003; Xu et al. 2008; Gallaway et al. 2013; Breen et al. 2013). We cross-correlated our *complete* cores with the published catalogs in Malyshev & Sobolev (2003); Pestalozzi et al. (2005); and Hu et al. (2016) using a positional tolerance of $10''$ (0.07 pc) and found that 10 cores are associated with class II maser sites (see Table D2).

UCH II regions are a product of newly formed (or forming) high-mass stars on their ambient materials and are bright in radio emissions (Churchwell 1990). We used the 3-GHz continuum maps from the VLA Sky Survey (VLASS¹²) to search

for compact radio sources that are associated with our *complete* cores within $10''$. These maps cover the whole Cygnus X region with a resolution of $2.5''$ and a 1σ rms level of $0.1 \text{ mJy} \cdot \text{beam}^{-1}$. To rule out possible radio emissions from low-mass star forming regions (i.e., radio jets or ionized accretion shocks, see Calvet & Gullbring 1998; Anglada et al. 2018), we only selected radio sources with $F_{3\text{GHz}} \geq 0.01$ Jy. The flux limit was set using typical physical values of UCH II regions in Kurtz (2005) (see their Table 3). Consequently, a total of 8 cores were found to be associated with bright compact radio sources (see Table D2).

The lower limit of mass for MDCs was then determined as the minimal mass of cores associated with either of the two HMSF signposts, which is $35 M_{\odot}$ (see Figure 3). Thus 151 out of 205 *complete* cores were defined as MDCs. We name these MDCs in the format of “field name-number”, where the number is the ranking by mass in the fields. See Table 3 for the overview properties of the MDCs, and Table B for their detailed physical properties. See also Figure B1 for a visualization of the MDCs, and Figure E2 for their maps in each band.

3.3. Coincidence of MDCs with Mid-infrared Sources and Infrared Classification

¹² <https://science.nrao.edu/science/surveys/vlass>

To better understand the infrared properties of MDCs, we cross-correlated our MDCs with archival mid-infrared sources. The Cygnus-X Archive catalog¹³ from the *Spitzer* Cygnus-X Legacy Survey (Kraemer et al. 2010) was used preferentially, and the Midcourse Space Experiment (*MSX*) Point Source Catalog¹⁴ was used in the cases where the *Spitzer* images are saturated. Using a positional tolerance of $10''$, we found that 78 and 40 MDCs are associated with *Spitzer* and *MSX* sources, respectively. The mid-infrared flux of each MDC was then determined as the sum of the fluxes of all associated infrared sources. If an MDC does not have any associated infrared sources but shows certain compact emissions in *Spitzer* $24\ \mu\text{m}$ or *MSX* $21\ \mu\text{m}$ maps, its mid-infrared flux was obtained by manual aperture photometry. See Table D1 for the results.

We classified the MDCs into IR-bright/IR-quiet ones following the method of M07. In our case, the mid-IR flux of a B3-type stellar embryo at a distance of 1.4 kpc is $F_{\text{Spitzer } 24\mu\text{m}} = 23\ \text{Jy}$, or $F_{\text{MSX } 21\mu\text{m}} = 17\ \text{Jy}$. MDCs are defined as IR-bright if their mid-IR fluxes exceed this threshold, which indicates that they should already host at least one high-mass ($\geq 8 M_{\odot}$) stellar embryo, or as IR-quiet if it is on the contrary (see Figure 3). Of the 151 MDCs, 15 and 136 MDCs were classified as IR-bright and IR-quiet, respectively. See Table B for the detailed list, Figure B2 for the numbers of different MDCs in each field and Figure 4 for the distributions of physical properties. The surprisingly large proportion of IR-quiet MDCs (90%) is our main deviation from the results of M07 (40%). We will discuss this in Sect. 4.2.2.

High-mass prestellar cores are small (0.01–0.1 pc), dense ($10^5\text{--}10^7\ \text{cm}^{-3}$) entities with no hydrostatic protostellar objects in their centers (McKee & Tan 2002). Since our resolutions can hardly resolve them, we chose to search for MDCs in their earliest evolutionary stages, in which high-mass prestellar cores are most likely to reside (see Motte et al. 2017). We define an MDC as “starless” if it has neither mid-IR (*Spitzer* $24\ \mu\text{m}$ or *MSX* $21\ \mu\text{m}$) sources nor compact $70\ \mu\text{m}$ emissions, and 26 MDCs were found to meet these criteria. Caveats should be made that further observational analyses are still needed to determine whether star-forming activities are absent from these MDCs (i.e., truly “starless”). We found that the candidate of starless MDC N69 (near N68-4 in our catalog) identified in M07 by its possible lack of SiO emissions shows emission peak in the *Herschel* $70\ \mu\text{m}$ data (see the corresponding panels in Figure E2), indicating that it is not truly starless. We will discuss these starless MDCs in Sect. 4.2.3.

4. DISCUSSION

4.1. Dense Regions in Cygnus X

4.1.1. Spatial Correlation with Developed H II Regions

To investigate the spatial distributions of the dense ($N_{\text{H}_2} \geq 3.5 \times 10^{22}\ \text{cm}^{-2}$) regions and (developed) H II regions in Cygnus X, we selected H II regions in the WISE Catalog of Galactic H II Regions (V2.0)¹⁵ (Anderson et al. 2014) with the following criteria: (1) $303^{\circ}.7 \leq \text{ra} \leq 310^{\circ}.5$ and $37^{\circ}.2 \leq \text{dec} \leq 43^{\circ}.2$; (2) radii $r \geq 10\ \text{pc}$; (3) line-of-sight velocity range $-15\ \text{km} \cdot \text{s}^{-1} \leq v_{\text{lsr}} \leq 20\ \text{km} \cdot \text{s}^{-1}$ from the CO survey results of Gottschalk et al. (2012). A total of 7 H II regions were found to meet these criteria (see Table 4). As can be seen in Figure 1, our fields, which cover all the dense regions in Cygnus X, locate preferentially on the edges of or in the spaces between the H II regions. To further analyze the impact of the H II regions on cloud structures, we calculated their radial profiles of column density and temperature (Figure 5). Out of the 7 H II regions, 5 show increasing radial density profiles within their radii, indicating their “cavity-like” density structures. In addition, 6 H II regions have increasing radial temperature profiles within their radii. This seems counter-intuitive since the inner temperature should be higher in a central-heating scenario. However, the central hotness actually can not be reflected in our continuum data since our data traces the molecular components, which have been ionized and depleted in the central regions. Instead, the low temperatures probably come from the cold molecular material along the line-of-sight that do not belong to the H II region. On the contrary, molecular gas on the edge of the H II region suffer less from depletion and are more likely to be heated by the central high-mass stars. These increasing temperature profiles confirm the impact of the H II regions on surrounding materials and indicate that the positional correlation mentioned before should have a causal relation. For the dense regions located on the edges of the H II regions, their formation can be explained by the “collect and collapse” process, which was firstly proposed by Elmegreen & Lada (1977) and supported by follow-up studies (e.g., Elmegreen 1998; Deharveng et al. 2005; Zavagno et al. 2007). In this view, cloud materials are compressed after the passage of shock fronts driven by OB stars, and dense structures (and probably MDCs) are formed due to gravitational instability. On the other hand, the dense regions located in the space between H II regions can not be affected by these shocks. A more reasonable explanation for the positional correlation of these regions would be that the formation of dense regions can not happen within the H II regions due to significant feedbacks. Detailed quantitative analyses are needed to fully

¹³ <https://irsa.ipac.caltech.edu/cgi-bin/Gator/nph-dd>

¹⁴ <https://irsa.ipac.caltech.edu/cgi-bin/Gator/nph-dd>

¹⁵ <http://astro.phys.wvu.edu/wise/>

explain this positional correlation but it is beyond the scope of this paper.

Table 4. Developed H II Regions in Cygnus X

Name	RA _{J2000} (h m s)	DEC _{J2000} (° ′ ″)	R (pc)	v_{lsr} (km · s ⁻¹)
G076.951+01.718	20:19:20.1	+39:11:15	12.1	6.7
G077.402+00.841	20:24:22.4	+39:03:28	26.5	-0.9
G078.698+01.902	20:23:43.8	+40:43:38	19.8	-3.7
G078.714+03.115	20:18:28.8	+41:25:45	22.5	0.9
G079.915-00.504	20:37:43.7	+40:17:30	25.6	1.6
G080.362+01.212	20:31:51.5	+41:40:40	18.2	-12.8
G081.920+00.138	20:41:31.8	+42:16:24	14.7	10.5

4.1.2. Potential of High-mass Star Formation of the Fields

In order to assess the HMSF potential of the fields, we calculated their $M(r) - r$ relations by drawing contours on the column density maps of the fields and measuring mass and size for each contour. The contour levels are exponentially distributed from the background levels to the maxima of the fields, and the sizes are defined as the effective radius: $r = (A/\pi)^{1/2}$, where A is the area of the contour region. The results are shown in Figure 6. As can be seen, most of the fields have $M(r) - r$ relations that can be well fitted by a power-law: $M(r) \propto r^\alpha$. The mean index value of the fields is 1.4. In addition, almost all the fields (with only one exception S01S) meet the HMSF criterion $M(r) \geq 870 M_\odot (r/\text{pc})^{1.33}$ proposed by Kauffmann & Pillai (2010), which supports the notion that most of the fields have potential to form high-mass stars. Interestingly, we found that no obvious systematic deviations of the $M(r) - r$ relation have been found among the fields with and without known HMSF signposts. This indicates that the fields without HMSF signposts are still highly likely to form high-mass stars in the future.

4.2. A New Complete Sample of MDCs in Cygnus X

Our new MDC sample contains 151 cores in Cygnus X with $M \geq 35 M_\odot$. These MDCs have an average size of ~ 0.1 pc, median mass of $60.4 M_\odot$, average temperature of 15.2 K, and a median density of $1.7 \times 10^6 \text{ cm}^{-3}$. Compared with cores in nearby low-mass star forming regions (e.g., Motte et al. 1998; Ward-Thompson et al. 1999), our MDCs have roughly the same sizes but are 1–2 orders of magnitude more massive (and thus denser), which shows the intrinsic HMSF nature of the MDCs. In this subsection, we will provide a detailed comparison between our MDC catalog and the catalog created by M07 (Sect. 4.2.1) and analyze the properties of MDCs and their constraints on HMSF (Sect. 4.2.2 and Sect. 4.2.3)

4.2.1. Comparison with the MDC Sample of M07

Compared with M07, our MDC sample was created using new data (especially the *Herschel* data) and more advanced extraction techniques in a larger spatial coverage. It is necessary and interesting to make a detailed comparison between the two samples.

Using their own source-extraction technique and the *Gaussclumps* program (Stutzki & Guesten 1990; Kramer et al. 1998), M07 identified and characterized a total of 129 cores on their 3-deg² 1.2-mm continuum maps of the IRAM 30 m telescope, which focused on the high-extinction ($A_v \geq 15$) regions in Cygnus X. They further found 42 probable precursors of high-mass stars (i.e., MDCs) out of their core sample by identifying HMSF signposts (embedded H II regions, high infrared luminosity, and strong SiO line emissions). Here we cross-correlated our cores with those of M07 allowing up to 10'' (0.07 pc) offsets. The results are shown in Table B and Figure 2. For the 42 MDCs in M07, 33 (79%) were found to be associated with our MDCs, 6 were “degraded” to be associated to our cores (because of their low masses or poor definitions), and 3 do not have any associations. In the following three paragraphs, we will respectively discuss the unique MDCs in M07, the MDCs in common, and our new MDCs that were not reported in M07.

A total of 9 MDCs in M07 were no longer included in our MDC sample (see Figure 2). These MDCs are N32, N58, N69, NW02, S07, S10, S15, S18, and S26 in M07’s nomenclature. NW02, S07, S10, and S15 are at the low-mass end of M07’s MDC sample. Indeed, these MDCs have masses in M07 all below $30 M_\odot$ and should not be included in our MDC sample. S26 is actually AFGL 2591 and has been excluded from our analysis (see Sect. 1). N58 is surrounded by the shell of an H II region IRAS 20375+4109 (Kothes, & Kerton 2002), and shows no peak but a shell structure in the 70–850 μm continuum and column-density maps. Its peak emission in the 1.2-mm map, by which M07 identified this core, is possibly the result of the contamination of free-free emissions. In our source extraction procedure, N32 was merged into our MDC W75N-1 and N69 was splitted into two cores due to its elongated shape, of which one becomes our MDC N68-4 and the other becomes a low-mass core. Finally, S18 has position and size in M07 that can not fit well with our *Herschel* and column-density maps, and is thus unreliable. It was substituted by our MDC S106-1 of which the position and size are consistent with our data. To summarize, owing to the improved data quality and extraction algorithm, we found that these 9 cores identified in M07 are no longer qualified as MDCs.

By comparing the 33 common MDCs in the two samples (Figure 2), we found that our MDCs have similar sizes as those of M07’s MDCs but are ~ 3.5 times more massive on average (compared with M07). This deviation is due to our

larger extracted fluxes (~ 1.4 times larger in F_V at 1.2 mm), smaller κ_V (e.g., $\kappa_{V,1.2\text{mm}} = 0.00625 \text{ cm}^2\text{g}^{-1}$ in our case versus $0.01 \text{ cm}^2\text{g}^{-1}$ in M07), and colder temperature (average temperature of $\sim 15 \text{ K}$ in our case versus a fixed temperature of 20 K in M07). While the first reason comes from the systematic deviation of the different extraction techniques, the latter two reasons, which jointly increase the mass evaluation by a factor of ~ 2 , truly reflect that the masses of MDCs were probably underestimated in M07. This indicates that MDCs in Cygnus X may be more massive than we expected before.

With our larger data coverage, a great number of MDCs (118) were found that are not in M07’s MDC sample, making our MDC sample three times larger than theirs. Interestingly, these MDCs have physical properties that systematically deviate from those of the MDCs associated with M07’s MDCs: they are generally less massive, colder, and less luminous (see Figure 7). We think this result can be attributed to the relatively high sensitivity and quality of the *Herschel* data (see Table 1). With the help of the powerful *Herschel* equipments, less massive dense-gas entities can be identified. Thus compared with M07, our sample is much more improved in statistical completeness, especially for the most quiescent MDCs.

4.2.2. Interpretations of the Large proportion of IR-quiet MDCs

One unique feature of our MDC sample is that IR-quiet MDCs take up a surprisingly large proportion (90%), compared with other studies using the same techniques, e.g., M07 (40%) and Tigé et al. (2017) (63%). We here propose two interpretations to explain this phenomenon.

One is to assume that all the MDCs (including the IR-quiet ones) are on the evolutionary track of HMSF, as was done in M07 and Tigé et al. (2017). This interpretation can explain the discrepancies of physical properties of MDCs in different infrared classes (see Table 3, Figure 4, and Figure 8): the increasing average temperature and luminosity of the MDCs in starless, IR-quiet but not starless, and IR-bright classes are a consequence of the heating from growing (high-mass) protostars, and the increasing average mass is due to the accretion of MDCs. If we assume that the star formation rate of Cygnus X has remained constant over the past 1–2 Myr, the lifetimes of the MDCs in different stages can be estimated by the number-counting method. For better comparison, we adopted the statistics of OB stars in Cygnus X from M07 ($n_{\text{OB}} = 2600 \pm 1000$, $t_{\text{OB}} = 2 \pm 1 \text{ Myr}$). An average MDC-to-high-mass-star production ratio of 2 was assumed, which was implied by the observational results of Bontemps et al. (2010). In result, the lifetimes of IR-quiet and IR-bright stages are $210 \pm 131 \text{ kyr}$ and $23.1 \pm 15.5 \text{ kyr}$, respectively. The lifetime of IR-quiet stage is even comparable with the whole HMSF timescale, of order $\sim 100 \text{ kyr}$,

proposed by some theoretical and simulation studies (Mayra et al. 1999; Nakano et al. 2000; Behrend & Maeder 2001; McKee & Tan 2002). This indicates that HMSF probably needs to go through a relatively long and quiescent low- to intermediate-mass stage before reaching the more dynamic high-mass stage. This accelerated HMSF scenario was also reported by (Zhang et al. 2005, 2015), who suggested an increasing accretion ratio with protostellar mass based on the CO observations of outflows in HMSF sites, and proposed by theoretical works (Hoyle & Lyttleton 1941; Bondi 1952; Norberg & Maeder 2000; McKee & Tan 2002; Keto 2003).

An alternative interpretation of the large proportion of IR-quiet MDCs is to assume that not all the IR-quiet MDCs are able to form high-mass stars. In this sense, the lower mass, luminosity, and mid-IR flux of the IR-quiet MDCs are due to their intrinsic nature of forming low- to intermediate-mass stars and the true timescale of IR-quiet stage is perhaps much shorter than that of the first scenario. This idea was also supported by Baldeschi et al. (2017), who analyzed the effect of source distance on the identification of HMSF candidates by synthesizing “observational” images of “moved” star-forming clouds. They found that more “false positives” will be identified if low-mass star-forming regions are moved to larger distances, probably because more inter-core emissions will be counted into those of cores. The proportion of IR-quiet MDCs that can form high-mass stars is unclear and only high-resolution studies can provide some hints. For instance, Bontemps et al. (2010) observed six massive IR-quiet MDCs in Cygnus X using the IRAM Plateau de Bure interferometer with resolutions as high as 1700 AU, and found that five of them have massive fragments that are probably precursors of high-mass stars. Duarte-Cabral et al. (2013) studied the CO outflows of the same six MDCs and found that 8 out of 9 high-mass cores (except N53 MM2) are driving outflows stronger than typical low-mass ones. However, their sample is small and biased towards the most massive IR-quiet MDCs.

Both of the interpretations will provide strong constraints on the early evolution of HMSF once validated but unfortunately, we can not yet unravel them based on our data. We expect that this so-called “mass–evolution degeneracy” can be disentangled by comprehensive high-resolution surveys of MDCs using interferometers such as SMA, NOEMA, and ALMA.

4.2.3. Quest for High-mass Prestellar Cores in Cygnus X

We found a total of 26 starless MDCs out of the 151 MDCs by their absence of compact emissions in the *Herschel* 70 μm maps. The average size, mass, and density of these starless MDCs are 0.16 pc , $70 M_{\odot}$, and $7 \times 10^5 \text{ cm}^{-3}$, respectively. With the caveat of the mass–evolutionary degeneracy discussed in Sect. 4.2.2, whether high-mass prestellar cores

exist within these starless MDCs remains unclear. However, with the simple idea that more denser cores are more likely to form high-mass stars, we propose that the 7 starless MDCs of which densities higher than the 1 g cm^{-2} threshold of HMSF proposed by Krumholz & McKee (2008) (see Figure 9) are among the most probable HMSF candidates. These MDCs are N68-5, S43-3, W75N-2, S106W2-6, S11-1, DR21-8, and S106-1, sorted by decreasing densities. It would be interesting to investigate the detailed properties of these MDCs using interferometers to reveal the early stages of HMSF.

5. SUMMARY

As part of the CENSUS project, we aimed at characterizing the physical conditions of high-mass star formation at $\sim 0.1 \text{ pc}$ scales and conducted a complete survey toward the massive dense cores in Cygnus X using space telescope observations of *Spitzer* and *Herschel* as well as ground-based submillimeter and millimeter data. Our results and conclusions are summarized as follows:

1. We generated $5^\circ \times 6^\circ$ mosaic maps of the whole Cygnus X region in the bands of *Herschel* (70, 160, 250, 350, and $500 \mu\text{m}$), JCMT (450 and $850 \mu\text{m}$), and the IRAM 30 m telescope (1.2 mm) (see Figure F3 to F10). A high-resolution column density map (at $18''$, Figure 1) and a temperature map (at $36.7''$, Figure F12) of Cygnus X were also created using the *Herschel* images.
2. With a column density threshold of $3.5 \times 10^{22} \text{ cm}^{-2}$ (corresponding to $A_v \geq 15$) we selected 39 high-density fields in Cygnus X (see Figure 1 and Table A). After the source extraction and SED fitting, 496 cores were identified with well-defined masses and temperatures. Statistical analysis (Sect. 3.2.2) suggests that cores with $M \geq 23.3 M_\odot$ (205 cores) are statistically complete.
3. We cross-correlated the 205 statistically complete cores with two kinds of HMSF signposts: class II methanol masers and UCH II regions (see Sect. 3.2.3 and Table D2). We determined a mass threshold of $35 M_\odot$ for MDCs and selected 151 MDCs. These MDCs have an average size of $\sim 0.1 \text{ pc}$, median mass of $60.4 M_\odot$, average temperature of 15.2 K , and a median density of $1.7 \times 10^6 \text{ cm}^{-3}$ (see Figure 7, Figure B1, and Table B).
4. We matched our core sample with M07’s MDC sample (see Table B and Figure 2) and found that our MDC sample covers most of the MDCs in M07 and is three times larger. Compared with the results of M07 with distance corrected to 1.4 kpc , our MDCs have similar sizes of $\sim 0.1 \text{ pc}$ but are on average ~ 3.5 times more

massive, showing that the masses were probably underestimated before (see Sect. 4.2.1). With more advanced telescopes such as *Herschel*, we are able to find 118 new MDCs that are more quiescent than those in M07.

5. We cross-correlated the MDCs with mid-IR sources of *Spitzer* and *MSX*, and measured their mid-IR fluxes (see Table D1). Nearly two thirds of MDCs were found to be associated with mid-IR sources. We classified the MDCs into 15 IR-bright ones and 136 IR-quiet ones by comparing their mid-IR fluxes with that of a B3-type stellar embryo. We found that the average mass, temperature, and far-IR luminosity of MDCs increase along the “starless-IR-quiet but not starless-IR-bright” sequence, and that starless MDCs are ~ 1.5 times larger than the other MDCs.
6. The large proportion of IR-quiet MDCs (90%) is a unique feature of our sample and we have proposed two possible scenarios of HMSF in Cygnus X to interpret it.
 - (a) Assuming that all the IR-quiet MDCs are able to form high-mass stars, HMSF is probably an accelerated progress with a relatively long ($\sim 200 \text{ kyr}$) IR-quiet stage and a rapid IR-bright stage.
 - (b) Not all the IR-quiet MDCs will form high-mass stars and their quiescent appearance is partly due to their intrinsic nature of forming low- to intermediate-mass stars.

We can not yet determine which one is closer to the truth with our existing data (so-called “mass–evolution degeneracy”). Future high-resolution comprehensive surveys of MDCs are necessary to provide better constraints on HMSF.

7. To search for HMSF at the earliest stages, we identified 26 starless MDCs by their lack of compact $70 \mu\text{m}$ emissions (see Sect. 3.3). With the caveat of the mass–evolutionary degeneracy, it is highly unlikely that all of them will form high-mass stars. However, the 7 densest MDCs with densities exceeding 1 g cm^{-2} are among the most probable HMSF candidates for future studies.
8. To investigate the HMSF potential of the fields, we calculated their $M(r)$ – r relations (see Figure 6). Almost all the fields have $M(r)$ – r relations above the HMSF thresholds $M(r) = 870 M_\odot (r/\text{pc})^{1.33}$ proposed by Kauffmann & Pillai (2010), indicating their high potential of HMSF. Interestingly, no obvious systematic deviations of the $M(r)$ – r relation have been found

among the fields with and without HMSF signposts, which indicates that the fields without HMSF signposts are likely to contain HMSF sites at the earliest stages.

9. We found that the dense regions (covered by our fields) in Cygnus X prefer to locate on the edges of or in the space between the developed ($r \geq 10$ pc) H II regions (see Figure 1). The “cavity-like” density structures and the increasing radial profiles of temperature of the H II regions (see Figure 5) further confirm their impacts on surrounding cloud materials. We here propose that large-scale structures in Cygnus X might be dominated by the expansion of developed H II regions.

Acknowledgments. Y.C., K.Q., J.L., B.H., and Y.W. are supported by National Key R&D Program of China No. 2017YFA0402600. We acknowledge the support from National Natural Science Foundation of China (NSFC) through grants U1731237, 11473011, 11590781 and 11629302.

We are grateful to Alexander Men’shchikov for his help and discussions on *getsources*. This research made use of *Astropy*, a community-developed core Python package for Astronomy ([Astropy Collaboration et al. 2013](#)). This research made use of data products from the Midcourse Space Experiment. Processing of the data was funded by the Ballistic Missile Defense Organization with additional support from NASA Office of Space Science. This research has also made use of the NASA/IPAC Infrared Science Archive, which is operated by the Jet Propulsion Laboratory, California Institute of Technology, under contract with the National Aeronautics and Space Administration. This research used the facilities of the Canadian Astronomy Data Center operated by the the National Research Council of Canada with COMMENT the support of the Canadian Space Agency. This research has made use of the NASA/IPAC Infrared Science Archive, which is operated by the Jet Propulsion Laboratory, California Institute of Technology, under contract

with the National Aeronautics and Space Administration. This research has made use of the SIMBAD database, operated at CDS, Strasbourg, France. This work uses the data of *Herschel*, which is an ESA space observatory with science instruments provided by European-led Principal Investigator consortia and with important participation from NASA. This article makes use of data products from the Wide-field Infrared Survey Explorer, a joint project of the University of California, Los Angeles, and the Jet Propulsion Laboratory/California Institute of Technology, funded by the National Aeronautics and Space Administration. This work is based in part on observations made with the Spitzer Space Telescope, which is operated by the Jet Propulsion Laboratory, California Institute of Technology under a contract with NASA. The images are based on data obtained as part of the Spitzer Space Telescope Cygnus X Legacy Survey (PID 40184, P.I. Joseph L. Hora). This work uses the data of the James Clerk Maxwell Telescope, which is operated by the East Asian Observatory on behalf of The National Astronomical Observatory of Japan; Academia Sinica Institute of Astronomy and Astrophysics; the Korea Astronomy and Space Science Institute; the Operation, Maintenance and Upgrading Fund for Astronomical Telescopes and Facility Instruments, budgeted from the Ministry of Finance (MOF) of China and administrated by the Chinese Academy of Sciences (CAS), as well as the National Key R&D Program of China (No. 2017YFA0402700). Additional funding support is provided by the Science and Technology Facilities Council of the United Kingdom and participating universities in the United Kingdom and Canada. This work is based on observations carried out with the IRAM 30 m telescope. IRAM is supported by INSU/CNRS (France), MPG (Germany) and IGN (Spain).

Facilities: IRAM: 30m, JCMT (SCUBA2), *Herschel* (PACS,SPIRE), *Spitzer* (IRAC,MIPS), *MSX*, *WISE*

Software: *getsources*, *Astropy*

REFERENCES

- Alves, J., Lombardi, M., & Lada, C. J. 2007, *A&A*, 462, L17
- Anderson, L. D., Bania, T. M., Baler, D. S., et al. 2014, *ApJS*, 212, 1
- Anglada, G., Rodríguez, L. F., & Carrasco-González, C. 2018, *Astronomy and Astrophysics Review*, 26, 3.
- Astropy Collaboration, Robitaille, T. P., Tollerud, E. J., et al. 2013, *A&A*, 558, A33
- Baldeschi, A., Elia, D., Molinari, S., et al. 2017, *MNRAS*, 466, 3682.
- Behrend, R., & Maeder, A. 2001, *A&A*, 373, 190
- Bernard, J.-P., Paradis, D., Marshall, D. J., et al. 2010, *A&A*, 518, L88
- Bernasconi, P. A., & Maeder, A. 1996, *A&A*, 307, 829
- Beuther, H., Henning, T., Linz, H., et al. 2010, *A&A*, 518, L78
- Bondi, H. 1952, *MNRAS*, 112, 195
- Bonnell, I. A., & Bate, M. R. 2006, *MNRAS*, 370, 488
- Bonnell, I. A., Bate, M. R., Clarke, C. J., & Pringle, J. E. 2001, *MNRAS*, 323, 785
- Bontemps, S., Motte, F., Csengeri, T., & Schneider, N. 2010, *A&A*, 524, A18

- Breen, S. L., Ellingsen, S. P., Contreras, Y., et al. 2013, *MNRAS*, 435, 524
- Butler, M. J., & Tan, J. C. 2012, *ApJ*, 754, 5
- Calvet, N., & Gullbring, E. 1998, *ApJ*, 509, 802
- Cheng, Y., Tan, J. C., Liu, M., et al. 2018, *ApJ*, 853, 160
- Ching, T.-C., Lai, S.-P., Zhang, Q., et al. 2018, *ApJ*, 865, 110
- Churchwell, E. 1990, *A&A Rv*, 2, 79
- Csengeri, T., Bontemps, S., Schneider, N., Motte, F., & Dib, S. 2011, *A&A*, 527, A135
- Cyganowski, C. J., Brogan, C. L., Hunter, T. R., et al. 2014, *ApJL*, 796, L2
- Deharveng, L., Zavagno, A., & Caplan, J. 2005, *A&A*, 433, 565
- Dickel, H. R., Wendker, H., & Bieritz, J. H. 1969, *A&A*, 1, 270
- Duarte-Cabral, A., Bontemps, S., Motte, F., et al. 2013, *A&A*, 558, A125
- Elmegreen, B. G. 1998, *Origins*, 148, 150
- Elmegreen, B. G., & Lada, C. J. 1977, *ApJ*, 214, 725
- Gallaway, M., Thompson, M. A., Lucas, P. W., et al. 2013, *MNRAS*, 430, 808
- Gottschalk, M., Kothes, R., Matthews, H. E., Landecker, T. L., & Dent, W. R. F. 2012, *A&A*, 541, A79
- Güver, T., & Özel, F. 2009, *MNRAS*, 400, 2050
- Hartmann, L., Ballesteros-Paredes, J., & Heitsch, F. 2012, *MNRAS*, 420, 1457
- Hennemann, M., Motte, F., & Schneider, N. 2014, *The Labyrinth of Star Formation*, 36, 271
- Hoare, M. G., Kurtz, S. E., Lizano, S., et al. 2007, *Protostars and Planets V*, 181.
- Hora, J. 2011, *Herschel Space Observatory Proposal*, id.1667, 1667
- Hoyle, F., & Lyttleton, R. A. 1941, *MNRAS*, 101, 227
- Hu, B., Menten, K. M., Wu, Y., et al. 2016, *ApJ*, 833, 18
- Jacob, J. C., Katz, D. S., Berriman, G. B., et al. 2010, *arXiv:1005.4454*
- Kauffmann, J., & Pillai, T. 2010, *ApJL*, 723, L7
- Keto, E. 2003, *ApJ*, 599, 1196
- Kong, S., Tan, J. C., Caselli, P., et al. 2017, *ApJ*, 834, 193
- Kothes, R., & Kerton, C. R. 2002, *A&A*, 390, 337.
- Kraemer, K. E., Hora, J. L., Adams, J., et al. 2010, *Bulletin of the American Astronomical Society*, 42, 414.01
- Kramer, C., Stutzki, J., Rohrig, R., & Corneliussen, U. 1998, *A&A*, 329, 249
- Krumholz, M. R., Klein, R. I., & McKee, C. F. 2007, *ApJ*, 656, 959
- Krumholz, M. R., & McKee, C. F. 2008, *Nature*, 451, 1082
- Kurtz, S. 2005, *Massive Star Birth: A Crossroads of Astrophysics*, 227, 111
- Larson, R. B. 1981, *MNRAS*, 194, 809
- Lu, X., Zhang, Q., Wang, K., & Gu, Q. 2015, *ApJ*, 805, 171
- Malyshev, A. V., & Sobolev, A. M. 2003, *Astronomical and Astrophysical Transactions*, 22, 1
- Mayra, O., Susana, L., & Paola, D. 1999, *arXiv:astro-ph/9909473*
- McKee, C. F., & Tan, J. C. 2002, *Nature*, 416, 59
- McLaughlin, D. E., & Pudritz, R. E. 1997, *ApJ*, 476, 750
- Men'shchikov, A., André, P., Didelon, P., et al. 2012, *A&A*, 542, A81
- Men'shchikov, A. 2017, *A&A*, 607, A64
- Menten, K. M. 1991, *ApJL*, 380, L75
- Minier, V., Ellingsen, S. P., Norris, R. P., & Booth, R. S. 2003, *A&A*, 403, 1095
- Molinari, S., Swinyard, B., Bally, J., et al. 2010, *PASP*, 122, 314
- Motte, F., André, P., & Neri, R. 1998, *A&A*, 336, 150
- Motte, F., Bontemps, S., & Louvet, F. 2017, *arXiv:1706.00118*
- Motte, F., Bontemps, S., Schilke, P., et al. 2007, *A&A*, 476, 1243
- Motte, F., Zavagno, A., Bontemps, S., et al. 2010, *A&A*, 518, L77
- Nakano, T., Hasegawa, T., Morino, J.-I., & Yamashita, T. 2000, *ApJ*, 534, 976
- Norberg, P., & Maeder, A. 2000, *A&A*, 359, 1025
- Ohashi, S., Sanhueza, P., Chen, H.-R. V., et al. 2016, *ApJ*, 833, 209
- Peretto, N., Fuller, G. A., André, P., et al. 2014, *A&A*, 561, A83
- Pestalozzi, M. R., Minier, V., & Booth, R. S. 2005, *A&A*, 432, 737
- Pipenbrink, A., & Wendker, H. J. 1988, *A&A*, 191, 313
- Rathborne, J. M., Jackson, J. M., & Simon, R. 2006, *ApJ*, 641, 389
- Rygl, K. L. J., Brunthaler, A., Sanna, A., et al. 2012, *A&A*, 539, A79
- Schilke, P. 2017, *arXiv e-prints*, *arXiv:1712.05281*.
- Schneider, N., Bontemps, S., Simon, R., et al. 2006, *A&A*, 458, 855
- Schneider, N., Simon, R., Kramer, C., Stutzki, J., & Bontemps, S. 2002, *A&A*, 384, 225
- Shepherd, D. S., Kurtz, S. E., & Testi, L. 2004, *ApJ*, 601, 952
- Shu, F. H., Adams, F. C., & Lizano, S. 1987, *ARA&A*, 25, 23
- Stutzki, J., & Guesten, R. 1990, *ApJ*, 356, 513
- Tan, J. C. 2018, *IAU Symposium*, 139.
- Tan, J. C., Kong, S., Butler, M. J., Caselli, P., & Fontani, F. 2013, *ApJ*, 779, 96
- Tan, J. C., Beltrán, M. T., Caselli, P., et al. 2014, *Protostars and Planets VI*, 149.
- Tan, J. C., & McKee, C. F. 2002, *Hot Star Workshop III: The Earliest Phases of Massive Star Birth*, 267.
- Tigé, J., Motte, F., Russeil, D., et al. 2017, *A&A*, 602, A77
- Uyaniker, B., Fürst, E., Reich, W., Aschenbach, B., & Wielebinski, R. 2001, *A&A*, 371, 675
- Wang, Y., Beuther, H., Zhang, Q., et al. 2012, *ApJ*, 754, 87
- Wang, K., Zhang, Q., Testi, L., et al. 2014, *MNRAS*, 439, 3275
- Ward-Thompson, D., Motte, F., & André, P. 1999, *MNRAS*, 305, 143
- Wendker, H. J., Higgs, L. A., & Landecker, T. L. 1991, *A&A*, 241, 551
- Xu, Y., Li, J. J., Hachisuka, K., et al. 2008, *A&A*, 485, 729
- Xu, Y., Li, J. J., Reid, M. J., et al. 2013, *ApJ*, 769, 15

Zavagno, A., Pomarès, M., Deharveng, L., et al. 2007, *A&A*, 472, 835
Zhang, Q., Hunter, T. R., Brand, J., et al. 2005, *ApJ*, 625, 864
Zhang, Q., Wang, K., Lu, X., & Jiménez-Serra, I. 2015, *ApJ*, 804, 141
Zhang, Q., Wang, Y., Pillai, T., & Rathborne, J. 2009, *ApJ*, 696, 268

Zinnecker, H., & Yorke, H. W. 2007, *Annual Review of Astronomy and Astrophysics*, 45, 481.

Ziurys, L. M., & Friberg, P. 1987, *ApJL*, 314, L49

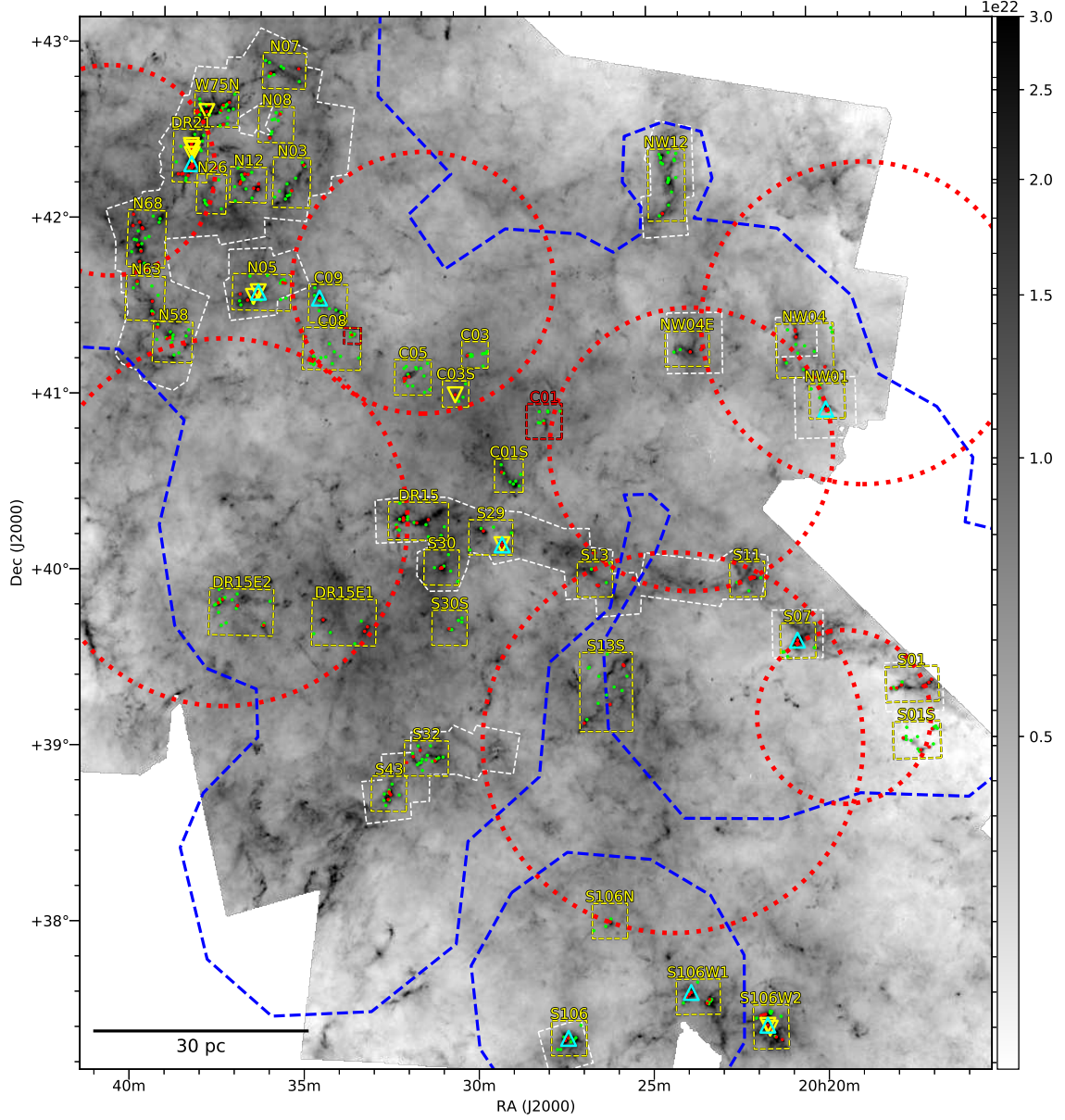


Figure 1. High-resolution ($18''$) N_2H_2 map of Cygnus X derived from *Herschel* images, units are in cm^{-2} . Yellow dashed rectangles represent the fields considered in this paper, which cover dense regions ($N_{H_2} \geq 3.5 \times 10^{22} \text{cm}^{-2}$) in Cygnus X. Regions in red dashed rectangles are excluded from our analysis due to their inconsistent distances (see Sect. 3.2.1). Blue and white dashed polygons outline the coverages of the JCMT and IRAM 30 m telescope images, respectively. Green and red dots mark the positions of our cores and MDCs, respectively, extracted by *getsources* (see Sect. 3.2.2). UCH II regions and sites of class II methanol masers are marked as cyan and yellow triangles, respectively (see Sect. 3.2.3). Developed H II regions in Cygnus X are represented as dotted red circles (see Sect. 4.1.1).

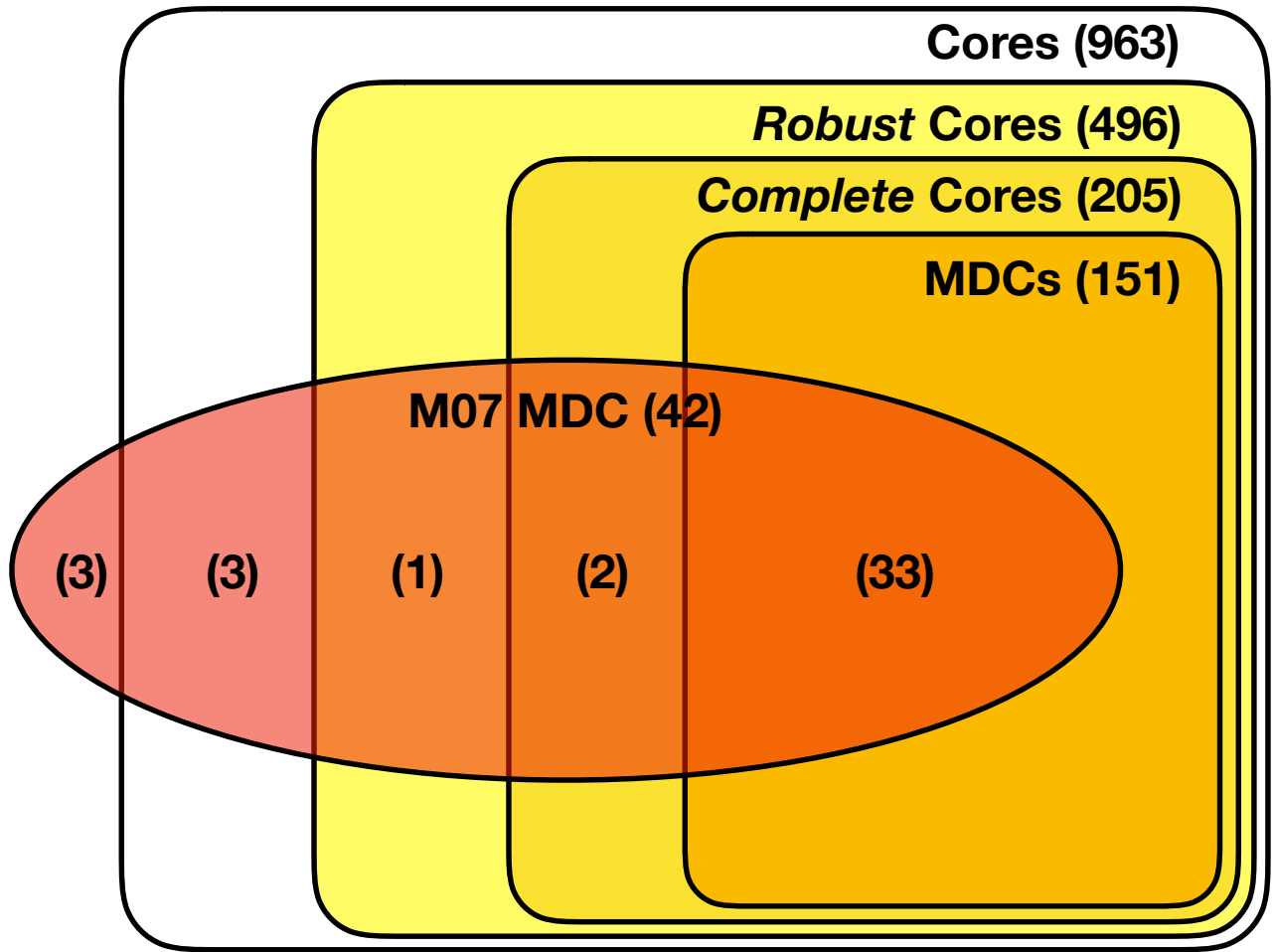


Figure 2. Venn diagram of the core/MDC samples in this paper and in [M07](#). Sizes of the samples and the intersections are shown in brackets.

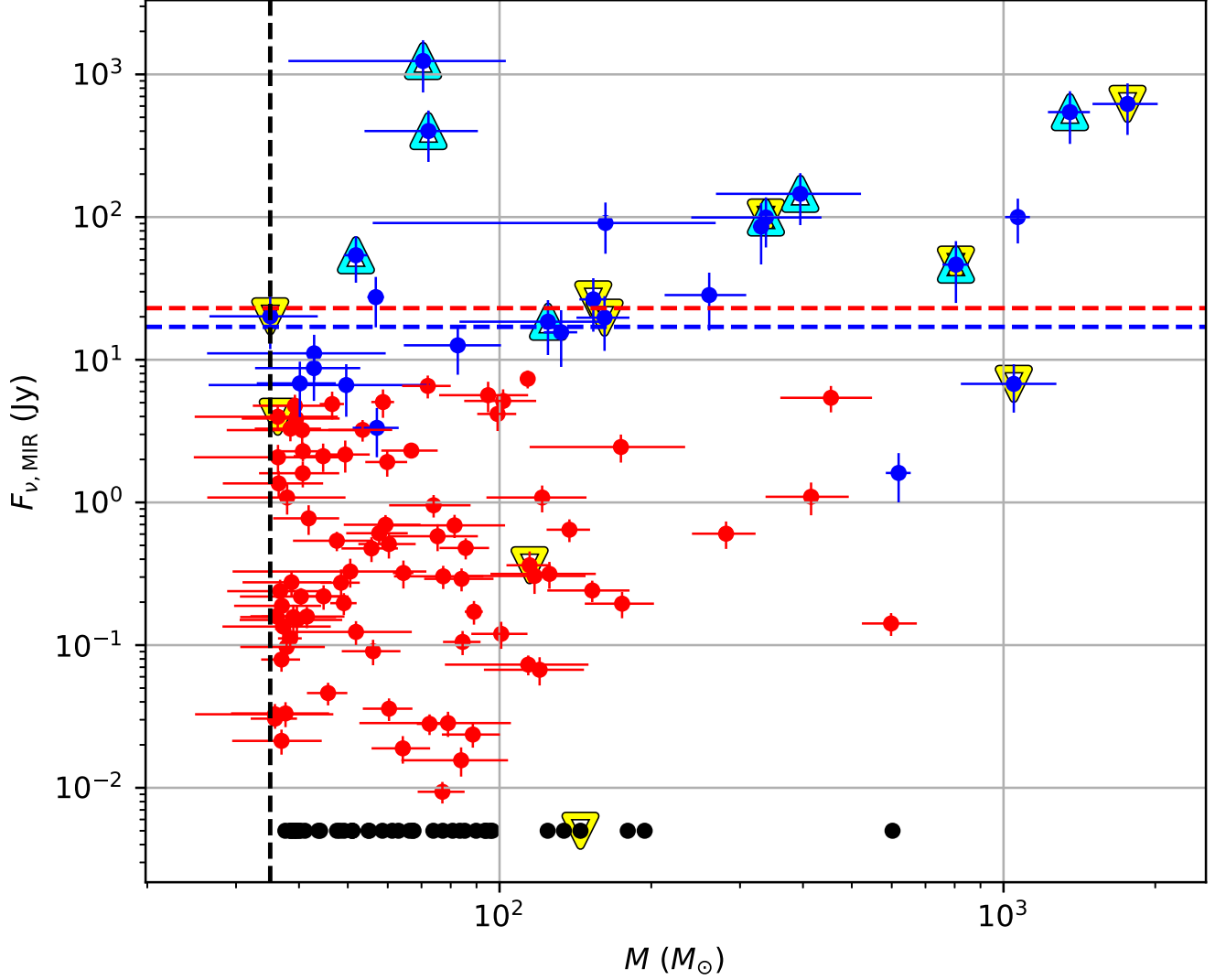


Figure 3. Mid-IR flux (red for *Spitzer* 24 μm , blue for *MSX* 21 μm , and black for the 5 mJy detection limit of *Spitzer* at 24 μm) versus mass diagram of the MDCs in Cygnus X. MDCs associated with UCH II regions and class II methanol masers are attached with cyan and yellow triangles, respectively. Black vertical dashed line shows the 35- M_{\odot} mass threshold for defining MDCs (see Sect. 3.2.3). Red and blue dashed lines are the 23-Jy (*Spitzer* 24 μm) and 17-Jy (*MSX* 21 μm) thresholds separating IR-bright/IR-quiet MDCs (see Sect. 3.3).

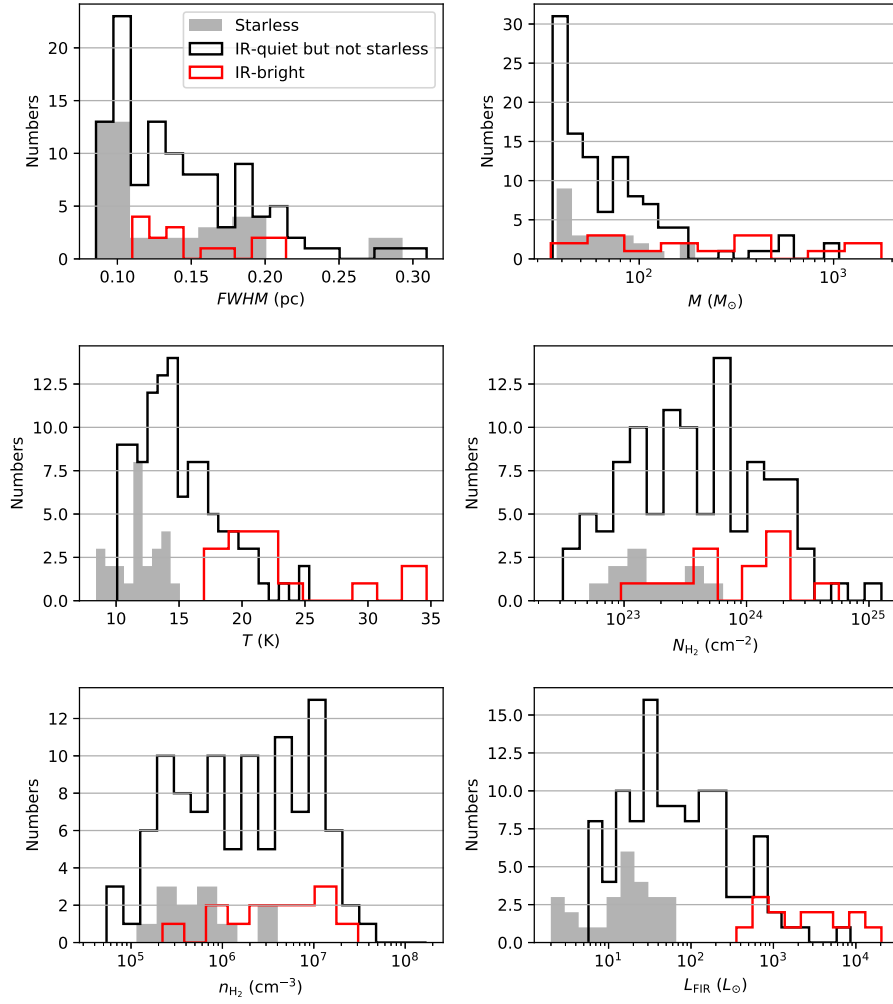


Figure 4. Distributions of the *convolved* FWHM sizes (at *Herschel* 160 μm), masses, dust temperatures, H_2 column and volume densities, and far-IR luminosities of the MDCs in different infrared classes.

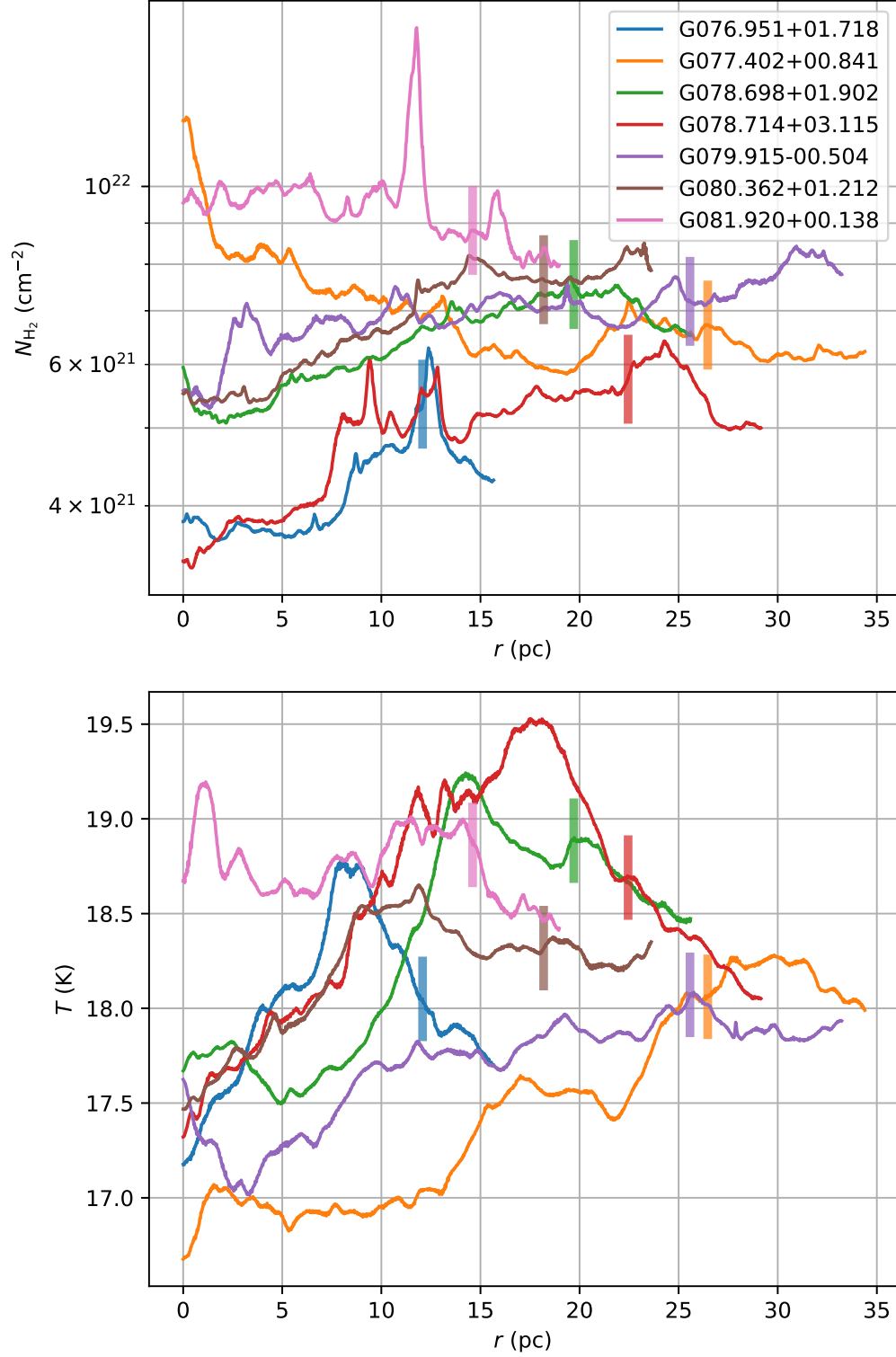


Figure 5. Radial profiles of column density (up) and temperature (bottom) of the 7 developed H II regions in Cygnus X (see Sect. 4.1.1). Radial distance range is from the centers of the H II regions to 1.3 times of their radii (marked by short vertical segments).

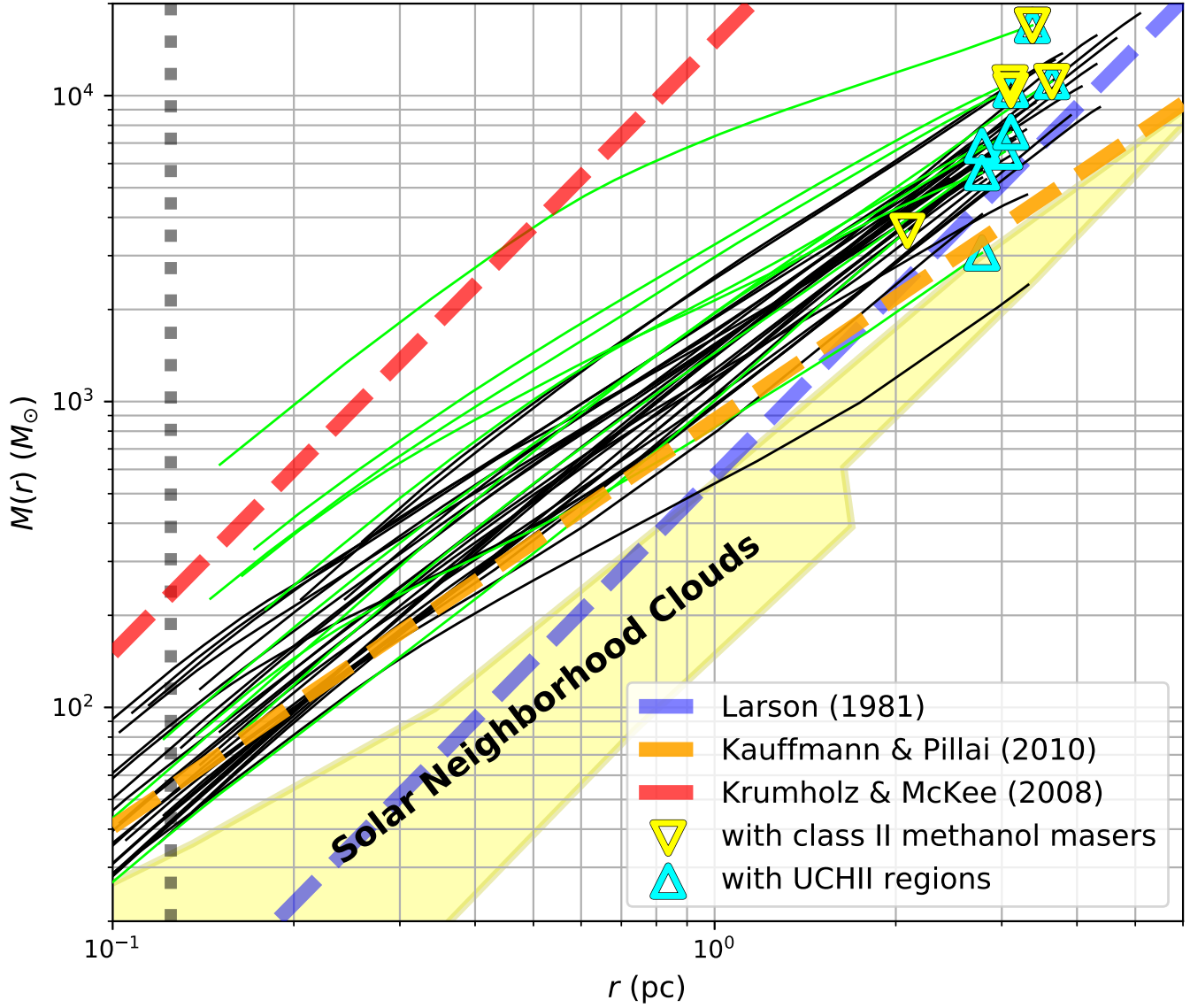


Figure 6. $M(r)$ – r relations of the fields as solid curves (see Sect. 4.1.2). Fields containing HMSF signposts have the corresponding curves colored green and attached with triangles. The vertical dotted line shows the resolution of the column density map ($18''$). Blue, orange, and red dashed lines represent the relations of Larson (1981) ($M(r) = 572 M_{\odot} (r/\text{pc})^2$), Kauffmann & Pillai (2010) ($M(r) = 870 M_{\odot} (r/\text{pc})^{1.33}$), and Krumholz & McKee (2008) (1 g cm^{-2}), respectively. The yellow range of solar neighborhood clouds were from Figure 2 of Kauffmann & Pillai (2010).

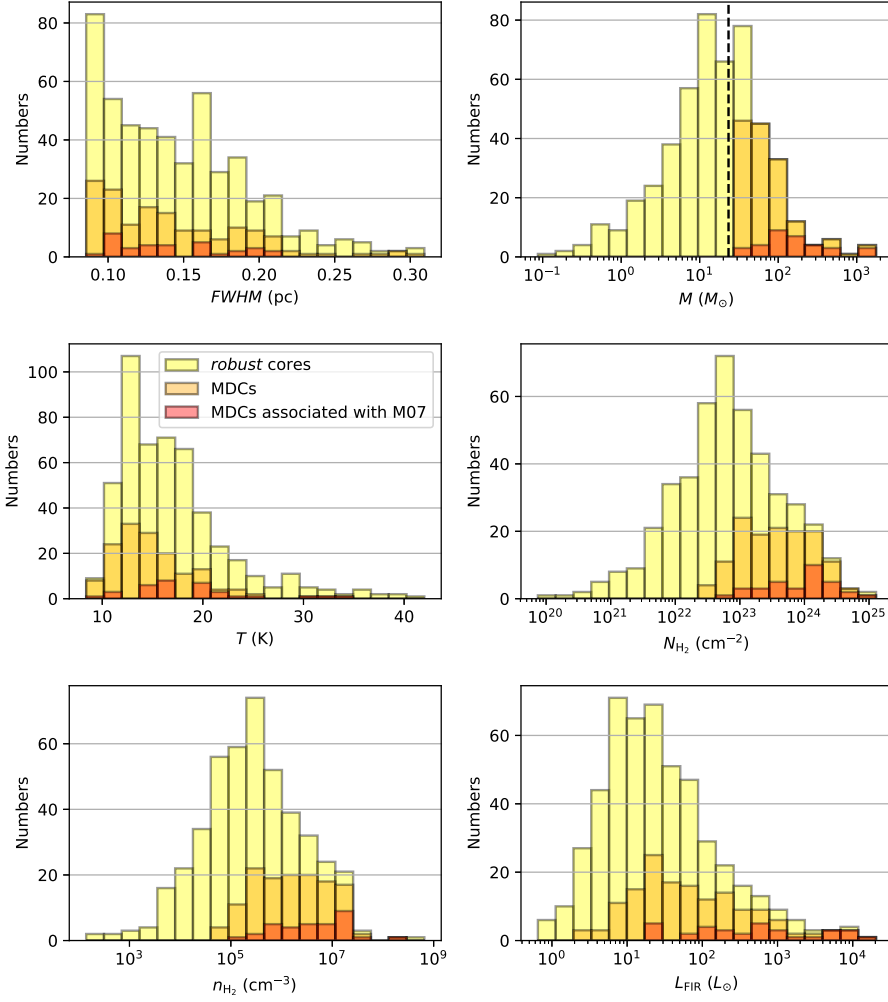


Figure 7. Distributions of the *convolved* FWHM sizes (at *Herschel* 160 μm), masses, dust temperatures, H_2 column and volume densities, and far-IR luminosities of the *robust core* sample, the MDC sample, and the MDCs that are associated with the MDCs in M07 (Sect. 4.2.1). In the “mass” panel, cores with masses larger than the critical mass represented as the vertical dashed line ($23.3 M_{\odot}$) are statistically complete (see Sect. 3.2.1).

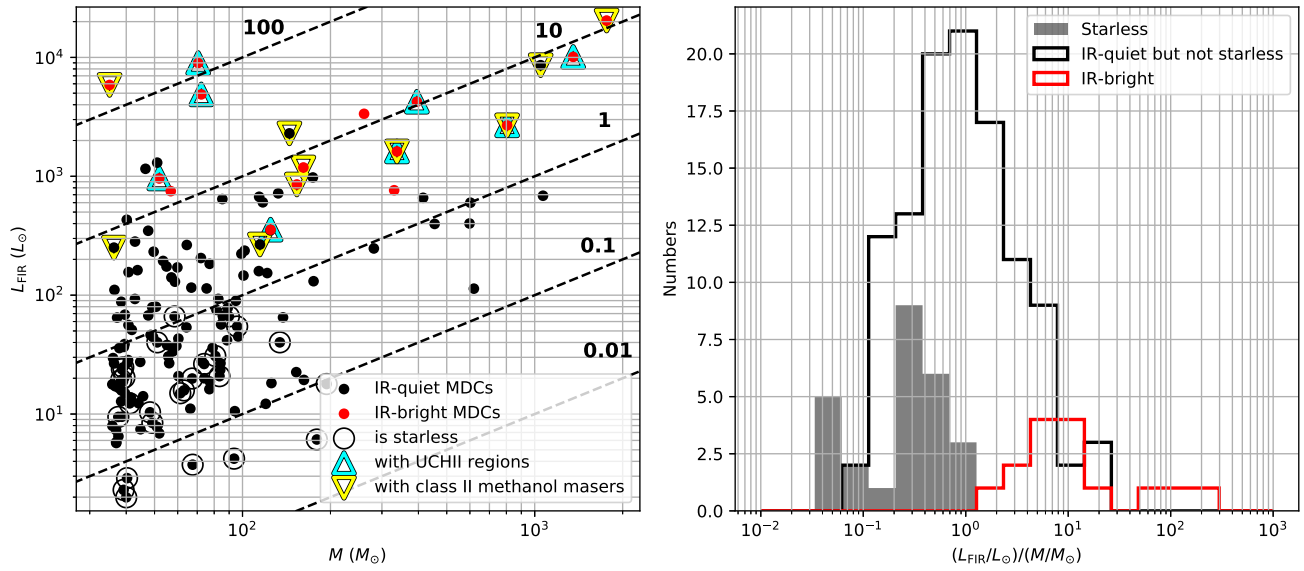


Figure 8. *Left:* luminosity–mass diagram of the MDCs in Cygnus X. Dashed lines are the $L/M = \text{const.}$ curves with the constant values near them. *Right:* distributions of the L/M ratios of different kinds of MDCs. It is clear that L/M ratios increase along the sequence: starless–IR-quiet but not starless–IR-bright.

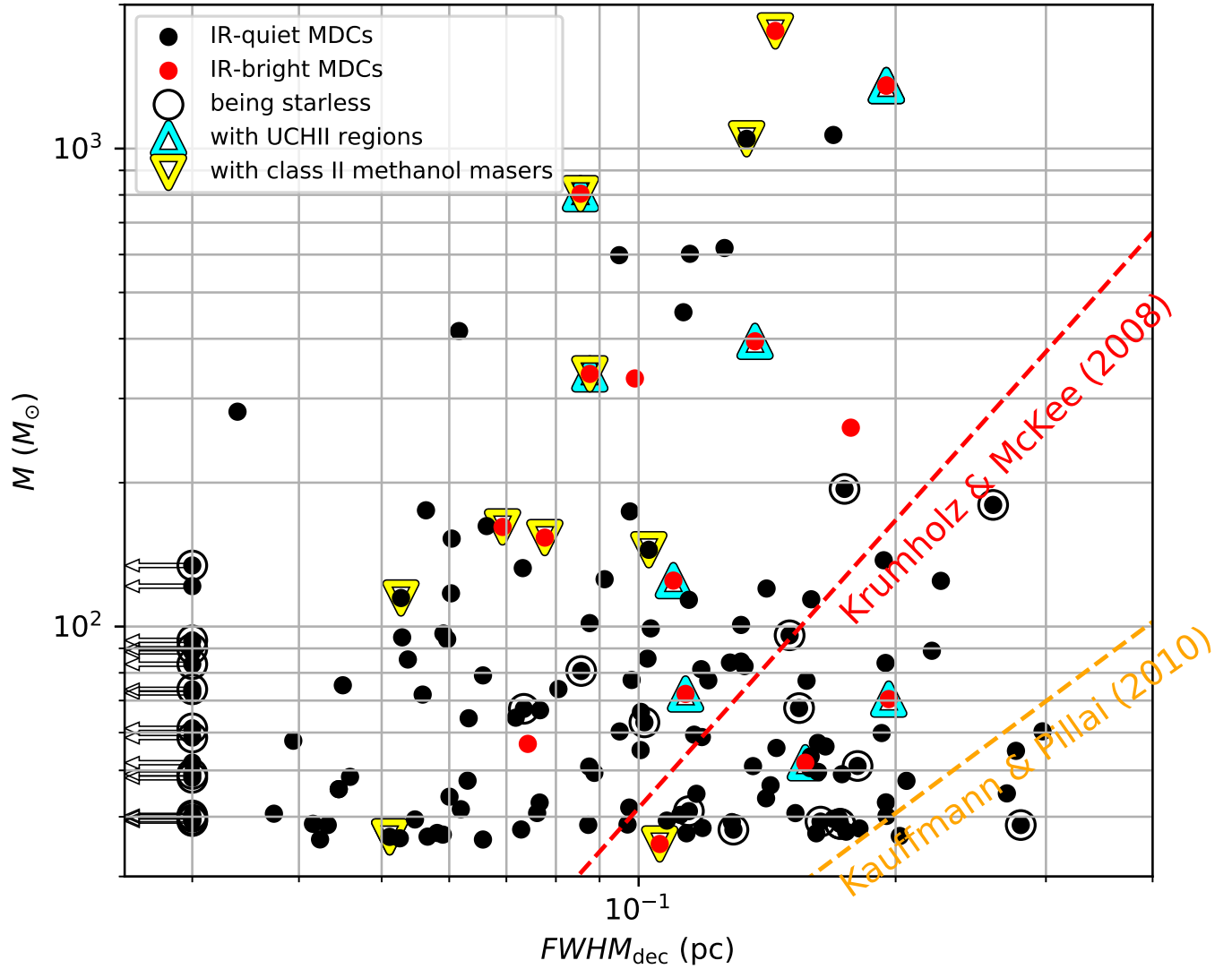


Figure 9. Mass–size diagram of the MDCs in Cygnus X. Sizes are presented as deconvolved FWHM sizes at *Herschel* $160 \mu\text{m}$. MDCs with sizes smaller than the *Herschel* beam at $160 \mu\text{m}$ are attached with left arrows. The infrared classes and the signposts of HMSF of the MDCs are explained in the legend. Two HMSF thresholds are shown as dashed lines: column density $= 1 \text{ g cm}^{-2}$ proposed by Krumholz & McKee (2008) (red), and $M(r) = 870 M_{\odot} (r/\text{pc})^{1.33}$ proposed by Kauffmann & Pillai (2010) (orange).

APPENDIX

A. FIELDS USED FOR CORE EXTRACTION

To extract MDCs in Cygnus X, we selected 39 high-density rectangular fields using a column density threshold of $3.5 \times 10^{22} \text{cm}^{-2}$. The threshold guarantees that cores with $M_{\text{core}} \geq 23.3 M_{\odot}$ extracted in the fields are statistically complete (see Sect. 3.2.1). Table A lists the geometric information and the numbers of cores in the fields.

Table A. Fields in Cygnus X Used for Core Extraction

Name	RA _{J2000} (h m s)	DEC _{J2000} (° ' ")	Width (°)	Height (°)	$N_{\text{robust}}^{\text{a}}$	$N_{\text{complete}}^{\text{b}}$	$N_{\text{MDC}}^{\text{c}}$
C01S	20:29:12.9	+40:35:00	0.16	0.19	8	2	1
C03	20:30:15.4	+41:16:12	0.15	0.15	11	2	1
C03S	20:30:50.1	+41:02:45	0.15	0.15	4	1	1
C05	20:32:07.9	+41:08:15	0.21	0.20	17	6	4
C08	20:34:36.1	+41:17:38	0.33	0.24	16	3	3
C09	20:34:44.7	+41:33:01	0.22	0.22	13	4	2
DR15	20:31:54.8	+40:19:08	0.34	0.22	19	10	7
DR15E1	20:34:05.3	+39:44:11	0.37	0.26	7	3	3
DR15E2	20:37:08.3	+39:46:55	0.37	0.26	20	6	4
DR21	20:39:04.3	+42:22:19	0.20	0.30	34	24	23
N03	20:35:55.9	+42:14:06	0.21	0.28	12	3	2
N05	20:36:46.3	+41:36:24	0.33	0.21	24	8	6
N07	20:36:14.4	+42:52:12	0.24	0.20	10	5	2
N08	20:36:27.0	+42:33:47	0.20	0.20	9	4	2
N12	20:37:16.0	+42:12:58	0.21	0.20	17	10	7
N26	20:38:23.2	+42:09:31	0.17	0.23	6	1	1
N58	20:39:26.1	+41:18:31	0.22	0.23	16	7	4
N63	20:40:18.6	+41:33:08	0.22	0.25	10	4	3
N68	20:40:19.8	+41:53:30	0.22	0.32	20	12	8
NW01	20:19:36.5	+40:59:24	0.20	0.20	6	1	1
NW04	20:20:14.7	+41:16:46	0.32	0.31	14	5	5
NW04E	20:23:48.8	+41:18:01	0.25	0.20	4	3	2
NW12	20:24:23.7	+42:14:05	0.21	0.41	19	2	1
S01	20:17:17.8	+39:21:53	0.30	0.20	9	7	6
S01S	20:17:12.5	+39:02:47	0.27	0.21	15	4	4
S07	20:20:38.2	+39:37:43	0.20	0.20	6	2	1
S11	20:22:06.5	+39:59:00	0.20	0.20	6	4	3
S13	20:26:38.7	+39:59:27	0.20	0.20	6	3	2

Table A continued

Table A (*continued*)

Name	RA _{J2000} (h m s)	DEC _{J2000} (° ' ")	Width (°)	Height (°)	$N_{\text{robust}}^{\text{a}}$	$N_{\text{complete}}^{\text{b}}$	$N_{\text{MDC}}^{\text{c}}$
S13S	20:26:19.5	+39:20:56	0.30	0.45	14	4	4
S29	20:29:44.9	+40:13:47	0.25	0.20	6	1	1
S30	20:31:12.5	+40:03:23	0.20	0.20	8	3	3
S30S	20:30:57.4	+39:42:47	0.20	0.20	6	2	1
S32	20:31:36.2	+38:58:05	0.25	0.20	18	7	4
S43	20:32:41.2	+38:45:53	0.20	0.20	12	8	4
S106	20:27:25.7	+37:22:49	0.20	0.20	10	5	2
S106N	20:26:14.6	+38:02:45	0.20	0.20	4	1	1
S106W1	20:23:43.0	+37:36:39	0.25	0.20	15	8	7
S106W2	20:21:38.1	+37:26:05	0.20	0.25	16	12	9
W75N	20:38:18.5	+42:38:32	0.25	0.20	29	8	6

^aNumber of *robust* cores (with well-defined fluxes, temperatures, and masses, see Sect. 3.2.2) in each field.

^bNumber of *complete* cores (*robust* cores with $M_{\text{core}} \geq 23.3 M_{\odot}$, which means they are statistically complete in Cygnus X, see Sect. 3.2.2) in each field.

^cNumber of MDCs (*complete* cores with $M_{\text{core}} \geq 35 M_{\odot}$, see Sect. 3.2.3) in each field.

B. PHYSICAL PROPERTIES OF THE MDCS IN CYGNUS X

In this appendix, Figure B1 visualizes all the MDCs in Cygnus X, Figure B2 shows the numbers of different MDCs in each field, and Table B lists the detailed physical properties and classifications of the MDCs.

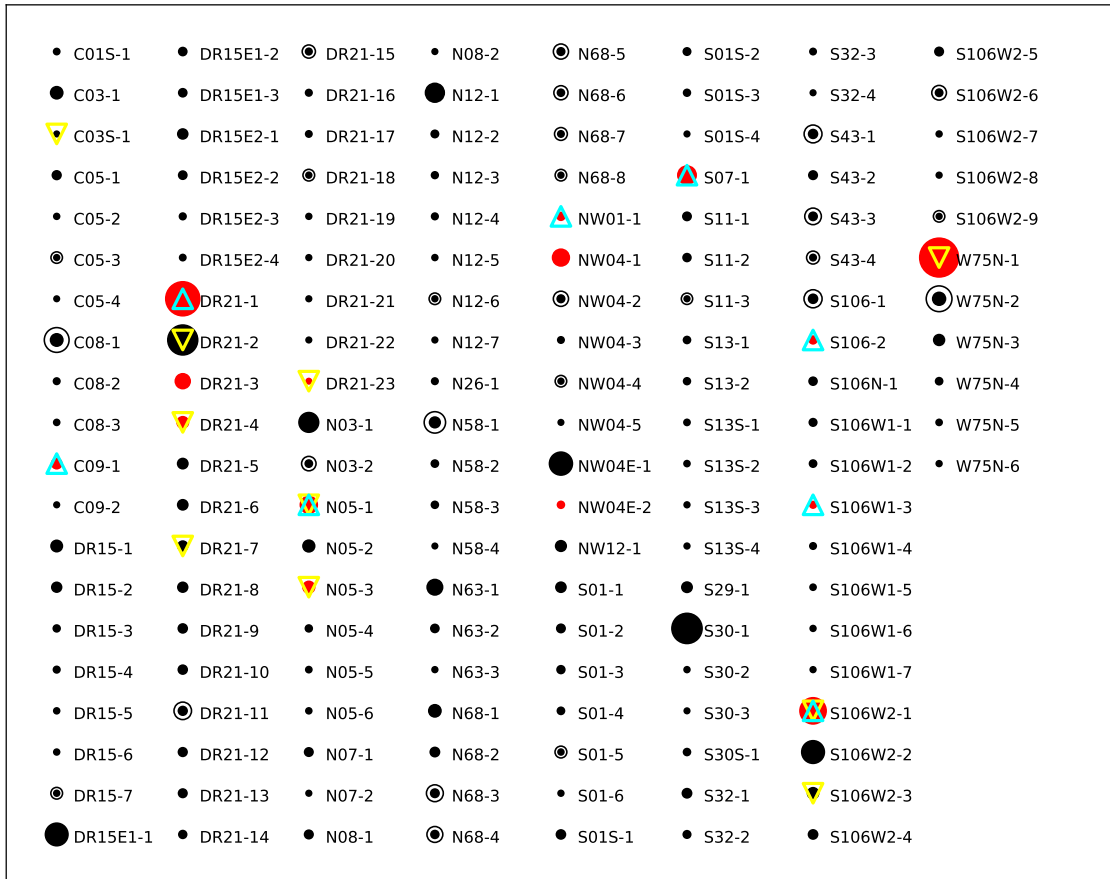


Figure B1. Assembly of the MDCs in Cygnus X in alphabetical order. Each (black/red) dot represents an (IR-quiet/IR-bright) MDC with its area proportional to the mass of the MDC. Dots will be attached with open circles/cyan triangles/yellow triangles if the corresponding MDCs are starless/associated with UCH II regions/associated with class II methanol masers.

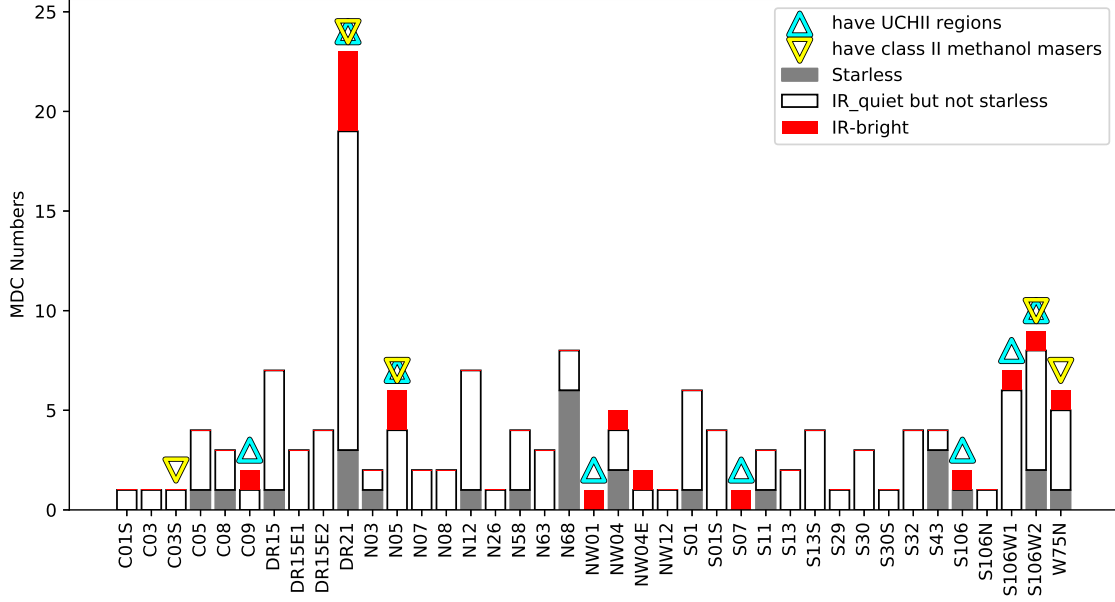


Figure B2. Stacked-bar plot of the numbers of MDCs in each field. MDCs in different infrared classes are described in the legend. Triangle markers will be added to the bar tops if the corresponding fields contain MDCs that are associated with HMSF signposts.

Table B. Properties of MDCs in Cygnus X

Name	Name in M07 ^a	RA _{J2000}	DEC _{J2000}	<i>FWHM</i> ^b	<i>T</i> ^c	<i>M</i> ^c	<i>N</i> _{H₂} ^d	<i>n</i> _{H₂} ^e	<i>L</i> _{FIR} ^f	Classification ^g
		(h m s)	(° ′ ″)	(pc)	(K)	(<i>M</i> _⊙)	(10 ²² cm ⁻²)	(10 ⁵ cm ⁻³)	(<i>L</i> _⊙)	
C01S-1		20:29:25.87	+40:36:05.2	0.045 (0.096)	12.1±0.4	45.7±4.2	118.7	122.7	14.1	IR-quiet
C03-1		20:30:28.90	+41:15:55.4	0.098 (0.130)	19.7±3.6	174±59.4	94.1	44.3	977	IR-quiet
C03S-1		20:30:50.78	+41:02:28.6	0.051 (0.100)	20.4±3.6	36.3±11.5	71.7	64.6	251	IR-quiet
C05-1		20:32:23.84	+41:07:52.8	0.221 (0.237)	14.4±0.2	89.0±3.7	9.4	2.0	78.0	IR-quiet
C05-2		20:32:21.06	+41:07:54.9	0.037 (0.093)	13.9±1.6	40.6±11.8	149.7	184.2	28.4	IR-quiet
C05-3		20:32:14.90	+41:08:28.4	0.172 (0.192)	13.6±1.5	38.6±10.7	6.7	1.8	23.8	starless
C05-4		20:32:23.20	+41:06:50.3	0.066 (0.108)	13.1±1.5	35.8±11.0	42.8	30.0	17.8	IR-quiet
C08-1		20:35:24.28	+41:21:33.1	0.260 (0.274)	8.4±0.9	180±64.6	13.7	2.4	6.11	starless
C08-2		20:35:07.55	+41:13:55.8	0.162 (0.183)	19.1±4.7	49.6±23.2	9.7	2.8	232	IR-quiet
C08-3		20:35:10.33	+41:13:10.3	0.195 (0.213)	20.2±4.3	42.9±16.6	5.8	1.4	282	IR-quiet
C09-1		20:34:59.62	+41:34:48.7	0.110 (0.139)	17.6±2.9	125±41.5	53.3	22.3	356	IR-bright
C09-2		20:34:50.22	+41:33:58.8	0.161 (0.183)	10.8±0.7	36.9±7.5	7.3	2.1	5.79	IR-quiet
DR15-1	S34	20:31:57.78	+40:18:32.6	0.060 (0.105)	10.7±0.7	153±28.4	215.9	164.5	22.5	IR-quiet
DR15-2	S37	20:32:21.92	+40:20:14.5	0.114 (0.143)	15.6±0.2	114±3.2	44.7	18.0	159	IR-quiet
DR15-3		20:32:22.07	+40:19:22.3	0.145 (0.168)	13.4±0.7	55.7±7.1	13.7	4.3	30.5	IR-quiet
DR15-4	S41	20:32:33.53	+40:16:56.6	0.136 (0.161)	25.3±2.1	51.0±6.0	14.2	4.8	1302	IR-quiet
DR15-5		20:31:37.13	+40:19:41.0	0.062 (0.106)	12.3±0.9	41.5±7.8	55.8	41.5	13.8	IR-quiet
DR15-6		20:32:21.13	+40:19:42.3	0.153 (0.175)	15.6±1.3	40.7±7.4	9.0	2.7	56.1	IR-quiet

Table B continued

Table B (continued)

Name	Name in M07 ^a	RA _{J2000}	DEC _{J2000}	<i>FWHM</i> ^b	<i>T</i> ^c	<i>M</i> ^c	<i>N</i> _{H₂} ^d	<i>n</i> _{H₂} ^e	<i>L</i> _{FIR} ^f	Classification ^g
		(h m s)	(° ' ")	(pc)	(K)	(<i>M</i> _⊙)	(10 ²² cm ⁻²)	(10 ⁵ cm ⁻³)	(<i>L</i> _⊙)	
DR15-7		20:32:30.34	+40:14:07.5	... (0.086)	9.5±4.0	40.3±26.0	≥31.3	≥17.8	2.89	starless
DR15E1-1		20:34:42.34	+39:44:56.5	0.095 (0.128)	13.8±0.7	598±74.7	342.5	166.1	401	IR-quiet
DR15E1-2		20:33:23.33	+39:42:47.4	0.098 (0.130)	11.7±0.8	77.3±15.6	41.4	19.4	18.8	IR-quiet
DR15E1-3		20:33:28.25	+39:41:14.1	0.157 (0.179)	11.4±0.4	77.0±8.2	16.1	4.7	16.2	IR-quiet
DR15E2-1		20:37:42.16	+39:51:08.2	0.060 (0.105)	19.4±2.8	117±30.8	166.5	127.1	604	IR-quiet
DR15E2-2		20:37:49.56	+39:49:54.2	0.066 (0.108)	13.0±1.6	79.0±26.3	94.3	66.1	36.0	IR-quiet
DR15E2-3		20:36:27.86	+39:42:39.5	... (0.086)	10.5±0.9	51.9±15.1	≥40.3	≥22.9	6.88	IR-quiet
DR15E2-4		20:37:15.19	+39:49:07.2	0.143 (0.166)	25.2±0.9	46.5±2.6	11.8	3.8	1156	IR-quiet
DR21-1	N46	20:39:01.03	+42:19:33.8	0.195 (0.213)	20.6±1.2	1355±130	183.5	43.3	10095	IR-bright
DR21-2	N44	20:39:00.89	+42:22:48.8	0.134 (0.159)	21.0±2.8	1048±225	301.7	103.7	8600	IR-quiet
DR21-3	N48	20:39:01.39	+42:22:04.2	0.177 (0.197)	22.6±2.8	261±48.0	42.8	11.1	3353	IR-bright
DR21-4	N51	20:39:02.13	+42:25:01.0	0.078 (0.116)	19.7±0.7	153±9.4	131.3	77.8	853	IR-bright
DR21-5		20:38:54.06	+42:19:12.7	0.226 (0.242)	17.5±1.6	125±21.0	12.6	2.6	351	IR-quiet
DR21-6		20:39:01.11	+42:18:34.7	... (0.086)	15.4±2.1	121±27.3	≥94.3	≥53.6	153	IR-quiet
DR21-7	N53	20:39:03.03	+42:25:50.3	0.053 (0.100)	17.0±0.9	115±11.5	213.1	186.2	267	IR-quiet
DR21-8	N40	20:38:59.62	+42:23:47.2	0.159 (0.181)	19.8±3.6	114±36.1	23.2	6.7	672	IR-quiet
DR21-9	N56	20:39:16.84	+42:16:10.0	0.053 (0.101)	14.6±1.4	94.9±19.0	175.2	152.6	89.7	IR-quiet
DR21-10		20:39:19.41	+42:15:59.1	0.060 (0.104)	10.3±0.6	94.1±16.3	136.3	105.1	10.6	IR-quiet
DR21-11		20:39:06.25	+42:18:16.4	... (0.086)	14.0±3.7	89.9±42.1	≥69.8	≥39.7	66.3	starless
DR21-12		20:38:51.65	+42:27:14.5	... (0.086)	13.0±0.9	88.5±11.7	≥68.7	≥39.1	41.7	IR-quiet
DR21-13	N38	20:38:58.95	+42:22:23.7	0.054 (0.101)	20.7±10.3	85.3±68.3	152.7	131.0	643	IR-quiet
DR21-14		20:39:02.01	+42:26:55.6	... (0.086)	12.6±0.3	72.6±4.1	≥56.4	≥32.1	27.6	IR-quiet
DR21-15		20:38:59.82	+42:27:32.5	0.180 (0.200)	14.2±0.7	51.1±6.3	8.1	2.1	40.1	starless
DR21-16		20:39:00.76	+42:18:12.7	0.159 (0.180)	15.9±3.2	50.6±21.0	10.3	3.0	79.9	IR-quiet
DR21-17		20:38:58.42	+42:18:51.5	0.206 (0.223)	20.6±2.1	47.6±8.6	5.8	1.3	348	IR-quiet
DR21-18		20:39:25.49	+42:15:59.6	... (0.086)	10.0±0.9	40.0±2.3	≥31.1	≥17.7	1.99	starless
DR21-19		20:39:02.12	+42:16:53.0	0.169 (0.189)	16.2±1.3	39.6±6.2	7.1	1.9	68.6	IR-quiet
DR21-20		20:39:02.63	+42:18:41.3	0.119 (0.146)	14.6±1.9	37.9±11.6	13.8	5.4	35.9	IR-quiet
DR21-21	N52	20:39:02.86	+42:26:23.3	0.175 (0.195)	16.2±1.7	37.2±9.0	6.3	1.6	64.8	IR-quiet
DR21-22		20:39:07.30	+42:15:33.9	0.202 (0.220)	17.8±2.1	36.5±8.2	4.6	1.0	111	IR-quiet
DR21-23	N43	20:39:00.35	+42:24:35.7	0.106 (0.136)	34.7±7.2	35.1±8.5	16.1	7.0	5865	IR-bright
N03-1	N03	20:35:34.23	+42:20:10.0	0.113 (0.142)	14.4±1.4	455±93.9	184.0	75.0	397	IR-quiet
N03-2		20:35:55.55	+42:11:19.9	... (0.086)	11.7±0.4	61.2±3.7	≥47.5	≥27.0	15.0	starless
N05-1	N10	20:36:52.25	+41:36:22.9	0.088 (0.122)	19.2±2.9	338±97.6	226.6	118.9	1619	IR-bright
N05-2	N06	20:36:08.21	+41:39:56.4	0.066 (0.108)	10.4±2.1	162±106	189.8	131.6	19.4	IR-quiet
N05-3	N14	20:37:01.02	+41:34:55.9	0.069 (0.110)	20.6±1.4	162±19.5	173.6	115.3	1186	IR-bright
N05-4		20:37:11.61	+41:33:36.2	0.166 (0.186)	13.1±0.7	56.1±7.5	10.6	2.9	26.8	IR-quiet
N05-5		20:37:25.41	+41:35:37.6	0.117 (0.145)	13.6±0.7	44.7±5.6	16.9	6.6	27.5	IR-quiet
N05-6		20:36:03.55	+41:39:45.2	0.097 (0.130)	15.3±1.0	41.8±6.3	22.7	10.7	51.0	IR-quiet
N07-1		20:36:39.61	+42:51:12.6	0.195 (0.213)	11.9±1.1	83.9±20.1	11.4	2.7	23.5	IR-quiet
N07-2		20:35:47.47	+42:52:58.4	0.073 (0.112)	11.0±0.8	37.6±8.3	36.5	23.1	6.49	IR-quiet
N08-1		20:36:38.36	+42:29:12.0	0.102 (0.133)	14.2±0.7	85.7±9.7	42.1	18.9	67.2	IR-quiet
N08-2		20:36:19.87	+42:37:27.4	0.058 (0.103)	10.8±0.7	37.0±7.3	56.6	44.8	5.71	IR-quiet
N12-1	N12	20:36:57.48	+42:11:31.2	0.062 (0.105)	15.9±1.5	415±78.0	563.8	421.1	659	IR-quiet
N12-2		20:36:56.83	+42:13:22.5	0.063 (0.106)	14.3±0.8	64.3±8.6	82.9	60.3	53.6	IR-quiet

Table B continued

Table B (continued)

Name	Name in M07 ^a	RA _{J2000}	DEC _{J2000}	<i>FWHM</i> ^b	<i>T</i> ^c	<i>M</i> ^c	<i>N</i> _{H₂} ^d	<i>n</i> _{H₂} ^e	<i>L</i> _{FIR} ^f	Classification ^g
		(h m s)	(° ′ ″)	(pc)	(K)	(<i>M</i> _⊙)	(10 ²² cm ⁻²)	(10 ⁵ cm ⁻³)	(<i>L</i> _⊙)	
N12-3		20:37:16.89	+42:16:31.3	0.159 (0.181)	18.3±1.5	53.5±7.8	10.9	3.2	194	IR-quiet
N12-4		20:37:22.89	+42:16:37.9	0.088 (0.122)	10.8±0.3	50.9±4.6	34.3	18.0	7.82	IR-quiet
N12-5		20:37:30.10	+42:13:59.3	0.076 (0.114)	18.5±1.2	40.7±5.0	36.3	22.0	156	IR-quiet
N12-6		20:37:31.27	+42:13:16.6	0.163 (0.184)	13.7±0.7	39.1±4.9	7.6	2.1	24.7	starless
N12-7		20:37:05.74	+42:11:50.9	0.181 (0.201)	12.9±1.0	37.8±7.2	5.9	1.5	16.5	IR-quiet
N26-1		20:38:21.03	+42:11:31.1	0.089 (0.123)	14.5±0.8	49.4±5.9	32.3	16.8	44.4	IR-quiet
N58-1		20:39:54.24	+41:23:26.7	... (0.086)	12.1±1.5	134±26.3	≥104.2	≥59.2	40.1	starless
N58-2		20:39:31.02	+41:20:04.7	0.193 (0.211)	17.6±0.9	59.9±5.7	8.3	2.0	171	IR-quiet
N58-3	N60	20:39:36.15	+41:19:37.5	0.162 (0.183)	17.2±0.9	57.1±6.0	11.2	3.2	141	IR-quiet
N58-4		20:39:03.55	+41:17:48.2	0.042 (0.095)	11.5±0.4	35.9±3.8	103.1	112.0	7.96	IR-quiet
N63-1	N63	20:40:05.43	+41:32:13.0	0.034 (0.092)	14.4±0.9	282±40.6	1263.3	1715.0	247	IR-quiet
N63-2		20:40:03.92	+41:27:54.3	0.121 (0.148)	17.1±2.7	77.2±24.0	27.3	10.4	184	IR-quiet
N63-3		20:40:34.26	+41:38:46.3	0.129 (0.154)	13.1±1.2	39.0±8.4	12.2	4.3	18.8	IR-quiet
N68-1	N68	20:40:33.56	+41:59:03.0	0.056 (0.102)	14.1±1.0	175±27.4	284.2	232.1	131	IR-quiet
N68-2	N65	20:40:28.43	+41:57:11.2	0.088 (0.122)	17.0±1.4	102±16.6	68.2	35.8	237	IR-quiet
N68-3		20:40:45.49	+41:57:50.6	... (0.086)	11.7±0.5	83.4±7.3	≥64.7	≥36.8	20.8	starless
N68-4		20:40:34.94	+41:51:18.1	... (0.086)	12.4±2.1	73.9±24.5	≥57.4	≥32.6	26.4	starless
N68-5		20:40:27.51	+41:56:54.3	0.073 (0.113)	12.1±0.7	67.3±10.0	64.4	40.4	19.9	starless
N68-6		20:40:29.11	+41:49:12.9	... (0.086)	15.1±0.4	58.6±2.2	≥45.5	≥25.8	66.2	starless
N68-7		20:40:31.24	+41:45:35.3	... (0.086)	11.4±1.8	48.2±16.1	≥37.5	≥21.3	10.3	starless
N68-8		20:40:45.36	+42:01:41.1	... (0.086)	13.2±1.5	39.4±8.1	≥30.6	≥17.4	20.3	starless
NW01-1	NW01	20:19:38.95	+40:56:39.3	0.113 (0.142)	29.8±5.6	72.3±18.3	28.9	11.7	4887	IR-bright
NW04-1	NW05	20:20:30.57	+41:21:26.4	0.099 (0.131)	17.0±0.3	330±12.2	173.8	80.8	763	IR-bright
NW04-2		20:20:31.31	+41:23:25.7	0.154 (0.176)	9.1±0.2	67.5±6.4	14.6	4.4	3.75	starless
NW04-3		20:19:39.20	+41:11:01.8	0.046 (0.097)	14.7±0.5	48.5±4.3	118.5	118.8	46.3	IR-quiet
NW04-4		20:20:52.51	+41:13:47.6	... (0.086)	9.2±0.5	39.2±6.1	≥30.4	≥17.3	2.30	starless
NW04-5		20:20:31.85	+41:23:52.9	0.053 (0.100)	14.3±0.7	36.1±4.0	67.4	59.1	29.6	IR-quiet
NW04E-1		20:23:43.43	+41:16:59.1	0.126 (0.152)	11.1±0.2	619±35.2	200.8	73.3	113	IR-quiet
NW04E-2		20:23:23.64	+41:17:39.7	0.074 (0.113)	22.7±0.5	56.8±2.2	53.3	33.0	750	IR-bright
NW12-1	NW14	20:24:31.63	+42:04:21.0	0.073 (0.113)	19.6±0.9	133±10.1	127.6	80.3	719	IR-quiet
S01-1		20:16:48.57	+39:22:16.2	0.141 (0.165)	10.1±0.7	120±27.0	31.1	10.1	12.2	IR-quiet
S01-2		20:17:55.73	+39:20:38.4	0.133 (0.158)	15.1±1.3	82.6±18.0	24.1	8.3	93.0	IR-quiet
S01-3		20:16:58.96	+39:21:05.7	0.056 (0.102)	17.6±1.0	72.0±8.0	119.1	98.1	205	IR-quiet
S01-4		20:17:45.79	+39:20:40.4	0.095 (0.128)	14.0±0.7	60.3±7.9	34.4	16.7	43.1	IR-quiet
S01-5		20:17:37.19	+39:21:38.9	0.115 (0.143)	12.1±0.8	41.1±8.0	16.2	6.5	12.3	starless
S01-6		20:16:43.64	+39:23:19.2	0.055 (0.102)	14.7±1.2	39.5±8.7	68.0	57.2	38.8	IR-quiet
S01S-1		20:16:45.52	+39:06:27.7	0.059 (0.104)	13.0±0.5	96.7±10.9	142.9	111.3	44.8	IR-quiet
S01S-2		20:17:36.97	+39:03:35.0	0.072 (0.112)	18.7±0.4	64.5±3.0	64.5	41.3	264	IR-quiet
S01S-3		20:17:06.58	+38:59:17.4	0.277 (0.290)	17.9±1.4	54.9±9.7	3.7	0.6	174	IR-quiet
S01S-4		20:16:51.91	+39:00:13.5	0.114 (0.142)	11.3±0.3	36.9±3.3	14.7	5.9	7.32	IR-quiet
S07-1	S08	20:20:39.10	+39:37:51.1	0.137 (0.161)	21.9±4.1	395±126	108.7	36.6	4239	IR-bright
S11-1		20:22:20.15	+39:58:18.1	0.118 (0.146)	14.6±1.7	81.4±21.2	29.9	11.6	75.2	IR-quiet
S11-2		20:21:53.56	+39:59:33.4	0.081 (0.117)	11.9±0.8	74.0±13.6	58.8	33.6	20.0	IR-quiet
S11-3		20:21:56.83	+39:59:38.3	0.129 (0.155)	11.7±2.3	37.6±16.1	11.6	4.1	9.46	starless
S13-1		20:26:32.31	+39:57:20.4	0.119 (0.146)	16.9±0.4	58.7±3.1	21.5	8.4	130	IR-quiet

Table B continued

Table B (continued)

Name	Name in M07 ^a	RA _{J2000}	DEC _{J2000}	FWHM ^b	T ^c	M ^c	N _{H₂} ^d	n _{H₂} ^e	L _{FIR} ^f	Classification ^g
		(h m s)	([∘] ' ")	(pc)	(K)	(M _⊙)	(10 ²² cm ⁻²)	(10 ⁵ cm ⁻³)	(L _⊙)	
S13-2		20:26:34.82	+39:57:26.5	0.101 (0.132)	13.9±0.4	55.1±3.7	28.1	12.9	38.1	IR-quiet
S13S-1		20:26:58.32	+39:10:19.5	0.270 (0.283)	11.0±0.3	44.8±4.8	3.2	0.5	7.45	IR-quiet
S13S-2		20:25:49.02	+39:30:14.7	0.077 (0.115)	16.8±1.7	42.8±10.1	37.7	22.6	92.9	IR-quiet
S13S-3		20:26:12.55	+39:16:42.9	0.042 (0.095)	11.7±0.7	38.7±7.8	115.5	127.9	9.49	IR-quiet
S13S-4		20:25:47.68	+39:29:54.2	0.043 (0.096)	12.3±0.2	38.4±2.1	106.0	112.8	12.8	IR-quiet
S29-1	S29	20:29:58.20	+40:15:58.7	0.091 (0.125)	10.7±0.8	126±29.7	77.8	39.2	18.2	IR-quiet
S30-1		20:31:11.73	+40:03:12.8	0.169 (0.189)	13.7±0.3	1068±60.4	192.5	52.4	686	IR-quiet
S30-2		20:31:14.59	+40:03:05.5	0.112 (0.141)	13.8±1.3	40.4±9.8	16.6	6.8	27.0	IR-quiet
S30-3	S30	20:31:12.80	+40:03:22.6	0.057 (0.103)	14.0±2.0	36.3±11.6	58.5	47.6	26.7	IR-quiet
S30S-1		20:30:58.19	+39:42:26.2	0.039 (0.094)	13.5±0.7	57.7±8.1	191.6	223.8	33.6	IR-quiet
S32-1	S32	20:31:20.94	+38:57:17.7	0.132 (0.157)	15.7±1.0	101±12.9	29.9	10.4	146	IR-quiet
S32-2		20:32:10.71	+38:56:35.5	0.101 (0.132)	11.0±0.6	66.3±11.7	33.7	15.4	11.1	IR-quiet
S32-3		20:31:59.21	+38:58:38.5	0.063 (0.106)	15.7±0.8	47.6±4.8	61.7	45.1	67.5	IR-quiet
S32-4		20:31:47.25	+39:00:48.6	0.059 (0.104)	13.0±1.0	36.7±7.9	54.4	42.5	17.1	IR-quiet
S43-1		20:32:42.44	+38:43:54.6	... (0.086)	8.8±0.9	93.6±20.3	≥72.6	≥41.3	4.21	starless
S43-2	S43	20:32:41.01	+38:46:30.1	0.132 (0.157)	13.8±0.5	84.5±7.2	25.1	8.8	56.7	IR-quiet
S43-3		20:32:40.31	+38:46:06.8	0.086 (0.121)	12.6±1.3	80.7±21.2	56.7	30.5	30.8	starless
S43-4		20:32:38.17	+38:45:33.8	... (0.086)	11.0±0.4	49.1±4.9	≥38.1	≥21.7	8.43	starless
S106-1		20:27:32.23	+37:22:02.8	0.150 (0.173)	13.4±1.5	95.9±26.9	21.9	6.7	54.5	starless
S106-2	S20	20:27:27.57	+37:22:51.6	0.196 (0.214)	33.1±12.1	70.5±32.4	9.4	2.2	8971	IR-bright
S106N-1		20:26:14.16	+38:02:26.5	0.045 (0.097)	15.8±1.4	75.4±15.2	191.6	195.8	114	IR-quiet
S106W1-1		20:23:23.49	+37:35:37.5	0.077 (0.115)	16.2±1.0	66.8±8.6	58.6	35.2	116	IR-quiet
S106W1-2		20:24:06.19	+37:35:51.4	0.297 (0.309)	12.4±0.5	60.4±6.8	3.5	0.5	20.8	IR-quiet
S106W1-3		20:23:54.90	+37:38:10.7	0.157 (0.198)	24.0±0.8	51.9±2.8	10.9	3.2	958	IR-bright
S106W1-4		20:23:58.34	+37:37:31.7	0.173 (0.193)	16.0±0.4	49.1±3.0	8.5	2.2	79.1	IR-quiet
S106W1-5		20:23:57.46	+37:39:50.6	0.141 (0.165)	18.4±1.0	43.7±3.9	11.3	3.7	162	IR-quiet
S106W1-6		20:23:27.80	+37:34:25.2	0.172 (0.192)	12.6±1.0	39.6±9.1	6.9	1.9	14.9	IR-quiet
S106W1-7		20:24:02.66	+37:36:37.8	0.087 (0.122)	17.0±1.2	38.5±5.8	26.0	13.7	88.0	IR-quiet
S106W2-1		20:21:44.31	+37:26:41.0	0.085 (0.121)	18.0±0.5	805±47.9	567.6	305.5	2684	IR-bright
S106W2-2		20:21:39.24	+37:25:12.0	0.115 (0.143)	14.8±1.1	602±115	235.5	94.3	600	IR-quiet
S106W2-3		20:21:41.11	+37:25:33.8	0.103 (0.134)	23.4±3.6	145±38.6	70.6	31.6	2297	IR-quiet
S106W2-4		20:21:47.65	+37:30:20.9	0.103 (0.134)	16.9±0.7	99.1±8.8	47.9	21.3	223	IR-quiet
S106W2-5		20:21:55.47	+37:29:57.3	0.128 (0.154)	12.2±0.6	84.1±13.2	26.5	9.5	26.7	IR-quiet
S106W2-6		20:21:51.26	+37:26:03.8	0.102 (0.133)	11.7±1.1	63.0±18.2	31.5	14.3	15.8	starless
S106W2-7		20:21:51.06	+37:30:12.8	0.195 (0.213)	21.9±2.1	40.2±7.2	5.4	1.3	431	IR-quiet
S106W2-8		20:21:29.94	+37:22:35.9	0.097 (0.129)	12.7±0.6	38.5±5.8	21.1	10.0	15.8	IR-quiet
S106W2-9		20:21:19.59	+37:21:39.1	0.280 (0.293)	13.2±0.4	38.4±3.0	2.5	0.4	19.4	starless
W75N-1	N30	20:38:36.44	+42:37:34.1	0.145 (0.168)	22.2±2.0	1762±261	434.6	138.3	20413	IR-bright
W75N-2	N24	20:38:05.93	+42:39:54.2	0.174 (0.194)	9.9±0.6	194±38.9	32.9	8.7	17.9	starless
W75N-3		20:38:33.04	+42:39:47.2	0.194 (0.212)	13.0±0.5	138±13.6	18.9	4.5	65.0	IR-quiet
W75N-4		20:38:10.16	+42:38:07.1	0.116 (0.144)	13.7±0.9	59.4±10.3	22.7	9.0	37.4	IR-quiet
W75N-5		20:38:05.17	+42:33:19.8	0.060 (0.104)	11.9±0.6	44.0±7.3	63.0	48.3	12.3	IR-quiet
W75N-6		20:37:55.06	+42:40:54.8	0.108 (0.138)	14.6±1.1	39.3±6.9	17.4	7.4	36.7	IR-quiet

Table B continued

Table B (*continued*)

Name	Name in M07 ^a	RA _{J2000}	DEC _{J2000}	<i>FWHM</i> ^b	<i>T</i> ^c	<i>M</i> ^c	<i>N</i> _{H₂} ^d	<i>n</i> _{H₂} ^e	<i>L</i> _{FIR} ^f	Classification ^g
		(h m s)	(° ' ")	(pc)	(K)	(<i>M</i> _⊙)	(10 ²² cm ⁻²)	(10 ⁵ cm ⁻³)	(<i>L</i> _⊙)	

^a Names of the MDCs in M07 that are associated with our MDCs with a positional tolerance of 10" (see Sect. 4.2.1).

^b Deconvolved (convolved) FWHM sizes in the *Herschel* 160 μm band. Ellipses will show where convolved sizes are smaller than the *Herschel* beam.

^c Dust temperatures and masses were obtained by SED fitting (Sect. 3.2.2). The errors in come from the flux uncertainties and the fitting errors.

^d Estimated as $N_{\text{H}_2} = \frac{4}{\pi} \frac{M}{\mu_{\text{H}_2} m_{\text{H}} FWHM_{\text{dec}}^2}$.

^e Estimated as $n_{\text{H}_2} = \frac{6}{\pi} \frac{M}{\mu_{\text{H}_2} m_{\text{H}} FWHM_{\text{dec}}^3}$.

^f Estimated as $L_{\text{FIR}} = 4\pi D^2 \int_0^{+\infty} \frac{\kappa_{\nu} B_{\nu}(T) M}{D^2} d\nu$.

^g Infrared classifications of the MDCs (see Sect. 3.3). Note that starless MDCs also belong to IR-quiet MDCs.

C. FAR-INFRARED TO MILLIMETER FLUXES OF THE MDCS AND SED FITTING

Fluxes of the MDCs in the bands of *Herschel* (70, 160, 250, 350, and 500 μm), JCMT (450 and 850 μm), and the IRAM 30 m telescope (1.2 mm) were extracted by *getsources* on the single-frequency maps of the fields (see Sect. 3.2.2). Large-scale emissions in the maps were firstly removed before flux extraction by setting the “maxsize” parameter in *getsources* to 35'' (0.23 pc). The results are shown in Table C.

We used the ≥ 160 μm fluxes and a modified blackbody model to do the SED fitting (see Sect. 3.2.2). During the fitting, we found that some fluxes deviate largely from the model curve (see Figure C). These poorly-measured fluxes are due to source blending in low-resolution images (e.g., S30-2@500 μm , DR15-2@350 μm , see the corresponding panels in Figure E2) and poor image quality (e.g., C09-2@450 μm , N05-5@450 μm). Given that the errors provided by *getsources* did not reflect the poor detections, we have manually removed these points from the SED fitting after careful by-eye inspection. The removed fluxes are enclosed in brackets in Table C.

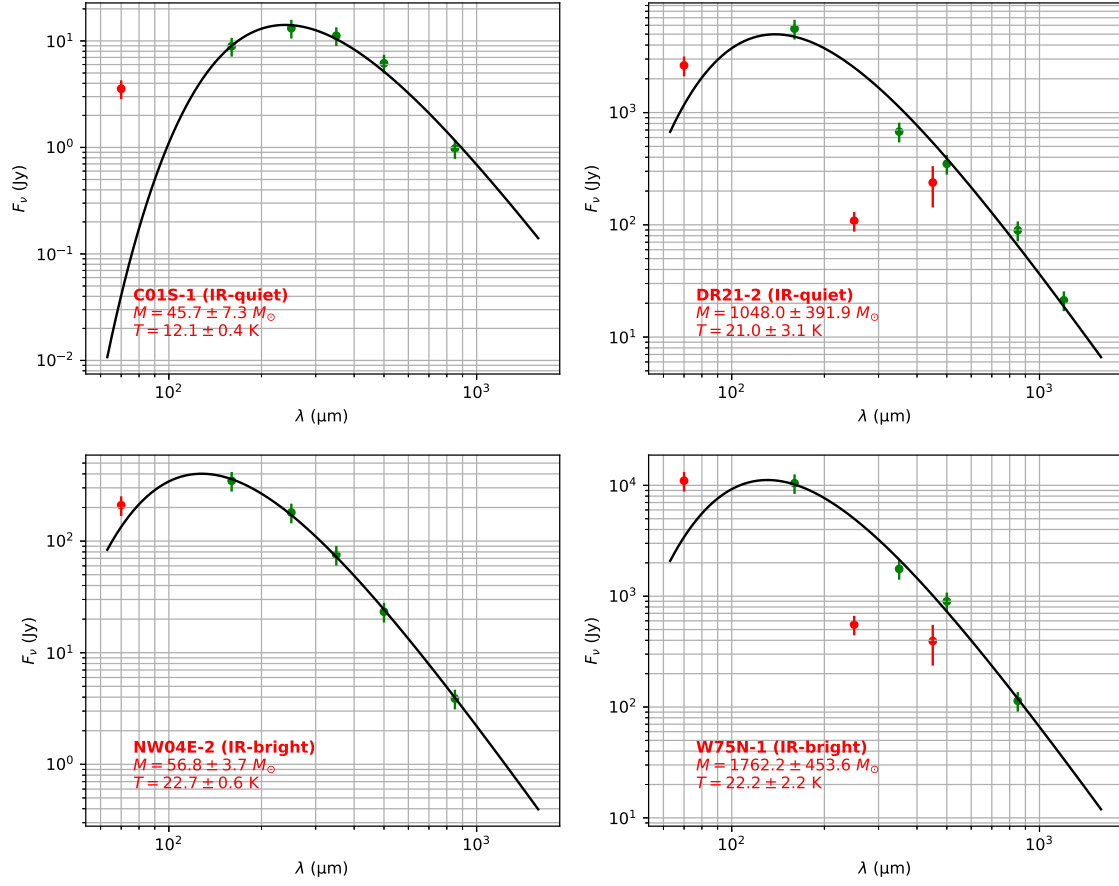


Figure C. SED fittings of four example MDCs (two IR-bright and two IR-quiet). Data in green were used for the fitting while data in red were not due to their large deviations from the model curves (see Sect. 3.2.2).

Table C. Fluxes of the MDCs in Cygnus X Obtained by *getsources* (in Jy)

Name	$F_V(70 \mu\text{m})$	$F_V(160 \mu\text{m})$	$F_V(250 \mu\text{m})$	$F_V(350 \mu\text{m})$	$F_V(450 \mu\text{m})$	$F_V(500 \mu\text{m})$	$F_V(850 \mu\text{m})$	$F_V(1.2 \text{ mm})$
C01S-1	(3.55 ± 0.03)	8.91 ± 0.28	13.2 ± 0.63	11.2 ± 0.64	...	6.17 ± 0.78	0.975 ± 0.04	...
C03-1	(267 ± 1.15)	420 ± 0.83	560 ± 0.32	218 ± 0.23	...	63.6 ± 0.49	5.73 ± 0.05	...
C03S-1	(68.7 ± 0.07)	120 ± 0.24	88.6 ± 0.25	48.9 ± 0.32	...	18.7 ± 0.31	1.20 ± 0.04	...
C05-1	(6.80 ± 0.91)	57.6 ± 4.10	59.8 ± 2.87	33.1 ± 0.43	(5.90 ± 0.13)	16.7 ± 0.89	3.00 ± 0.11	...
C05-2	(14.2 ± 0.25)	19.1 ± 1.86	22.2 ± 2.18	15.1 ± 0.83	(0.962 ± 0.06)	11.9 ± 0.99	0.763 ± 0.07	...
C05-3	...	14.9 ± 3.84	20.8 ± 3.59	15.2 ± 2.27	(2.69 ± 0.09)	9.64 ± 1.27	0.684 ± 0.14	...
C05-4	(2.13 ± 0.56)	9.76 ± 1.48	18.9 ± 1.17	14.6 ± 0.49	(0.910 ± 0.06)	7.39 ± 0.45	0.547 ± 0.04	...
C08-1	6.06 ± 0.67	11.1 ± 0.79	...	5.80 ± 0.62
C08-2	(182 ± 2.49)	140 ± 7.13	65.6 ± 4.71	61.4 ± 2.17	...	33.5 ± 0.91	1.23 ± 0.16	...
C08-3	(214 ± 2.00)	170 ± 5.66	63.6 ± 3.90	54.7 ± 1.91	...	28.4 ± 1.30	1.43 ± 0.13	...
C09-1	(464 ± 0.68)	170 ± 0.51	290 ± 0.75	122 ± 0.62	(11.7 ± 0.24)	33.4 ± 0.51	3.59 ± 0.06	...
C09-2	...	3.00 ± 0.63	5.30 ± 0.84	6.38 ± 0.69	...	4.64 ± 0.59	0.523 ± 0.04	...
DR15-1	(5.87 ± 0.17)	10.6 ± 0.20	27.2 ± 0.96	20.0 ± 1.77	(2.69 ± 0.40)	15.2 ± 1.19	4.84 ± 0.08	0.570 ± 0.02
DR15-2	(53.9 ± 0.19)	114 ± 2.24	105 ± 2.70	(334 ± 0.94)	(10.3 ± 0.35)	24.8 ± 1.16	4.50 ± 0.15	1.27 ± 0.03
DR15-3	(0.445 ± 0.23)	21.1 ± 3.38	24.8 ± 2.50	(6.09 ± 1.74)	(3.74 ± 0.35)	11.3 ± 1.19	1.68 ± 0.14	0.410 ± 0.03
DR15-4	(1083 ± 43.5)	519 ± 18.3	160 ± 8.56	102 ± 2.92	(9.34 ± 0.29)	27.3 ± 1.78	4.41 ± 0.15	1.03 ± 0.05
DR15-5	(3.22 ± 0.28)	9.58 ± 0.20	10.7 ± 0.77	9.28 ± 1.25	(3.41 ± 0.30)	6.54 ± 0.89	1.65 ± 0.07	0.207 ± 0.02
DR15-6	(14.0 ± 1.53)	42.3 ± 3.68	29.8 ± 2.39	13.4 ± 1.01	1.56 ± 0.12	0.364 ± 0.03
DR15-7	2.03 ± 2.44	0.921 ± 0.11	0.166 ± 0.02
DR15E1-1	(31.8 ± 0.41)	248 ± 1.04	441 ± 0.78	217 ± 0.67	(14.0 ± 0.30)	86.6 ± 0.66	17.3 ± 0.03	...
DR15E1-2	(1.42 ± 0.22)	10.8 ± 0.81	17.1 ± 0.98	18.6 ± 0.98	...	11.4 ± 0.51	1.23 ± 0.03	...
DR15E1-3	...	10.1 ± 0.86	14.2 ± 1.06	13.5 ± 1.03	...	9.10 ± 0.51	1.61 ± 0.03	...
DR15E2-1	(165 ± 0.23)	331 ± 1.03	(124 ± 1.48)	161 ± 0.55	...	37.8 ± 0.39	4.75 ± 0.05	...
DR15E2-2	(3.36 ± 0.22)	22.9 ± 1.81	27.8 ± 1.80	29.8 ± 0.97	...	19.6 ± 0.38	1.17 ± 0.08	...
DR15E2-3	(0.764 ± 0.04)	2.67 ± 0.16	8.05 ± 0.39	14.4 ± 0.44	...	3.51 ± 0.45	0.661 ± 0.04	...
DR15E2-4	(178 ± 0.43)	418 ± 0.46	201 ± 0.52	77.5 ± 0.55	...	23.6 ± 0.52	3.53 ± 0.03	...
DR21-1	(7666 ± 28.7)	5533 ± 27.7	...	1396 ± 3.70	(264 ± 1.64)	617 ± 1.83	70.3 ± 0.68	22.6 ± 0.14
DR21-2	(2635 ± 7.46)	5595 ± 6.61	(109 ± 5.33)	677 ± 3.82	(238 ± 1.60)	350 ± 2.16	89.3 ± 0.31	21.3 ± 0.07
DR21-3	(364 ± 13.9)	1831 ± 26.1	553 ± 18.1	409 ± 3.61	107 ± 1.80	167 ± 1.99	16.0 ± 0.67	5.52 ± 0.12
DR21-4	(224 ± 1.27)	527 ± 6.61	296 ± 6.39	(371 ± 3.52)	(31.0 ± 0.58)	48.2 ± 2.32	10.1 ± 0.50	2.29 ± 0.09
DR21-5	(220 ± 12.6)	290 ± 35.0	144 ± 22.7	71.9 ± 4.68	42.1 ± 2.32	25.2 ± 1.70	10.7 ± 0.99	1.58 ± 0.19
DR21-6	116 ± 20.9	42.9 ± 3.21	34.6 ± 0.64	...	6.37 ± 0.80	1.14 ± 0.15
DR21-7	(54.2 ± 0.90)	203 ± 6.96	121 ± 6.68	72.3 ± 3.73	(14.8 ± 0.58)	28.0 ± 2.43	6.87 ± 0.41	1.28 ± 0.08
DR21-8	...	481 ± 9.27	151 ± 12.2	(498 ± 3.51)	(18.5 ± 1.68)	44.3 ± 2.35	12.2 ± 0.59	1.13 ± 0.10
DR21-9	(38.7 ± 0.23)	79.9 ± 0.77	59.9 ± 1.30	34.0 ± 1.54	18.8 ± 0.10	10.5 ± 1.60	6.94 ± 0.05	1.01 ± 0.02
DR21-10	...	4.91 ± 0.38	10.8 ± 1.13	12.3 ± 1.12	(3.73 ± 0.13)	5.82 ± 1.21	3.04 ± 0.05	0.377 ± 0.02
DR21-11	41.4 ± 6.71	41.7 ± 2.36	21.4 ± 0.37	(4.15 ± 1.50)	5.87 ± 0.19	0.416 ± 0.11
DR21-12	46.3 ± 5.13	20.6 ± 3.27	13.7 ± 0.56	10.7 ± 2.28	2.77 ± 0.27	0.945 ± 0.09
DR21-13	(42.1 ± 6.39)	112 ± 11.5	473 ± 15.3	278 ± 3.80	103 ± 1.64	109 ± 2.25	1.48 ± 0.30	0.264 ± 0.07
DR21-14	26.8 ± 5.04	...	10.9 ± 0.59	...	2.03 ± 0.23	...
DR21-15	...	30.8 ± 2.44	30.0 ± 3.98	...	9.12 ± 0.30	...	2.37 ± 0.18	0.463 ± 0.05
DR21-16	...	70.1 ± 10.4	25.2 ± 11.8	56.1 ± 2.24	9.07 ± 0.51	...	5.00 ± 0.56	0.320 ± 0.06
DR21-17	(72.0 ± 3.07)	240 ± 23.3	76.7 ± 24.1	45.3 ± 3.56	24.3 ± 0.90	...	3.49 ± 0.64	...
DR21-18	5.51 ± 0.22	2.58 ± 1.23	2.27 ± 0.16	...

Table C continued

Table C (continued)

Name	$F_V(70 \mu\text{m})$	$F_V(160 \mu\text{m})$	$F_V(250 \mu\text{m})$	$F_V(350 \mu\text{m})$	$F_V(450 \mu\text{m})$	$F_V(500 \mu\text{m})$	$F_V(850 \mu\text{m})$	$F_V(1.2 \text{ mm})$
DR21-19	...	56.0 ± 11.5	42.6 ± 7.31	17.3 ± 2.52	8.10 ± 0.79	...	2.35 ± 0.30	0.550 ± 0.08
DR21-20	...	28.2 ± 11.5	...	9.64 ± 2.81	14.2 ± 1.06	...	1.29 ± 0.51	(0.054 ± 0.09)
DR21-21	...	47.9 ± 7.14	42.4 ± 7.47	(0.929 ± 3.64)	7.46 ± 0.89	(1.39 ± 2.50)	2.06 ± 0.45	...
DR21-22	(116 ± 1.09)	91.3 ± 4.33	56.6 ± 3.83	14.6 ± 2.69	10.5 ± 0.24	...	1.90 ± 0.15	0.838 ± 0.05
DR21-23	(487 ± 2.71)	758 ± 6.78	382 ± 8.38	(24.0 ± 3.30)	(8.60 ± 0.32)	40.0 ± 2.24	3.71 ± 0.40	0.921 ± 0.06
N03-1	(70.8 ± 1.56)	329 ± 3.11	366 ± 2.23	132 ± 1.88	65.2 ± 0.45	57.4 ± 1.53	30.4 ± 0.07	5.43 ± 0.03
N03-2	12.2 ± 1.07	1.38 ± 0.15	0.490 ± 0.04
N05-1	(1088 ± 3.45)	1017 ± 4.60	456 ± 3.51	430 ± 2.03	(28.7 ± 0.24)	150 ± 1.12	11.9 ± 0.09	...
N05-2	(40.3 ± 0.87)	4.38 ± 0.91	40.9 ± 0.96	70.4 ± 0.61	(3.35 ± 0.13)	12.5 ± 0.36	0.906 ± 0.08	...
N05-3	(591 ± 2.19)	594 ± 4.03	452 ± 2.86	179 ± 2.20	(14.2 ± 0.19)	58.1 ± 1.19	8.34 ± 0.07	...
N05-4	...	21.7 ± 3.62	18.1 ± 2.92	15.0 ± 2.02	(3.55 ± 0.17)	9.05 ± 1.12	1.71 ± 0.07	...
N05-5	(13.5 ± 0.23)	23.0 ± 1.46	17.6 ± 1.03	13.5 ± 0.98	(2.04 ± 0.17)	7.41 ± 1.04	1.56 ± 0.03	...
N05-6	(3.18 ± 1.81)	38.3 ± 1.08	32.7 ± 0.64	23.9 ± 0.57	(3.18 ± 0.16)	5.93 ± 0.38	1.88 ± 0.06	...
N07-1	...	13.4 ± 1.71	20.1 ± 2.23	21.0 ± 1.60	...	19.2 ± 1.23	1.97 ± 0.16	0.368 ± 0.03
N07-2	(0.827 ± 0.05)	3.33 ± 0.51	5.48 ± 0.73	7.48 ± 0.76	...	6.15 ± 0.66	0.822 ± 0.07	0.147 ± 0.02
N08-1	(17.3 ± 0.07)	52.7 ± 0.48	44.7 ± 1.17	30.6 ± 1.00	(6.78 ± 0.35)	18.1 ± 0.78	2.63 ± 0.06	...
N08-2	(0.487 ± 0.11)	2.57 ± 0.49	6.86 ± 0.66	6.40 ± 0.53	...	4.25 ± 0.37	0.489 ± 0.05	...
N12-1	(146 ± 0.18)	358 ± 1.26	586 ± 0.88	272 ± 0.73	(57.7 ± 0.21)	119 ± 1.10	11.9 ± 0.17	4.15 ± 0.02
N12-2	(5.99 ± 0.12)	34.2 ± 1.37	44.5 ± 0.47	29.1 ± 0.48	(6.01 ± 0.22)	14.4 ± 0.39	2.24 ± 0.12	0.458 ± 0.03
N12-3	(145 ± 0.42)	150 ± 1.92	73.6 ± 2.02	31.9 ± 1.62	(8.86 ± 0.16)	14.2 ± 1.13	4.04 ± 0.06	0.732 ± 0.02
N12-4	...	4.17 ± 1.58	7.95 ± 2.46	7.99 ± 1.91	4.67 ± 0.24	...	1.38 ± 0.08	0.284 ± 0.02
N12-5	(42.4 ± 0.21)	112 ± 0.87	71.5 ± 1.41	21.9 ± 1.26	(6.16 ± 0.15)	11.5 ± 1.17	2.33 ± 0.10	0.713 ± 0.02
N12-6	...	19.9 ± 1.06	17.9 ± 1.20	10.1 ± 1.25	(4.27 ± 0.21)	7.55 ± 0.94	1.57 ± 0.09	0.320 ± 0.02
N12-7	...	10.2 ± 1.96	(0.677 ± 0.63)	11.6 ± 0.46	(3.05 ± 0.24)	7.13 ± 0.74	1.26 ± 0.21	0.201 ± 0.04
N26-1	(12.8 ± 0.50)	34.0 ± 2.77	30.1 ± 2.65	18.2 ± 2.13	(7.12 ± 0.17)	10.5 ± 1.50	2.24 ± 0.19	0.392 ± 0.02
N58-1	29.3 ± 2.21	3.94 ± 0.14	0.951 ± 0.05
N58-2	...	124 ± 12.2	74.6 ± 7.54	39.8 ± 3.42	...	18.9 ± 1.75	2.26 ± 0.21	0.981 ± 0.04
N58-3	(95.0 ± 5.72)	118 ± 9.12	59.2 ± 6.80	30.6 ± 4.59	...	13.7 ± 1.88	3.08 ± 0.13	0.871 ± 0.05
N58-4	(0.635 ± 0.43)	3.96 ± 1.22	10.1 ± 1.51	7.22 ± 1.26	...	4.31 ± 0.61	0.812 ± 0.13	0.200 ± 0.03
N63-1	(67.4 ± 0.09)	211 ± 0.85	170 ± 1.45	93.2 ± 1.44	(29.5 ± 0.26)	36.1 ± 1.21	14.6 ± 0.05	3.10 ± 0.01
N63-2	...	86.5 ± 3.35	121 ± 1.59	104 ± 0.85	(9.70 ± 0.66)	24.9 ± 1.48	3.05 ± 0.12	0.519 ± 0.03
N63-3	(1.47 ± 0.14)	9.51 ± 0.53	26.6 ± 0.56	11.1 ± 0.64	...	8.43 ± 0.51	1.04 ± 0.10	0.220 ± 0.02
N68-1	(23.5 ± 0.50)	101 ± 1.58	121 ± 1.10	45.0 ± 1.00	(15.8 ± 0.42)	23.2 ± 0.93	8.90 ± 0.06	1.68 ± 0.01
N68-2	(51.1 ± 0.34)	158 ± 1.29	148 ± 1.18	58.8 ± 1.09	(17.0 ± 0.51)	21.6 ± 0.87	7.22 ± 0.13	0.991 ± 0.03
N68-3	20.2 ± 2.61	18.1 ± 1.24	(6.41 ± 0.46)	8.83 ± 1.67	2.24 ± 0.15	0.548 ± 0.03
N68-4	18.0 ± 4.13	26.5 ± 3.96	(0.498 ± 0.58)	12.6 ± 2.50	2.33 ± 0.23	0.365 ± 0.06
N68-5	...	11.5 ± 1.45	17.9 ± 1.27	19.5 ± 1.14	(6.38 ± 0.34)	10.4 ± 0.91	1.72 ± 0.11	0.356 ± 0.02
N68-6	26.4 ± 5.98	...	11.4 ± 2.62	2.10 ± 0.28	0.674 ± 0.09
N68-7	8.56 ± 1.56	9.30 ± 1.49	(0.379 ± 0.37)	9.01 ± 1.58	1.12 ± 0.08	0.218 ± 0.02
N68-8	16.1 ± 2.30	11.8 ± 1.37	(4.54 ± 0.45)	7.63 ± 1.68	1.35 ± 0.08	0.261 ± 0.02
NW01-1	(1039 ± 5.02)	1386 ± 2.54	379 ± 1.79	108 ± 1.38	(8.03 ± 0.38)	65.1 ± 0.91	7.92 ± 0.05	...
NW04-1	(198 ± 2.27)	552 ± 0.49	377 ± 0.49	223 ± 0.48	(5.16 ± 0.38)	78.8 ± 0.40	15.1 ± 0.03	...
NW04-2	...	1.12 ± 1.13	...	5.38 ± 0.73	...	3.04 ± 0.55
NW04-3	(8.85 ± 0.06)	33.0 ± 0.25	35.3 ± 0.29	22.5 ± 0.35	...	7.79 ± 0.27	(0.551 ± 0.04)	...
NW04-4	2.54 ± 0.76	3.26 ± 0.89	...	1.86 ± 0.55
NW04-5	(7.26 ± 0.11)	24.1 ± 0.65	18.3 ± 0.72	13.3 ± 0.75	(3.37 ± 0.35)	7.31 ± 0.56	1.20 ± 0.04	...
NW04E-1	(10.3 ± 0.76)	61.5 ± 2.25	(45.2 ± 1.60)	109 ± 1.46	...	52.7 ± 1.12	(1.58 ± 0.07)	...

Table C continued

Table C (continued)

Name	$F_V(70 \mu\text{m})$	$F_V(160 \mu\text{m})$	$F_V(250 \mu\text{m})$	$F_V(350 \mu\text{m})$	$F_V(450 \mu\text{m})$	$F_V(500 \mu\text{m})$	$F_V(850 \mu\text{m})$	$F_V(1.2 \text{ mm})$
NW04E-2	(210 ± 0.41)	347 ± 1.38	180 ± 1.14	75.4 ± 0.90	...	23.3 ± 0.79	3.88 ± 0.04	...
NW12-1	(290 ± 0.12)	442 ± 0.34	268 ± 0.60	114 ± 0.96	...	39.5 ± 0.90	9.25 ± 0.03	1.92 ± 0.02
S01-1	...	4.71 ± 0.89	12.9 ± 1.70	16.2 ± 1.48	...	12.9 ± 0.64	...	0.450 ± 0.03
S01-2	(238 ± 1.36)	65.2 ± 2.62	81.5 ± 1.28	28.4 ± 0.85	...	17.3 ± 0.87
S01-3	(96.4 ± 0.16)	139 ± 0.62	97.3 ± 1.34	48.3 ± 1.34	(3.30 ± 0.31)	24.4 ± 0.62	...	0.854 ± 0.02
S01-4	(5.99 ± 1.31)	31.1 ± 3.97	30.9 ± 2.79	23.2 ± 2.51	...	12.8 ± 1.05	...	0.488 ± 0.04
S01-5	...	7.23 ± 0.96	11.2 ± 1.69	11.0 ± 1.82	(1.90 ± 0.29)	6.75 ± 1.30	...	0.224 ± 0.02
S01-6	(23.6 ± 0.04)	32.0 ± 0.47	23.9 ± 1.46	13.7 ± 0.90	(1.38 ± 0.24)	9.22 ± 0.74
S01S-1	(4.60 ± 0.12)	33.2 ± 0.17	34.2 ± 0.12	29.4 ± 0.09	(0.297 ± 0.03)	13.6 ± 0.06
S01S-2	(27.9 ± 0.10)	169 ± 0.11	110 ± 0.07	55.2 ± 0.05	(0.500 ± 0.02)	18.3 ± 0.04
S01S-3	(41.8 ± 0.54)	111 ± 0.82	93.1 ± 0.71	(91.8 ± 0.27)	...	13.9 ± 0.49
S01S-4	(0.454 ± 0.11)	4.38 ± 0.82	6.98 ± 0.59	6.28 ± 0.48	...	3.72 ± 0.34
S07-1	(1466 ± 0.34)	1882 ± 1.59	1084 ± 2.59	629 ± 1.70	...	240 ± 1.46	14.8 ± 0.09	...
S11-1	...	60.1 ± 3.42	38.9 ± 1.69	49.4 ± 1.42	...	11.4 ± 1.12	5.49 ± 0.05	0.519 ± 0.02
S11-2	(3.56 ± 0.40)	11.7 ± 1.17	15.2 ± 1.30	25.6 ± 0.98	...	10.8 ± 0.79	1.65 ± 0.06	0.403 ± 0.02
S11-3	...	(0.793 ± 0.92)	7.74 ± 1.11	9.39 ± 0.91	...	6.04 ± 0.78	0.588 ± 0.06	...
S13-1	(46.7 ± 0.78)	98.4 ± 2.67	60.8 ± 1.48	36.0 ± 1.10	...	15.3 ± 0.84	2.82 ± 0.11	0.734 ± 0.02
S13-2	(1.48 ± 0.40)	30.8 ± 2.48	26.0 ± 1.53	17.6 ± 1.04	...	9.76 ± 0.86	1.88 ± 0.09	0.558 ± 0.02
S13S-1	...	3.84 ± 0.45	8.87 ± 0.76	6.62 ± 0.70
S13S-2	(40.1 ± 0.04)	59.5 ± 0.17	69.8 ± 0.27	21.7 ± 0.37	...	10.1 ± 0.36
S13S-3	(3.95 ± 0.03)	6.48 ± 0.10	7.83 ± 0.21	6.82 ± 0.29	...	4.92 ± 0.18
S13S-4	(4.03 ± 0.04)	8.37 ± 0.09	(0.307 ± 0.24)	8.67 ± 0.36	...	4.67 ± 0.37
S29-1	(0.527 ± 0.13)	8.94 ± 1.72	16.5 ± 2.51	22.9 ± 2.53	(2.95 ± 0.26)	15.6 ± 1.48	1.60 ± 0.12	...
S30-1	(494 ± 0.72)	512 ± 0.60	534 ± 0.50	355 ± 0.39	(15.2 ± 0.48)	174 ± 0.71	(6.55 ± 0.08)	(1.59 ± 0.02)
S30-2	(1.78 ± 0.43)	19.2 ± 1.57	1.76 ± 0.12	0.299 ± 0.02
S30-3	...	22.2 ± 1.90	26.8 ± 0.57	(2.89 ± 0.41)	3.45 ± 0.36	3.07 ± 0.52	2.09 ± 0.12	0.625 ± 0.02
S30S-1	(5.21 ± 0.06)	22.5 ± 0.25	26.9 ± 0.33	25.7 ± 0.35	(1.36 ± 0.11)	8.81 ± 0.29	1.42 ± 0.02	...
S32-1	(32.2 ± 0.78)	115 ± 1.90	80.0 ± 2.46	47.2 ± 1.53	(12.0 ± 0.15)	24.4 ± 1.28	5.50 ± 0.06	0.904 ± 0.03
S32-2	(2.85 ± 0.35)	6.08 ± 0.84	(3.71 ± 0.55)	8.71 ± 1.33	...	6.52 ± 1.60
S32-3	(12.8 ± 0.32)	48.1 ± 1.66	42.2 ± 1.34	24.4 ± 0.90	(3.62 ± 0.13)	11.9 ± 0.57	2.21 ± 0.06	0.421 ± 0.02
S32-4	(4.28 ± 0.54)	13.9 ± 2.31	10.7 ± 0.93	11.9 ± 0.78	1.16 ± 0.05	...
S43-1	6.61 ± 1.97	...	3.29 ± 0.98	1.06 ± 0.15	0.554 ± 0.04
S43-2	...	41.5 ± 0.75	46.1 ± 1.50	28.3 ± 1.49	(6.15 ± 0.22)	12.8 ± 1.12	3.55 ± 0.08	0.686 ± 0.02
S43-3	...	15.6 ± 0.87	31.7 ± 1.46	30.6 ± 1.49	(2.69 ± 0.22)	19.1 ± 1.01	1.90 ± 0.07	0.348 ± 0.02
S43-4	8.82 ± 1.56	8.50 ± 1.37	...	(0.714 ± 1.02)	0.999 ± 0.09	...
S106-1	...	37.3 ± 10.3	40.5 ± 7.51	34.6 ± 4.44	(6.09 ± 0.42)	25.0 ± 3.33	1.74 ± 0.19	...
S106-2	(3180 ± 8.97)	2124 ± 13.9	377 ± 11.3	106 ± 8.32	(10.5 ± 0.64)	93.5 ± 3.15	9.22 ± 0.20	...
S106N-1	(21.9 ± 0.02)	79.8 ± 0.09	66.0 ± 0.19	44.3 ± 0.19	...	23.4 ± 0.18	2.08 ± 0.04	...
S106W1-1	(52.3 ± 0.09)	79.5 ± 0.74	78.2 ± 0.99	32.3 ± 1.12	...	18.8 ± 0.55	2.37 ± 0.06	...
S106W1-2	...	15.2 ± 2.00	16.5 ± 3.17	(0.529 ± 2.34)	...	7.17 ± 0.90	1.75 ± 0.10	...
S106W1-3	(585 ± 1.81)	420 ± 4.62	165 ± 3.67	78.1 ± 2.45	...	25.8 ± 0.84	3.79 ± 0.08	...
S106W1-4	(1.83 ± 0.74)	56.0 ± 5.59	47.9 ± 3.63	30.5 ± 2.30	...	10.2 ± 0.44	1.90 ± 0.11	...
S106W1-5	67.4 ± 8.23	36.2 ± 4.35	...	(2.33 ± 0.65)	2.17 ± 0.20	...
S106W1-6	...	11.4 ± 0.91	11.4 ± 0.99	8.48 ± 0.91	...	6.37 ± 1.29	(0.108 ± 0.08)	...
S106W1-7	(39.9 ± 0.92)	67.5 ± 1.96	41.1 ± 2.26	20.1 ± 2.41	...	12.9 ± 0.82	1.60 ± 0.05	...
S106W2-1	(3474 ± 6.14)	1872 ± 14.3	1116 ± 4.01	601 ± 3.19	...	234 ± 2.11
S106W2-2	(206 ± 8.40)	458 ± 7.40	448 ± 4.38	198 ± 2.71	...	133 ± 1.77

Table C continued

Table C (continued)

Name	$F_V(70 \mu\text{m})$	$F_V(160 \mu\text{m})$	$F_V(250 \mu\text{m})$	$F_V(350 \mu\text{m})$	$F_V(450 \mu\text{m})$	$F_V(500 \mu\text{m})$	$F_V(850 \mu\text{m})$	$F_V(1.2 \text{ mm})$
S106W2-3	(1513 ± 7.58)	1115 ± 12.1	358 ± 4.16	256 ± 2.59	...	61.9 ± 1.74
S106W2-4	(102 ± 4.03)	162 ± 9.61	119 ± 4.61	55.4 ± 5.11	...	26.5 ± 2.42
S106W2-5	(1.81 ± 0.20)	19.0 ± 1.76	21.6 ± 2.07	18.4 ± 2.43	...	11.2 ± 2.33
S106W2-6	...	10.6 ± 5.19	11.3 ± 4.60	17.9 ± 0.98	...	6.00 ± 0.95
S106W2-7	(289 ± 4.25)	230 ± 6.51	108 ± 4.81	38.7 ± 5.21	...	19.3 ± 2.54
S106W2-8	(3.51 ± 0.13)	11.8 ± 1.14	12.0 ± 1.44	10.1 ± 1.69	...	5.59 ± 1.87
S106W2-9	...	13.0 ± 0.94	18.3 ± 1.46	12.4 ± 1.76	...	4.86 ± 1.24
W75N-1	(11010 ± 0.34)	10470 ± 2.19	(554 ± 7.71)	1762 ± 1.63	(394 ± 0.14)	898 ± 1.09	114 ± 0.08	...
W75N-2	...	9.38 ± 1.65	12.3 ± 2.13	20.4 ± 1.68	(4.67 ± 0.25)	14.9 ± 1.03	3.59 ± 0.07	...
W75N-3	(0.966 ± 0.24)	49.8 ± 2.52	52.7 ± 7.01	32.8 ± 1.36	(12.6 ± 0.35)	20.9 ± 1.06	4.36 ± 0.16	...
W75N-4	(10.2 ± 0.79)	27.9 ± 2.04	25.9 ± 2.68	20.6 ± 2.22	(4.11 ± 0.22)	13.2 ± 0.98	1.45 ± 0.08	...
W75N-5	(0.611 ± 0.16)	7.15 ± 1.00	12.3 ± 1.18	12.5 ± 0.60	(3.43 ± 0.13)	(1.32 ± 0.75)	0.902 ± 0.05	...
W75N-6	(16.7 ± 0.08)	29.6 ± 0.63	21.8 ± 1.73	14.9 ± 1.33	...	10.2 ± 0.81	1.17 ± 0.09	...

NOTE—Fluxes in brackets were not used for SED fitting since they deviate largely from the model or the wavelengths are at 70 μm (see Sect. 3.2.2). Ellipses mean the data are not available in the continuum images used for source extraction.

D. SOURCES ASSOCIATED WITH THE MDCS IN CYGNUS X

This appendix presents the mid-IR sources and signposts of HMSF that are associated with the MDCs. The positional tolerances were all set to 10''.

Table D1. Mid-infrared Sources Associated with the MDCs in Cygnus X

Name	Method ^a	$F_V(\text{Spitzer } 24\mu\text{m})$ (Jy)	Spitzer ID	$F_V(\text{MSX } 21\mu\text{m})$ (Jy)	MSX ID
C01S-1	catalog	0.046	J202925.88+403605.1
C03-1	catalog	2.446	J203029.40+411557.9
C03S-1	catalog	3.986	J203050.66+410227.6	2.295	G079.7358+00.9905
C05-1	catalog	0.084 0.088	J203223.76+410757.5 J203224.72+410803.4
C05-2	catalog	3.213	J203221.06+410754.5	2.691	G079.9766+00.8153
C05-4	catalog	0.033	J203223.21+410651.7
C08-2	catalog	6.649	G080.3656+00.4573
C08-3	catalog	11.089	G080.3597+00.4419
C09-1	catalog	18.475	G080.6344+00.6822
C09-2	catalog	0.021	J203449.97+413359.0
DR15-1	catalog	0.241	J203158.15+401836.1
DR15-2	catalog	4.962 1.545	J203222.10+402017.1 J203222.99+402021.4	4.441	G079.3398+00.3417

Table D1 continued

Table D1 (continued)

Name	Method ^a	F_V (<i>Spitzer</i> 24 μ m) (Jy)	<i>Spitzer</i> ID	F_V (<i>MSX</i> 21 μ m) (Jy)	<i>MSX</i> ID
		0.846	J203221.13+402025.6		
DR15-3	catalog	0.476	J203223.04+401922.7
DR15-5	catalog	0.159	J203137.00+401939.3
DR15-6	catalog	0.612 0.990	J203221.96+401937.7 J203220.60+401950.1
DR15E1-1	catalog	0.142	J203442.23+394505.8
DR15E1-2	catalog	0.262 0.042	J203323.60+394245.3 J203323.95+394256.7
DR15E1-3	catalog	0.009	J203328.73+394119.1
DR15E2-1	photometry	0.305
DR15E2-2	catalog	0.028	J203750.17+394952.0
DR15E2-3	catalog	0.124	J203627.76+394239.3
DR15E2-4	catalog	4.894	J203714.82+394855.5	9.669	G079.4822-00.7174
DR21-1	catalog	543.910	G081.6802+00.5405
DR21-2	catalog	6.777	G081.7220+00.5699
DR21-3	catalog	28.401	G081.7133+00.5589
DR21-4	catalog	26.502	G081.7522+00.5906
DR21-6	catalog	1.083	J203901.91+421837.4
DR21-7	photometry	0.363
DR21-8	catalog	0.073	J203859.53+422343.6
DR21-9	catalog	5.645	J203916.72+421609.3	3.677	G081.6632+00.4651
DR21-12	catalog	0.024	J203850.80+422716.4
DR21-14	catalog	0.007 0.021	J203901.80+422656.6 J203902.18+422644.4
DR21-16	catalog	0.226 0.102	J203901.44+421809.6 J203900.55+421821.0
DR21-17	photometry	0.539
DR21-20	catalog	1.083	J203901.91+421837.4
DR21-21	catalog	0.135	J203903.13+422627.7
DR21-22	catalog	1.359	J203907.31+421534.9	7.252	G081.6411+00.4812
DR21-23	photometry	20.148	...
N03-1	catalog	1.250 2.448 1.714	J203533.56+422015.1 J203534.75+422016.7 J203534.44+422006.8	3.737	G081.3039+01.0520
N05-1	catalog	99.331	G080.8645+00.4197
N05-3	catalog	19.714	G080.8624+00.3827
N05-4	catalog	0.091	J203712.23+413334.6
N05-5	catalog	0.668 1.442	J203724.92+413535.6 J203726.02+413540.9	2.334	G080.9171+00.3289

Table D1 continued

Table D1 (continued)

Name	Method ^a	$F_V(\text{Spitzer } 24\mu\text{m})$ (Jy)	Spitzer ID	$F_V(\text{MSX } 21\mu\text{m})$ (Jy)	MSX ID
N05-6	catalog	0.774	J203603.28+413939.6
N07-1	catalog	0.016	J203639.89+425110.6
N07-2	catalog	0.033	J203547.51+425254.6
N08-1	catalog	0.336	J203638.56+422907.3
		0.143	J203638.34+422915.7		
N08-2	catalog	0.188	J203619.91+423728.5
N12-1	photometry	1.096
N12-2	photometry	0.019
N12-3	catalog	3.225	J203717.67+421637.5	3.872	G081.4452+00.7635
N12-5	catalog	2.283	J203730.51+421359.1
N12-7	catalog	0.022	J203704.82+421150.7
		0.075	J203705.70+421203.0		
N26-1	catalog	0.837	J203821.33+421120.7
		0.909	J203820.96+421125.9		
		0.421	J203822.29+421135.4		
N58-2	catalog	1.011	J203931.50+412003.0	2.809	G080.9473-00.1419
		0.908	J203930.96+412002.8		
N58-3	catalog	3.332	G080.9500-00.1556
N58-4	photometry	0.031
N63-1	catalog	0.442	J204005.54+413212.8
		0.162	J204005.58+413221.3		
N63-3	catalog	0.068	J204033.51+413839.5
		0.090	J204034.91+413845.1		
N68-1	catalog	0.195	J204033.49+415900.6
N68-2	catalog	2.750	J204028.49+415712.0	-1.415	G081.5486+00.0945
		2.395	J204028.98+415707.9		
NW01-1	catalog	400.660	G078.4373+02.6584
NW04-1	catalog	85.851	G078.8699+02.7602
NW04-3	catalog	0.274	J201939.16+411102.5
NW04-5	photometry	0.159
NW04E-1	catalog	1.609	G079.1557+02.2197
NW04E-2	catalog	27.468	G079.1272+02.2782
NW12-1	catalog	15.582	G079.8855+02.5517
S01-1	catalog	0.067	J201648.81+392208.7
S01-2	catalog	12.621	G076.9283+02.0329
S01-3	catalog	6.554	J201659.13+392103.9	5.271	G076.8322+02.1876
S01-4	catalog	0.511	J201745.91+392040.1
S01-6	catalog	3.873	J201643.74+392320.5	3.085	G076.8356+02.2494
S01S-2	catalog	0.320	J201737.09+390334.4

Table D1 continued

Table D1 (continued)

Name	Method ^a	$F_V(\text{Spitzer } 24\mu\text{m})$ (Jy)	Spitzer ID	$F_V(\text{MSX } 21\mu\text{m})$ (Jy)	MSX ID
S01S-4	catalog	0.079	J201651.59+390011.7
S07-1	catalog	145.480	G077.4622+01.7600
S11-1	catalog	0.691	J202220.04+395823.0
S11-2	catalog	0.955	J202153.50+395936.7
S13-1	catalog	5.055	J202632.37+395720.8	4.843	G078.3762+01.0191
S13S-1	catalog	0.220	J202658.91+391023.6
S13S-2	catalog	8.738	G077.9280+00.8711
S13S-3	catalog	0.275	J202612.63+391641.9
S13S-4	catalog	0.112	J202547.75+392954.2
S29-1	catalog	0.316	J202957.68+401604.2
S30-2	catalog	0.219	J203114.63+400318.4
S30-3	catalog	2.073	J203112.91+400323.1
S30S-1	catalog	0.113	J203058.65+394229.0
		0.250	J203057.88+394220.8		
		0.245	J203058.04+394226.7		
S32-1	catalog	0.120	J203121.71+385716.6
S32-4	catalog	0.239	J203147.25+390048.2	2.641	G078.2049-00.3555
S43-2	catalog	0.105	J203240.77+384639.0
S106-2	catalog	1240.900	G076.3829-00.6210
S106N-1	catalog	0.169	J202614.94+380224.5
		0.410	J202614.09+380224.2		
S106W1-1	catalog	0.124	J202322.97+373548.8
		2.184	J202323.73+373535.2		
S106W1-2	catalog	0.036	J202406.91+373543.6
S106W1-3	catalog	54.009	G076.1877+00.0974
S106W1-4	catalog	0.197	J202358.42+373729.0
S106W1-6	catalog	0.150	J202328.46+373421.7
S106W1-7	catalog	3.288	J202402.83+373637.3	3.494	G076.1807+00.0619
S106W2-1	catalog	46.419	G075.7822+00.3421
S106W2-4	catalog	4.170	J202147.91+373017.3	4.043	G075.8404+00.3682
S106W2-5	catalog	0.291	J202155.09+372953.9
S106W2-7	catalog	6.830	G075.8428+00.3595
W75N-1	photometry	620.539	...
W75N-3	catalog	0.342	J203832.33+423945.1
		0.298	J203833.31+423938.7		
		0.004	J203834.09+423955.9		
W75N-4	catalog	0.698	J203810.05+423809.4
W75N-6	catalog	4.761	J203755.41+424046.7	3.702	G081.8375+00.9134

Table D1 continued

Table D1 (*continued*)

Name	Method ^a	$F_V(\text{Spitzer } 24\mu\text{m})$ (Jy)	Spitzer ID	$F_V(\text{MSX } 21\mu\text{m})$ (Jy)	MSX ID
------	---------------------	--	------------	--	--------

^aMethods used to extract fluxes. “Catalog” means that the fluxes were quoted from archival catalogs, and “photometry” means that the fluxes were obtained by manual photometry (see Sect. 3.3).

Table D2. Signposts of High-mass Star Formation of the MDCs in Cygnus X

MDC	VCLASS UCH II region ^a	$F_V(3 \text{ GHz})$ (Jy)	Class II methanol maser	Refs. ^b	$F_{V,\text{peak}}(6.7 \text{ GHz maser})$ (Jy)
C03S-1	G079.735+0.990	1	101.3
C09-1	J203500.21+413453.2	0.129
DR21-1	J203901.39+421937.7	4.917
DR21-2	G081.721+0.571	1	16.7
DR21-4	G081.752+0.590	1	63.7
DR21-7	G081.765+0.597	1	7.6
DR21-23	G081.744+0.590	1	32.4
N05-1	J203652.15+413623.7	0.034	J203652.60+413633.0	2	10.0
N05-3	G080.861+0.383	1	35.3
NW01-1	J201939.39+405634.7	0.071
S07-1	J202039.29+393750.9	0.026
S106-2	J202726.86+372246.9	3.090
S106W1-3	J202355.08+373809.5	0.398
S106W2-1	J202144.11+372639.5	0.030	G075.782+0.342	1	263.4
S106W2-3	75.76+0.34	3	39.0
W75N-1	G081.871+0.780	1	1865.5

^aVCLASS catalog was unavailable by the time of publication and the sources here were identified on the VCLASS images and named by their positions. The fluxes were obtained by manual radiometry.

^bReferences of the maser catalogs. 1. [Hu et al.\(2016\)](#) 2. [Malyshev & Sobolev\(2003\)](#) 3. [Pestalozzi et al.\(2005\)](#).

E. MAPS OF THE FIELDS AND MDCS IN CYGNUS X

This appendix shows the multi-wavelength maps of each field (Figure E1) and each MDC (Figure E2), as well as the column density and temperature maps derived by *getsources hirescoldens* command.

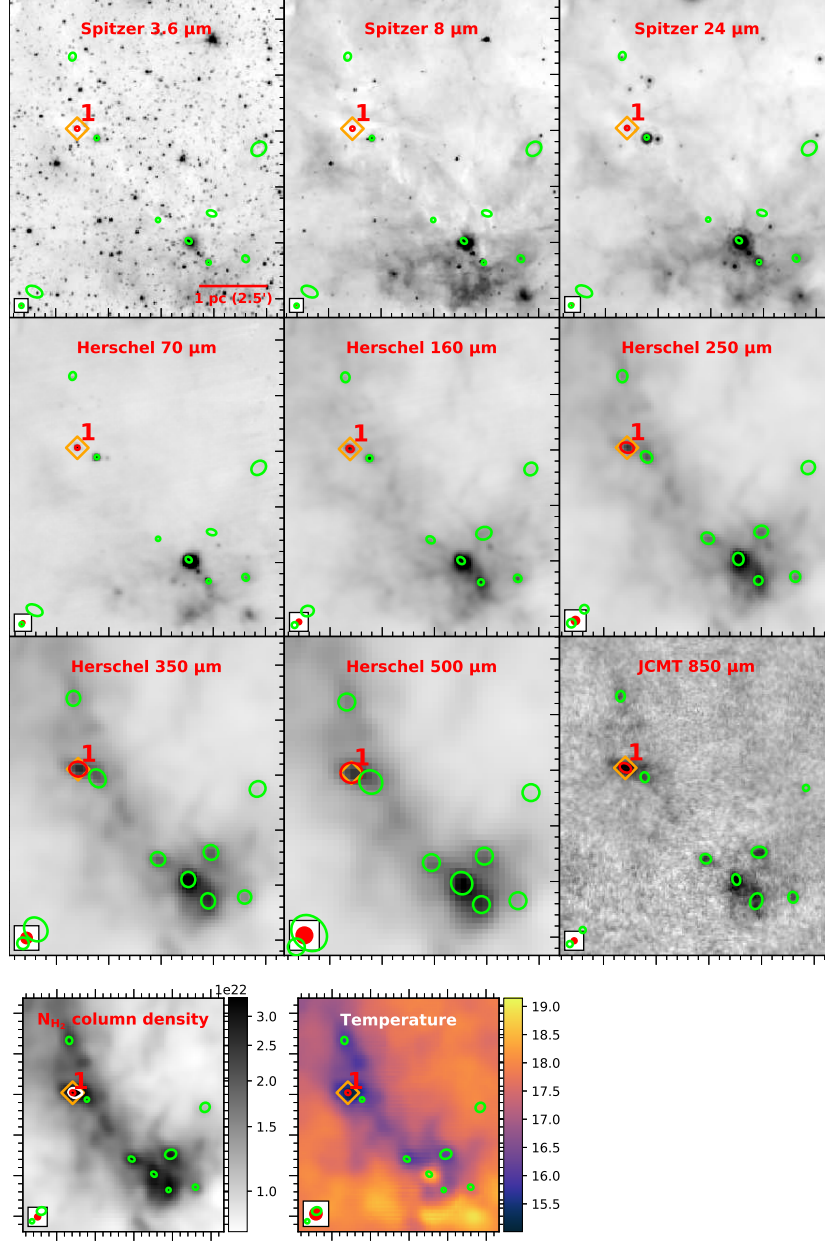


Figure E1. Continuum maps, column density maps, and temperature maps of the fields (here C01S) in Cygnus X. Continuum maps are in wavelengths of *Spitzer* (3.6, 8, and 24 μm), *Herschel* (70, 160, 250, 350, and 500 μm), JCMT (450 and 850 μm), and the IRAM 30 m telescope (1.2 mm). Panels will be omitted if the corresponding data are not available. Grayscale maps are logarithmically stretched for the *Spitzer* bands, and are linearly stretched for the other continuum bands. A single-level contour of $3.5 \times 10^{22} \text{cm}^{-2}$ is drawn as white solid lines in the column density panels. Green and red ellipses represent the FWHM sizes of cores and MDCs, respectively, obtained by *getsources* for the $\geq 70 \mu\text{m}$ bands, or the reference sizes at 70 μm for the $< 70 \mu\text{m}$ bands as well as the column density and temperature maps. Names of MDCs are shown. *Spitzer* 24 μm sources and *MSX* 21 μm sources are marked as orange and yellow diamonds, respectively. UCH II regions and class II methanol masers are marked as cyan and yellow triangles, respectively. **The complete figure set (39 images) is available in the online journal.**

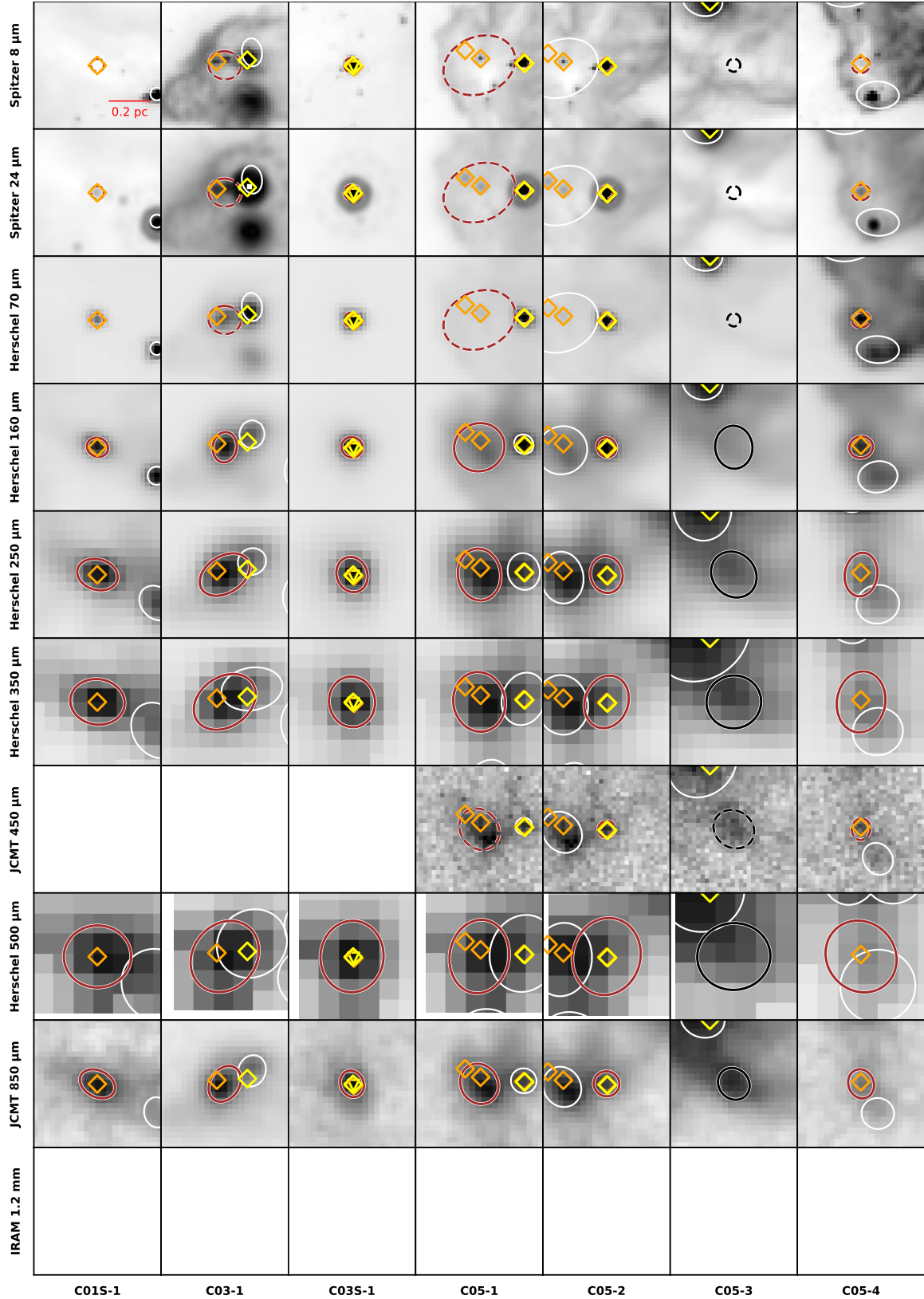


Figure E2. Images of the 151 MDCs in each band. Ellipses in the center of each panel are colored black, brown or red if the corresponding MDCs are starless, IR-quiet but not starless or IR-bright, respectively. Dashed ellipses mean that the corresponding fluxes were not used for SED fitting (see Sect. 3.2.2). Neighboring MDCs are represented as white ellipses. Other legends and figure settings are the same as in Figure E1. **The complete figure set (22 images) is available in the online journal.**

F. MAPS OF CYGNUS X

This appendix shows the multi-wavelength maps of the whole Cygnus X region, as well as the column density and temperature maps derived by *getsources hirescoldens* command.

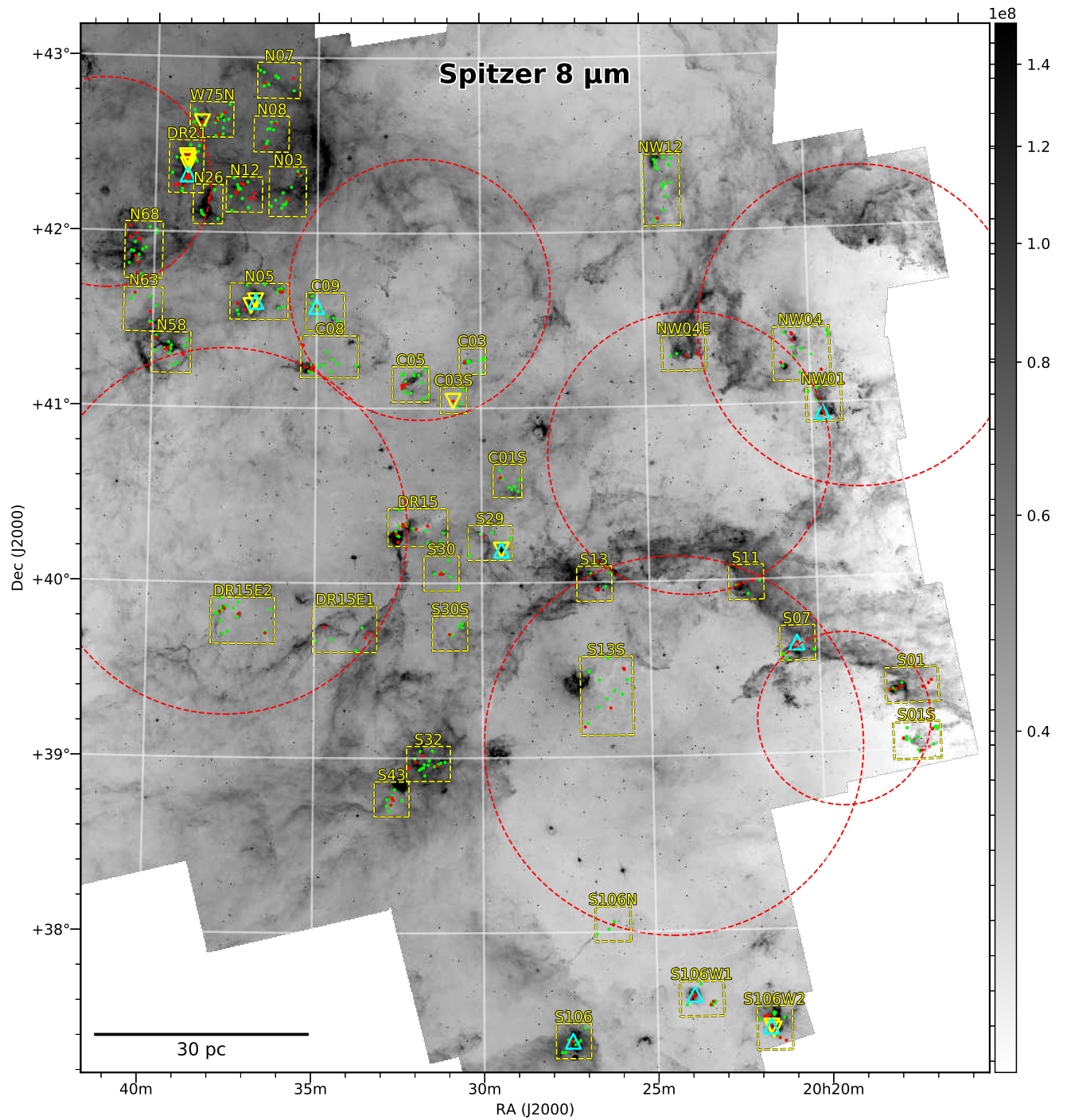


Figure F1. *Spitzer* 8 μm map (Jy sr^{-1}) with the same legends as in Figure 1. The continuum data are from The *Spitzer* Legacy Survey of the Cygnus-X Region.

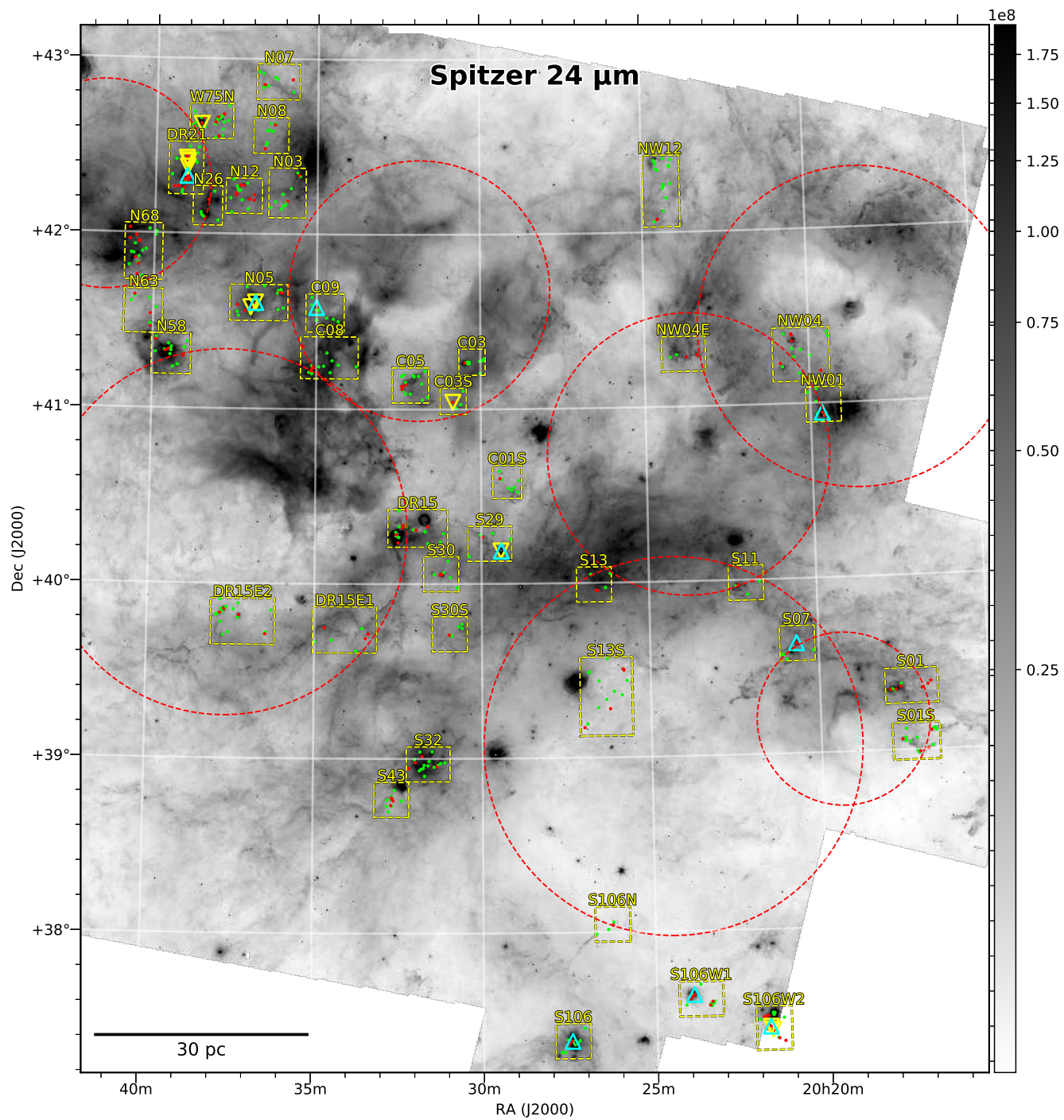


Figure F2. *Spitzer* 24 μm map (Jy sr^{-1}) with the same legends as in Figure 1. The continuum data are from The *Spitzer* Legacy Survey of the Cygnus-X Region.

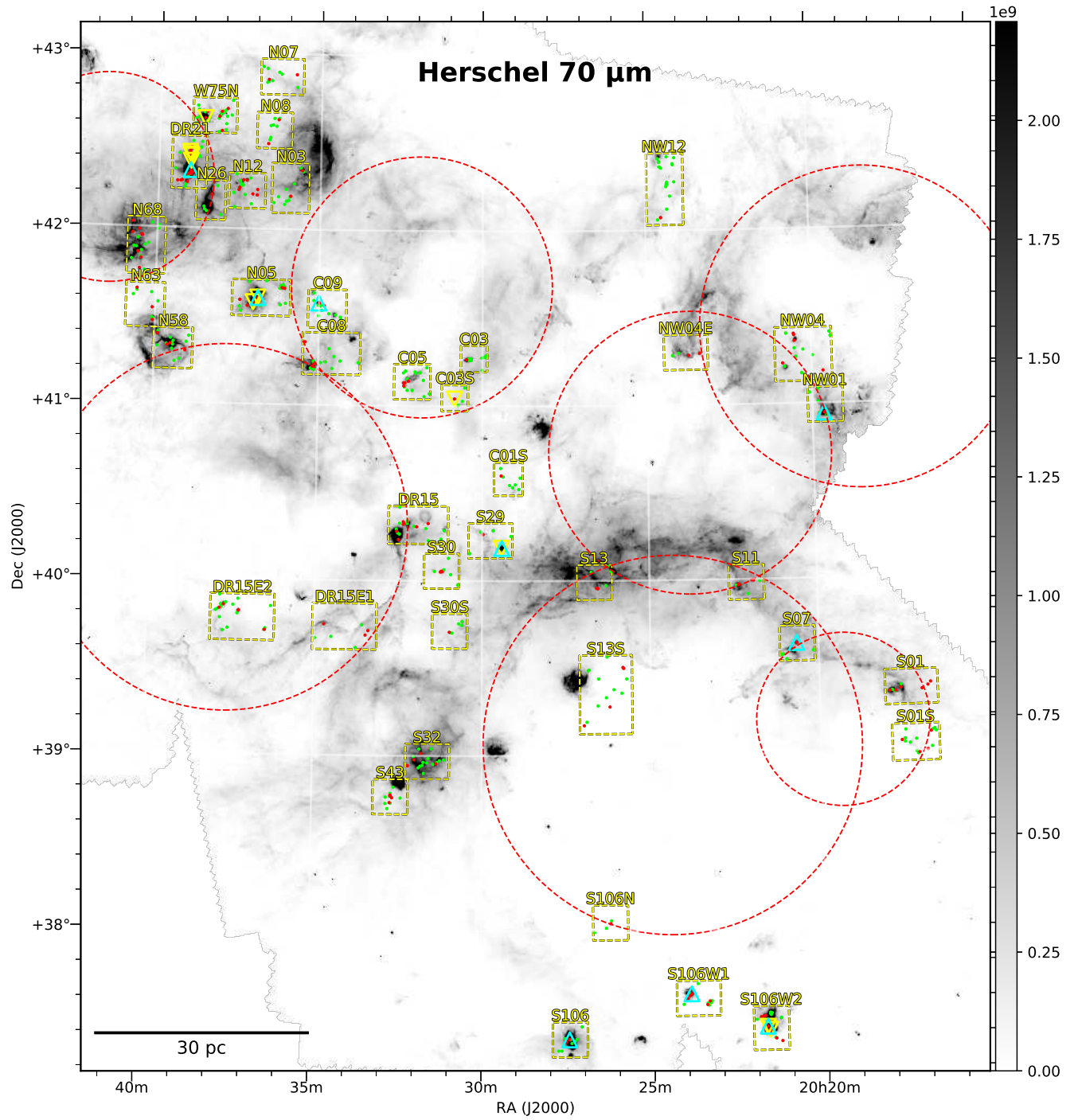


Figure F3. *Herschel* 70 μm map (Jy sr^{-1}) with the same legends as in Figure 1. This map was created using the images from the *Herschel* Science Archive.

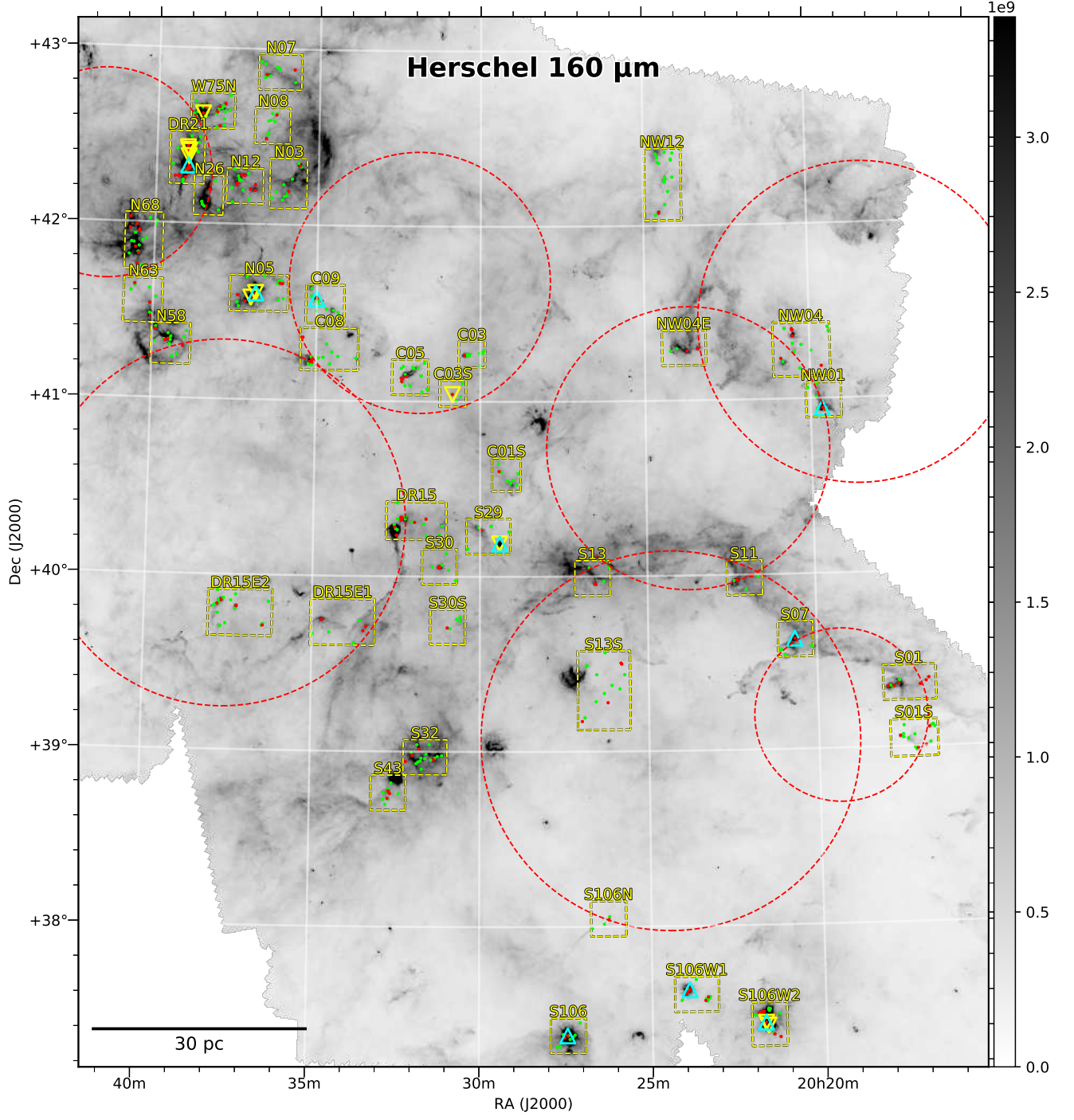


Figure F4. *Herschel* 160 μm map (Jy sr^{-1}) with the same legends as in Figure 1. This map was created using the images from the *Herschel* Science Archive.

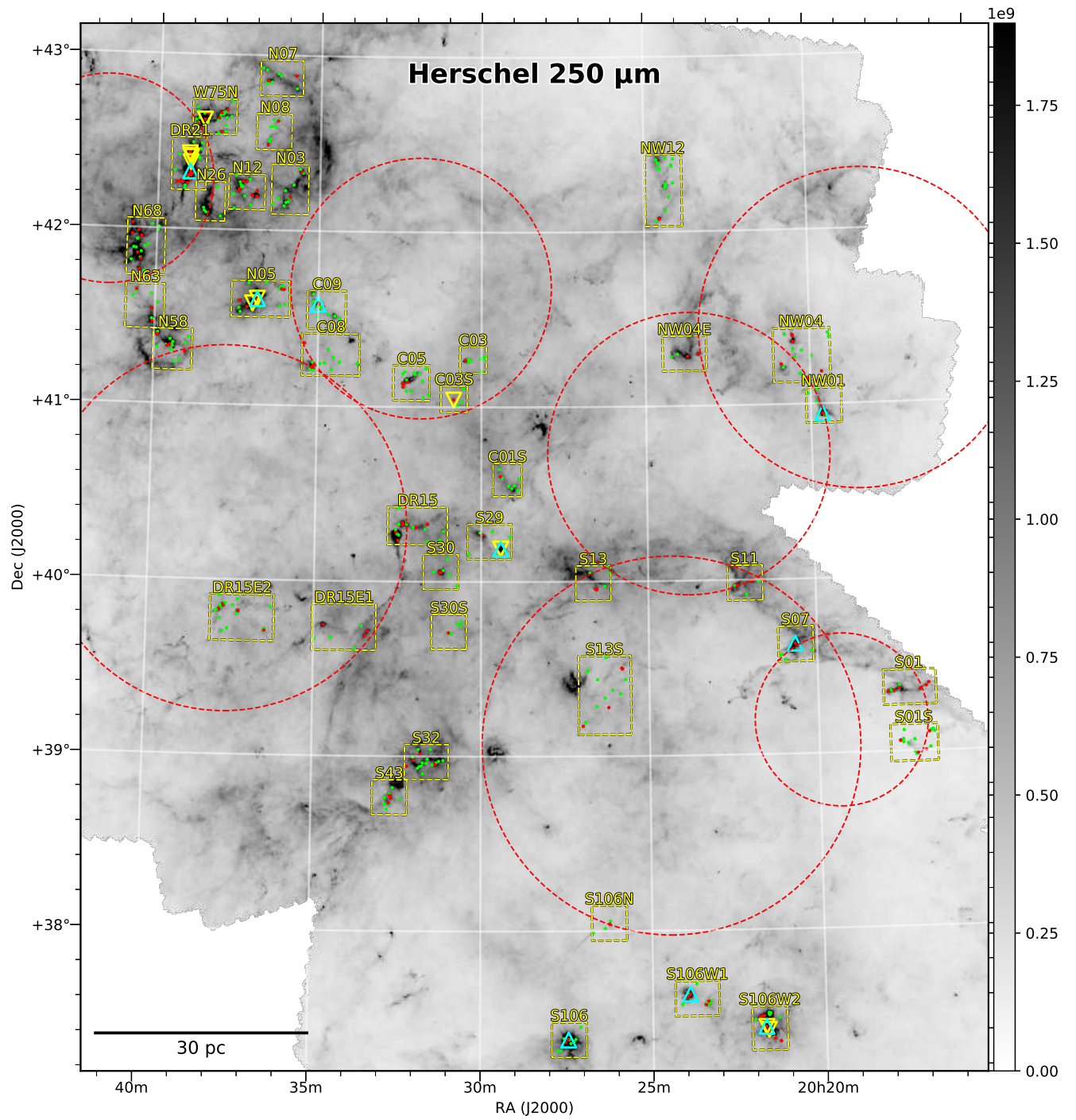


Figure F5. *Herschel* 250 μm map (Jy sr^{-1}) with the same legends as in Figure 1. This map was created using the images from the *Herschel* Science Archive.

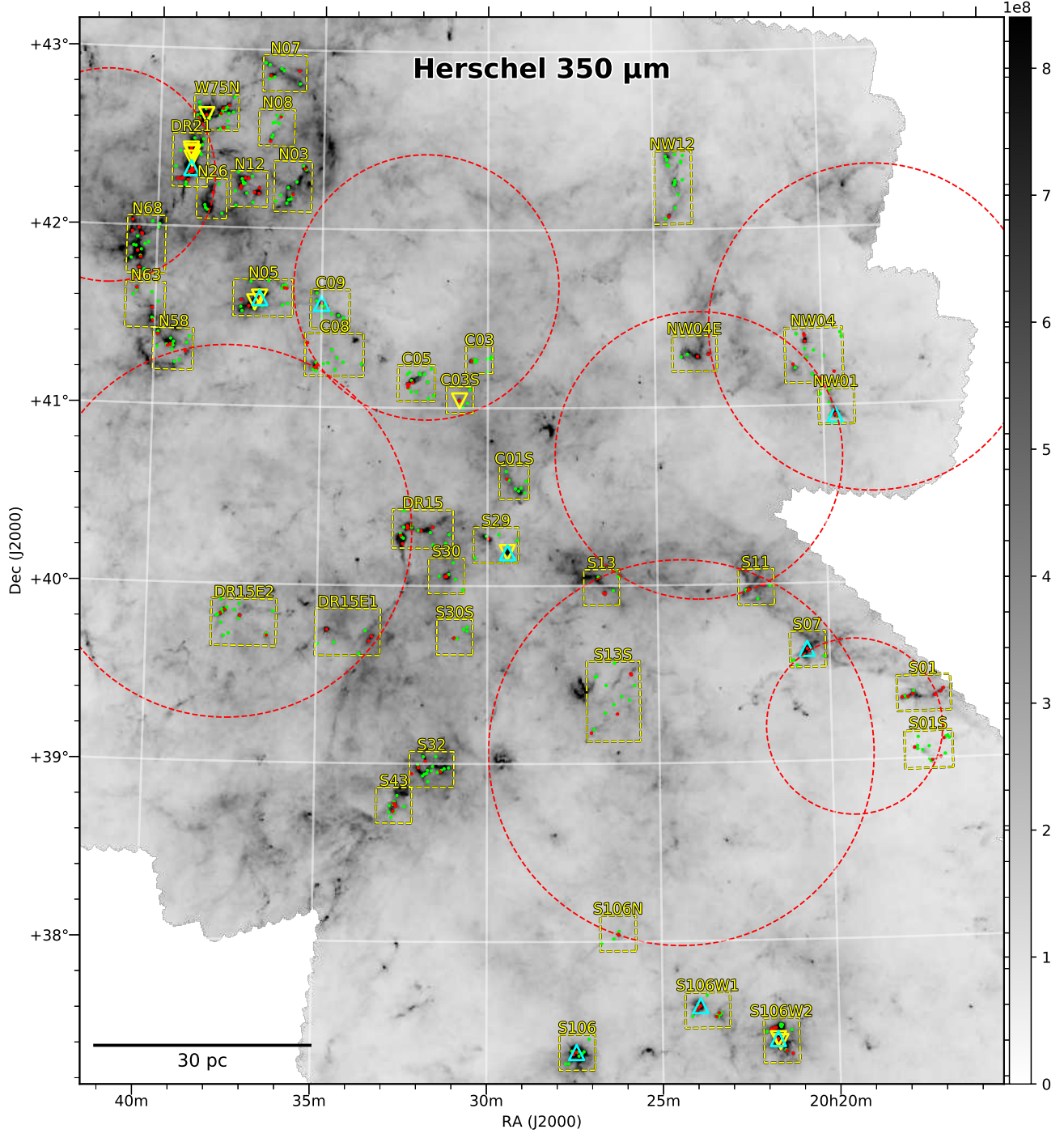


Figure F6. *Herschel* 350 μm map (Jy sr^{-1}) with the same legends as in Figure 1. This map was created using the images from the *Herschel* Science Archive.

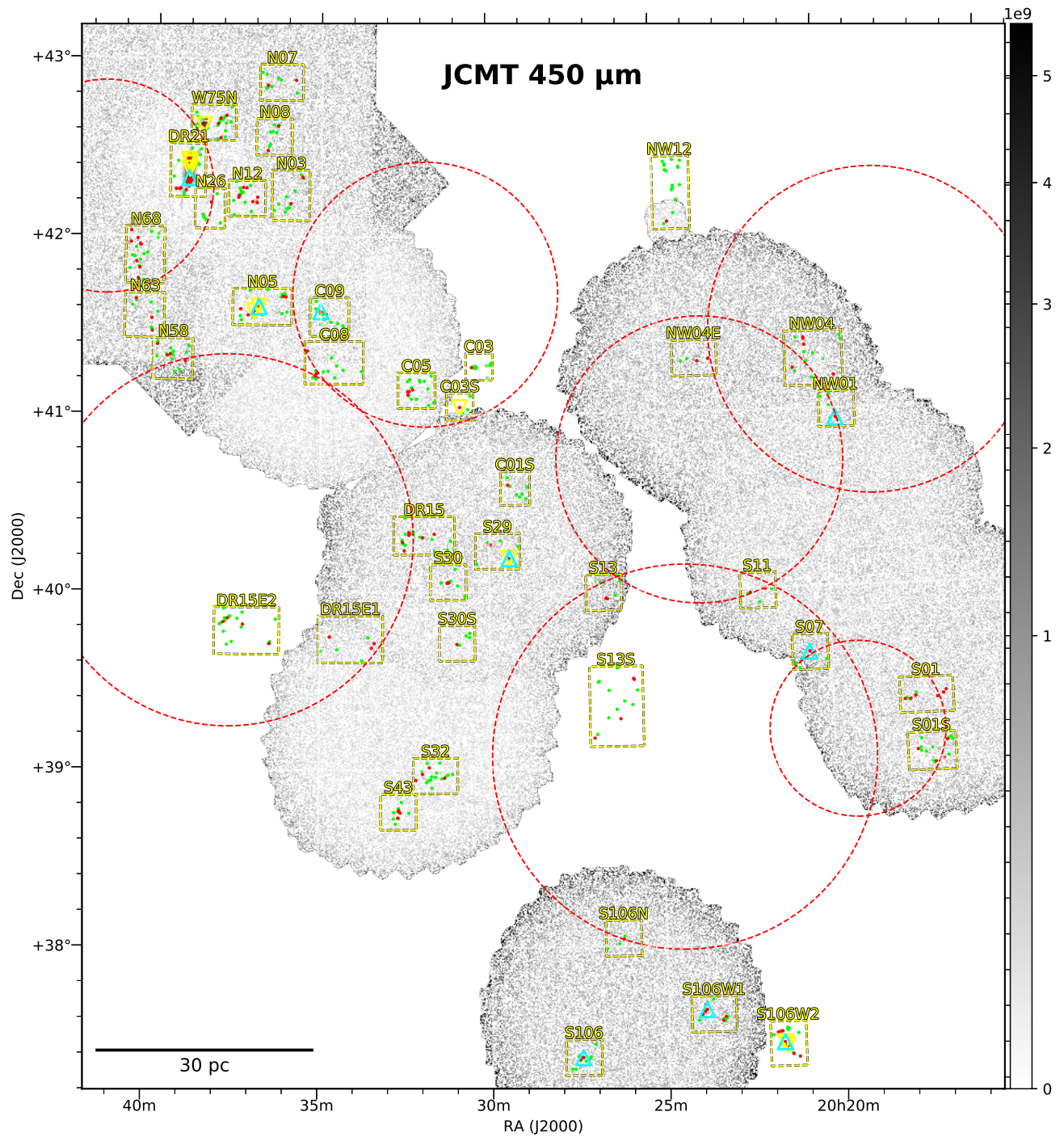


Figure F7. JCMT 450 μm map (Jy sr^{-1}) with the same legends as in Figure 1. This map was created using the data from the the Canadian Astronomy Data Centre.

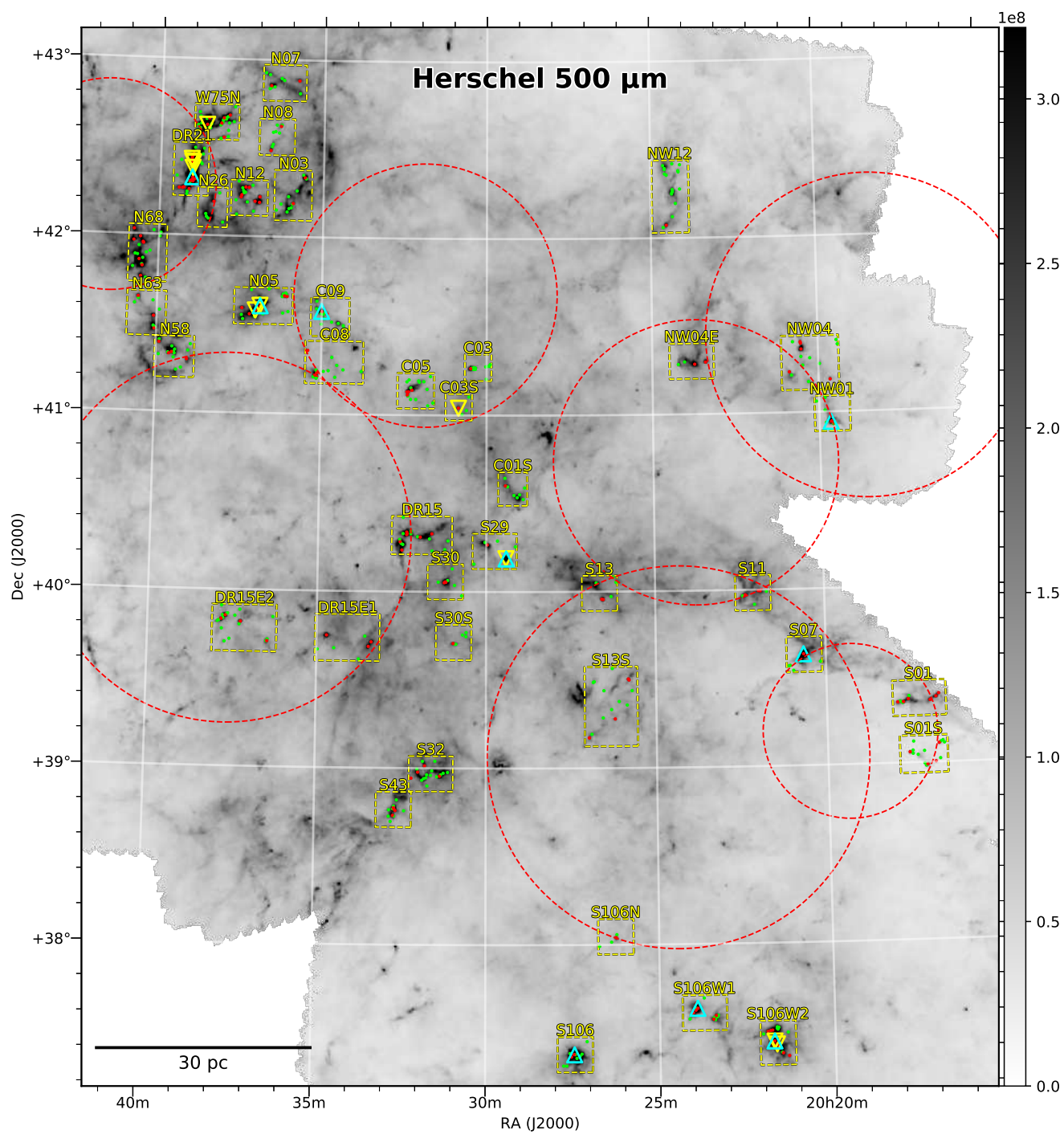


Figure F8. *Herschel* 500 μm map (Jy sr^{-1}) with the same legends as in Figure 1. This map was created using the images from the *Herschel* Science Archive.

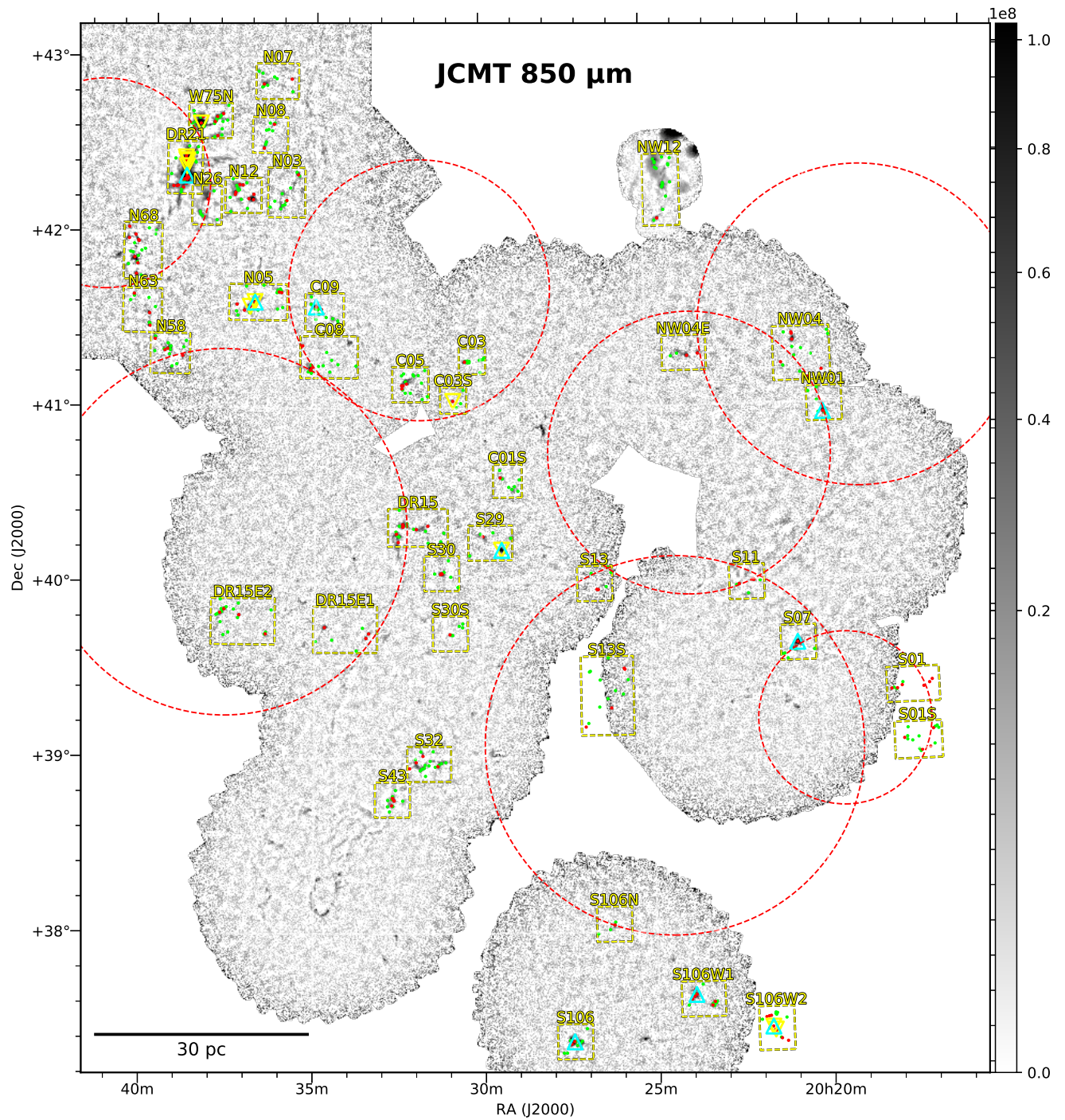


Figure F9. JCMT 850 μm map (Jy sr^{-1}) with the same legends as in Figure 1. This map was created using the data from the the Canadian Astronomy Data Centre.

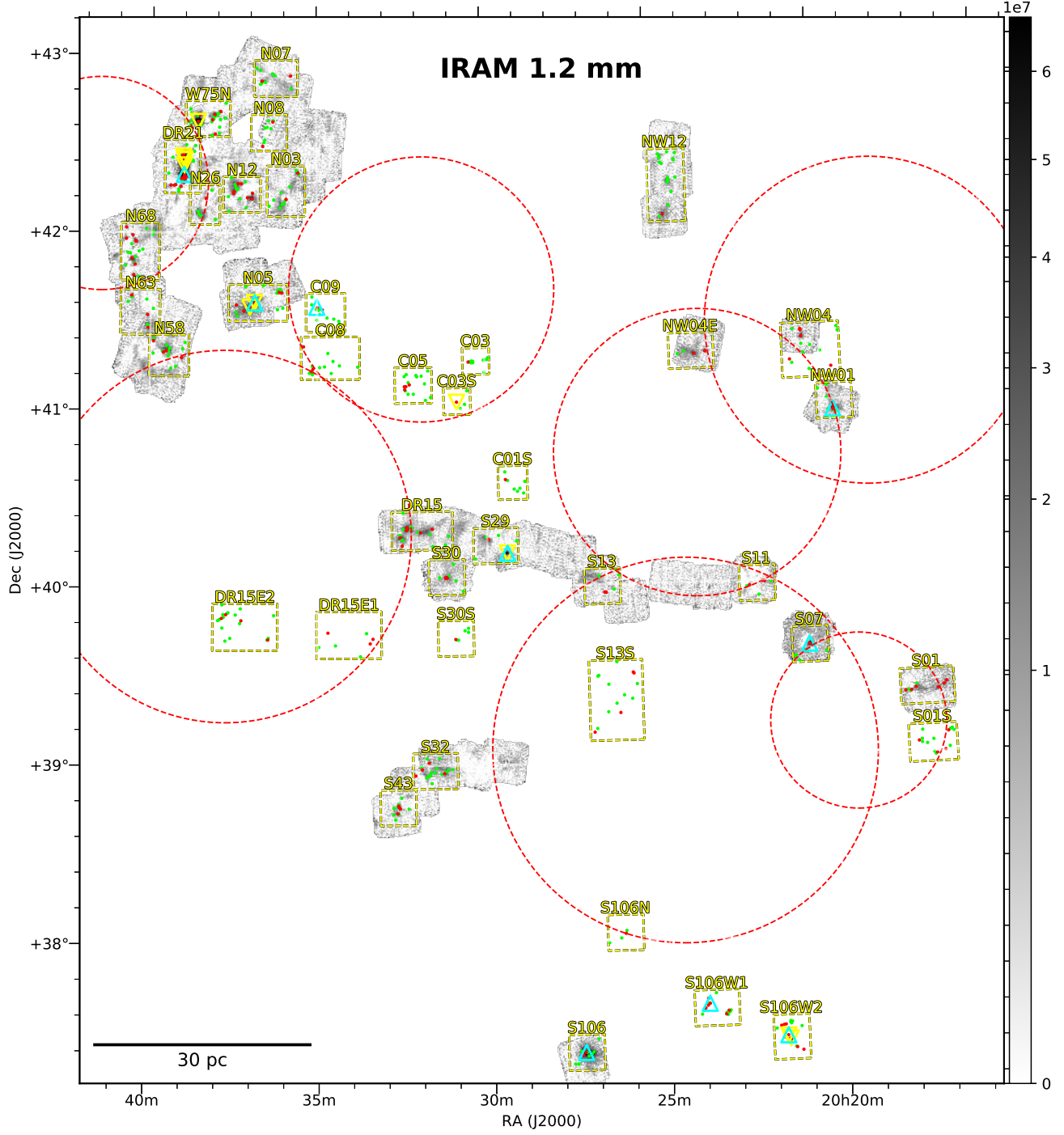


Figure F10. IRAM 1.2 mm map (Jy sr^{-1}) with the same legends as in Figure 1. This map was created using the images in M07.

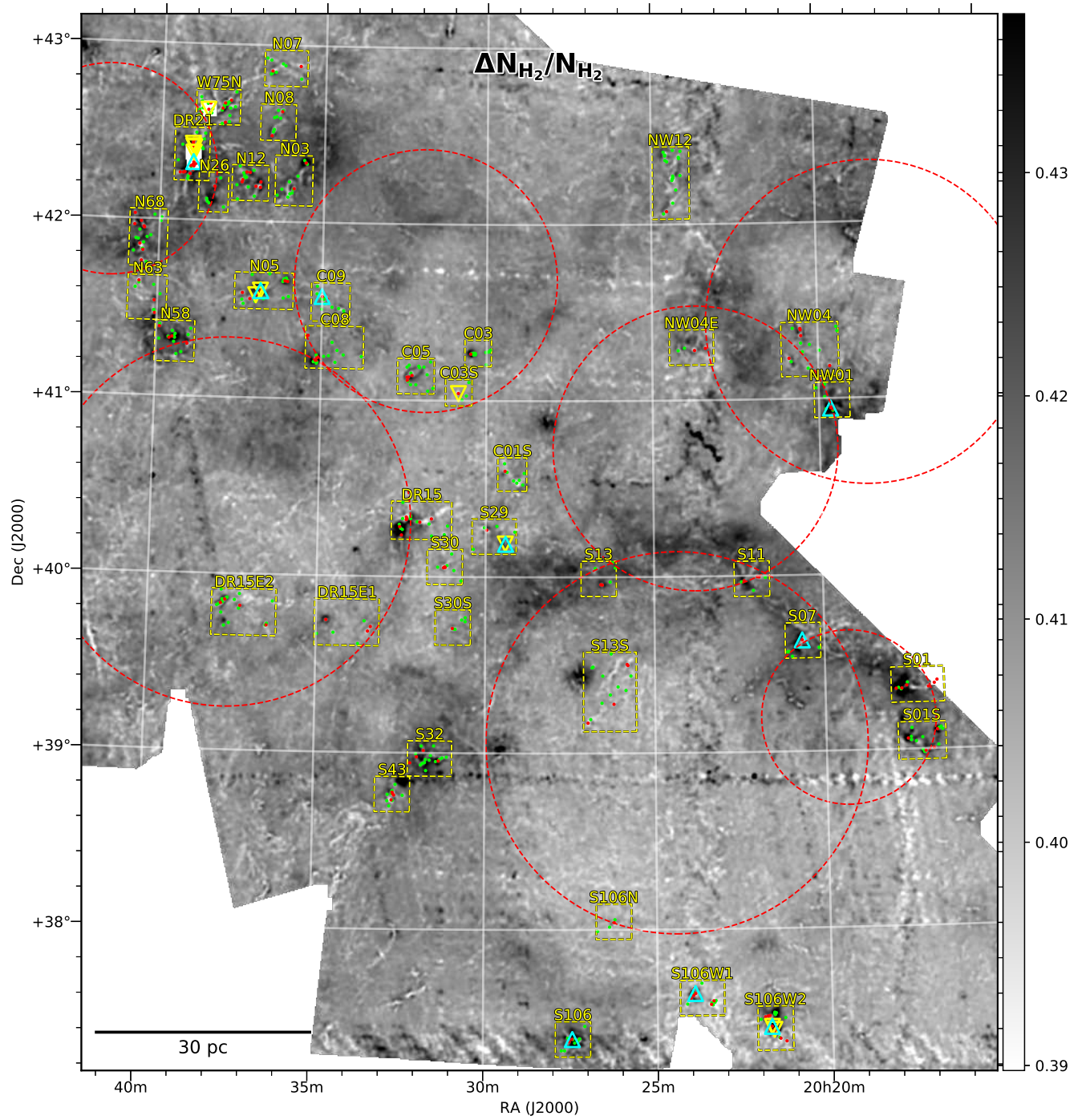


Figure F11. Relative uncertainty map of H₂ column density with the same legends as in Figure 1. This map was derived from the outputs of the *hirescoldens* command.

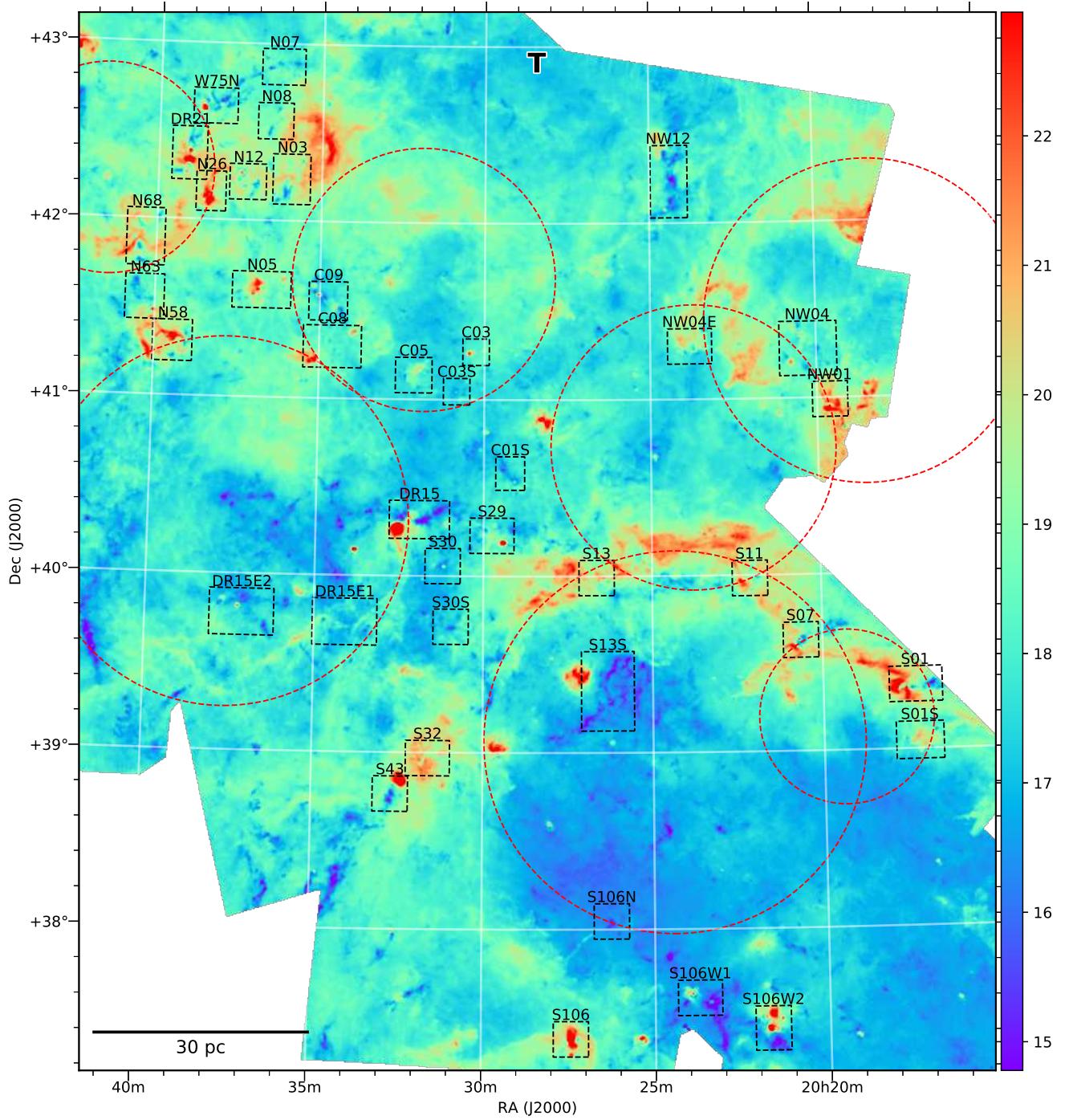


Figure F12. Temperature map (K). This map was derived from the outputs of the *hirescoldens* command.

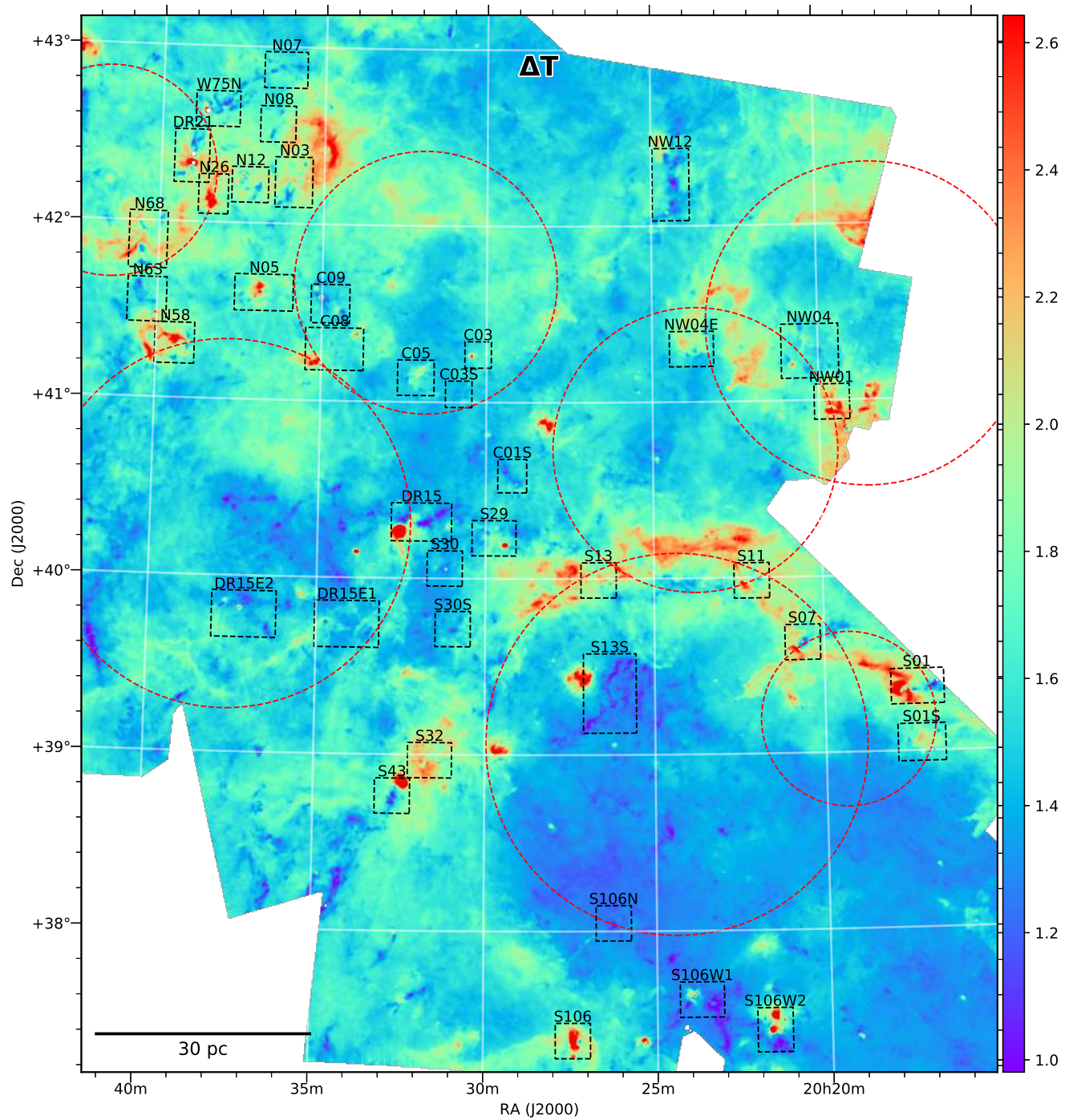


Figure F13. Map of temperature uncertainty (K). This map was derived from the outputs of the *hirescoldens* command.

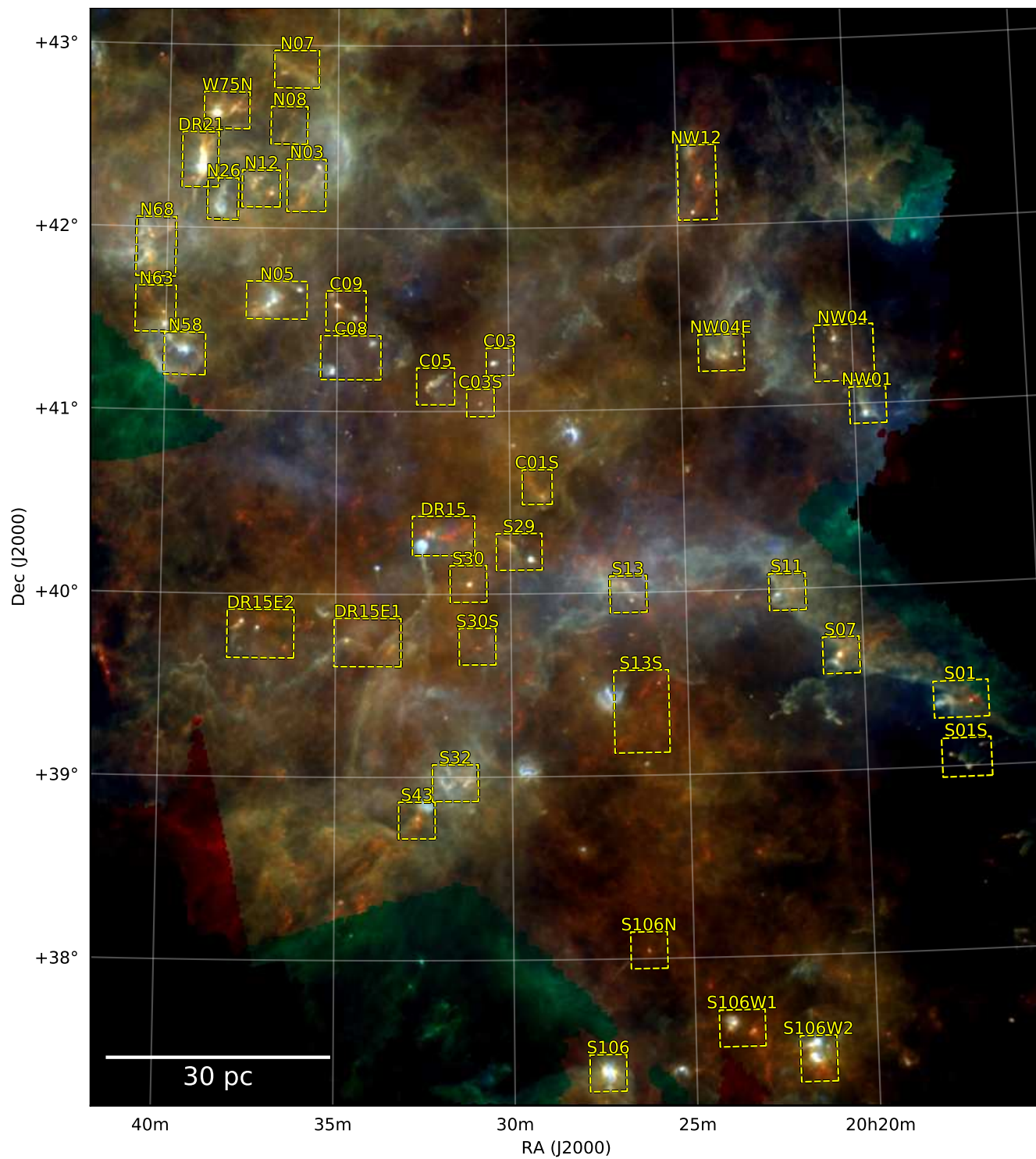


Figure F14. RGB map. R=*Herschel* 500 μm , G=*Herschel* 160 μm , B=*Herschel* 70 μm . Color scales are logarithmically stretched. This map was created using the images from the *Herschel* Science Archive.